Remotely detecting submarine volcanic activity at Monowai: Insights from International Monitoring System hydroacoustic data

Dirk Metz

Worcester College

University of Oxford

Thesis submitted in support of an application for leave to supplicate for the degree of

Doctor of Philosophy

Hilary Term 2018

Remotely detecting submarine volcanic activity at Monowai: Insights from International Monitoring System hydroacoustic data

Dirk Metz

Worcester College

University of Oxford

Hilary Term 2018

Abstract

Monowai is an active submarine volcanic center in the Kermadec Arc, Southwest Pacific Ocean. We show, using cross-correlation and time-difference-of-arrival techniques, that low-frequency underwater sound waves from the volcano travel in the Sound Fixing and Ranging (SOFAR) channel and can be detected by bottom-moored hydrophone arrays of the International Monitoring System (IMS), a global sensor network maintained by the Comprehensive Nuclear-Test-Ban Treaty Organization. Hydroacoustic phases associated with the May 2011 eruption at Monowai are identified in the record of the IMS station at Ascension Island, Equatorial Atlantic Ocean. The source-receiver distance of ∼15,800 km is the furthest documented range of any naturally occurring underwater signal ever observed. Our observations are consistent with results from transmission loss modeling, which suggest that acoustic propagation at southern latitudes is facilitated by the anomalous temperature regime of the Antarctic Circumpolar Current. Subsequently, we examine the 3.5-year record of the IMS hydrophone station near Juan Fernández Islands, Southeast Pacific Ocean, for volcanic activity at Monowai. Density-based clustering of arrivals during the time periods when data is available, i.e. from July 2003 to March 2004, and between April 2014 and January 2017, reveals 82 discrete episodes that are spaced days to weeks apart, typically ranging from a few hours to days in length. The resolution of the hydrophone data for seismic events at the volcano is estimated at 2.2 m_b and exceeds regional broadband networks by one order of magnitude. Considering the results and techniques developed in the study of Monowai, we investigate the 2014 submarine eruption of Ahyi volcano in the Northern Mariana Islands. Acoustic phases of the 15-day episode are identified in the record of an IMS hydrophone array located at Wake Island in the northwestern Pacific Ocean. Explosive volcanic activity occurred in two bursts, accompanied by a decrease in low-frequency arrivals that is interpreted as a shift in signal source parameters. Acoustic energy released during the event is on the order of 9.7 10^{13} J.

Remotely detecting submarine volcanic activity at Monowai: Insights from International Monitoring System hydroacoustic data

Dirk Metz

Worcester College

University of Oxford

Hilary Term 2018

Extended Abstract

Little is known about active volcanism in the global ocean. As the inaccessibility of the marine environment precludes the use of conventional volcano monitoring techniques, only a few active sites have been investigated in detail or over a longer period. This observational constraint can be overcome by the study of long-range underwater sound waves that are generated by the sudden displacement of material within the seabed or the water column, for example during earthquakes or volcanic eruptions. Signals below a few hundred Hertz are refracted along the Sound Fixing and Ranging (SOFAR) channel, a distinct layer of minimal sound velocity in the oceanic water column that serves as an acoustic waveguide. Once trapped in the SOFAR channel, acoustic phases propagate efficiently over hundreds or thousands of kilometers. The detection of low-frequency underwater sound is a key feature of the International Monitoring System (IMS), a global sensor network maintained by the Preparatory Commission for the Comprehensive Nuclear-Test-Ban Treaty Organization. As part of the verification regime for the Comprehensive Nuclear-Test-Ban Treaty of 1996, the prime objective of the IMS is to detect nuclear explosions on land, in the atmosphere, and in the ocean. Therefore, in addition to seismic and infrasound waveform technologies, the IMS includes eleven hydroacoustic receiver sites: Five land-based,

high-frequency seismometers and six bottom-moored hydrophone arrays, the latter of which are typically deployed at remote ocean islands and near the depth of the SOFAR channel.

Using data gathered by IMS instruments, the work presented here focuses on the long-range acoustic detection of volcanic activity at Monowai, a submarine volcanic center in the northern Kermadec Arc, Southwest Pacific Ocean. During May 2011, Monowai erupted over a period of five days, with explosive activity directly linked to changes in seafloor topography and the generation of seismoacoustic tertiary waves, so called 'T phases', recorded by regional broadband seismometers. We show, using cross-correlation and time-difference-of-arrival techniques, that the eruption is detected as far as Ascension Island, equatorial South Atlantic Ocean, where hydrophone station H10 is operated as part of the IMS network. Hydroacoustic phases from the volcanic center must therefore have propagated through the SOFAR channel in the South Pacific and South Atlantic Oceans, a source-receiver distance of ∼15,800 km. We believe this to be the furthest documented range of a naturally occurring underwater signal above 1 Hz. Our observations are consistent with results from transmission loss modeling, which suggest that acoustic propagation at southern latitudes is facilitated by the anomalous temperature regime of the Antarctic Circumpolar Current.

In the past, activity at Monowai had been intermittently observed in the form of fallout at the sea surface, changes in seafloor depth, and T phase seismicity, but no continuous record exists for recent years. Hence, we investigated 3.5 years of recordings of the southern hydrophone array at IMS station H03, located at Juan Fernández Islands, Southeast Pacific Ocean, for long-range underwater sound waves from Monowai. Results from a plane-wave-fitting approach and density-based spatial clustering are consistent with previous studies and indicate that 82 discrete episodes of activity occurred during the time periods when data was available, i.e. between

July 2003 and March 2004, and from April 2014 to January 2017. Volcanic episodes are typically spaced days to weeks apart, range from six hours to 14 days in length, and amount to a cumulative sum of 137 days of arrivals in total, making Monowai one of the most active submarine arc volcanoes currently known. The resolution of the hydrophone recordings surpasses broadband seismometer data by at least one order of magnitude and places detected seismic events at the volcano between 1.4 and 4.2 m_b. Further observations suggest volcanic activity at a location approximately 400 km north of Monowai in the Tonga Arc, and at Healy or Brothers volcano in the southern Kermadec Arc.

Considering the methods developed and implemented in the study of Monowai, we investigate the 2014 eruption of Ahyi, a submarine volcano in the Northern Mariana Islands. Results from direction-of-arrival calculations show that underwater sound phases associated with the episode are recorded at IMS station H11, located at Wake Island, northwestern Pacific Ocean. After a 3.5-hour-long sequence of precursory events that show signs of harmonic tremor, explosive volcanic activity occurred in two distinct bursts over the course of 15 days. Activity is accompanied by a notable decrease in arrivals below 8 Hz that indicates a shift in signal source parameters, potentially caused by the gradual cessation of magma movement towards the end of the eruption. Acoustic resolution of the southern H11 array exceeds broadband network data by more than half an order of magnitude, successfully identifying seismic events at Ahyi as low as 2.5 m_b. Total radiated acoustic energy of the eruption is estimated at 9.7 10^{13} J, which suggests that volcanic activity contributed significantly to the ocean soundscape.

Our findings highlight the exceptional capabilities of the IMS hydrophone network for the scientific study of active volcanism in the global ocean.

Disclaimer

The views expressed in the following document are those of the author and do not necessarily reflect those of the Preparatory Commission for the CTBTO.

Contents

List of Figures

Chapter 1

Introduction

1.1 Submarine volcanism

Little is known about active volcanism in the ocean. As eruptions are attenuated by seawater and fallout does not regularly reach the sea surface, location and timing of volcanic activity remain difficult to investigate. For example, the Global Volcanism Program currently lists a total of 568 observed or inferred subaerial volcanic eruptions worldwide in the past 2000 years, as opposed to a mere 57 in the ocean (Global Volcanism Program, 2013, Figure 1.1). Such discrepancies appear irreconcilable with current geological and geophysical knowledge given that there are at least 200,000 seamounts in the world's oceans, most of which are volcanic in origin (Hillier and Watts, 2007). The majority of all active volcanism in the ocean occurs along mid-ocean ridges and their transform fault offsets and the submarine volcanic arcs of subduction zones (e.g. Dars et al., 1995; Watts et al., 2006), but observational constraints in the marine environment are limited and there may be many more active sites in the interior of tectonic plates than we know at the present day.

While volcanoes on land can be monitored by the means of ground deformation via satellite altimetry (Parks et al., 2011), thermal imaging (Calkins et al., 2008), the

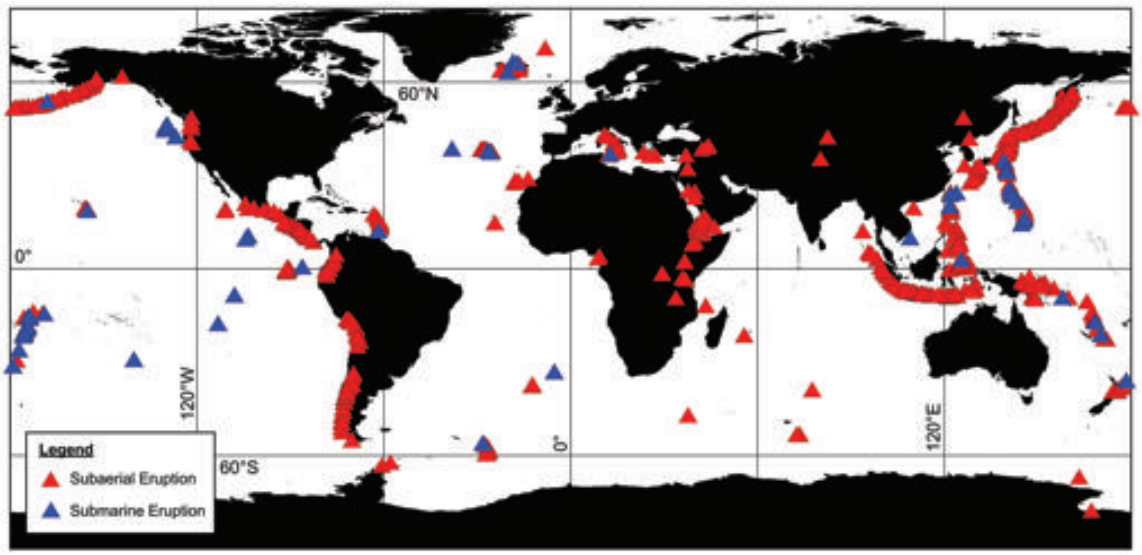

Figure 1.1: Global map of observed or inferred subaerial and submarine volcanic eruptions over the last 2,000 years according to the Smithsonian Global Volcanism Database (Global Volcanism Program, 2013), retrieved October 2017.

measurement of gas emissions (Mather et al., 2012; Bredemeyer and Hansteen, 2014) or permanently installed seismic and infrasound networks (e.g. Ketner and Power, 2013; Rodgers et al., 2013; Matoza et al., 2017), the same tools are inherently inapplicable in the ocean. Here, observations are mostly limited to secondary effects, e.g. by studying the distribution of volcanic fallout at the sea surface (Jutzeler et al., 2014) or the composition of retrieved rock samples (Stoffers et al., 1989). Only in a few cases, it has been possible to measure a volcanic episode live and onsite, either by the means of remotely operated vehicles (Chadwick et al., 2008a) or seismometer deployments (Tolstoy et al., 2006). However, rates and mechanisms of volcanic processes in the ocean have implications beyond the solid earth realm, in particular when considering their role in the climate system: As a source of trace metals and carbon dioxide (CO_2), ridge volcanism plays a key role in ocean chemistry and hence directly feeds back into long-term climatic trends such as glacial/interglacial cycles (Gernon et al., 2016). For instance, Tolstoy (2015) notes that the rate of submarine eruptions may in itself be influenced by sea level change and crustal loading due to

tidal forcing and orbital eccentricity, causing significant changes in ocean CO_2 levels, which in return affects the flux rate of the greenhouse gas across the ocean-atmosphere boundary over short time scales (thousands to hundred thousand years). Burley and Katz (2015) suggest that such external forcing of seafloor volcanism could account for up to 12% of the variation of global mid-ocean ridge CO_2 emissions. Finally, studying underwater volcanoes is important for disaster mitigation, especially where active sites are located near the coastline, as rock falls and landslides during an eruption may generate tsunamis and affect local shipping (Lindsay et al., 2005; Smith and Shepherd, 1996). In every sense, overcoming the difficulties of detecting volcanic activity in the ocean is a worthwhile scientific challenge.

1.2 The deep sound channel

The observational constraints of submarine volcanic activity can be partially overcome by the study of long-range underwater sound waves, also known as tertiary or 'T' phases as they arrive at a given receiver site after the canonical primary ('P') and secondary ('S') waves. T phases are generated by the sudden displacement of material within the seabed or the water column, for example during earthquakes or explosions (Linehan, 1940; Tolstoy et al., 1949; Ewing et al., 1951). In essence following the principles of Snells Law, acoustic phases below a few hundred Hertz are refracted along the Sound-Fixing-and-Ranging (SOFAR) channel, a distinct layer of minimal sound velocity in the oceanic water column that serves as an acoustic waveguide (Blum and Cohen, 1971), like an optical fiber but for sound (Figure 1.2). Once trapped in the SOFAR channel, acoustic phases propagate efficiently over hundreds or thousands of kilometers (Munk et al., 1994; Dushaw and Menemenlis, 2014), unless bathymetric obstacles, for example seamounts, ridges or islands, interfere (Munk and Zachariasen, 1991). As a cumulative effect of water temperature, pressure, and, to a

lesser degree, salinity, the deep sound channel occurs at varying depths in the global ocean (Northrop and Colborn, 1974): At mid-latitudes, the SOFAR axis is typically found at around 800-1000 m, but shoals to as little as a few dozen meters below sea level in the colder waters beyond 60° latitudes (de Groot-Hedlin et al., 2009).

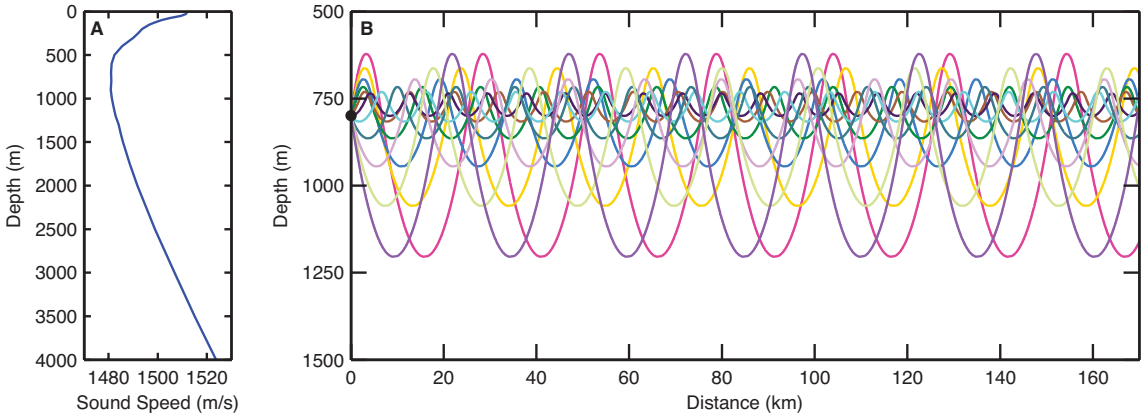

Figure 1.2: Simplified view of the SOFAR channel domain. (a) Generic sound speed profile for a mid-latitude location. The sound speed minimum is located at approximately 800 m. (b) Raytracing results using the profile shown in (a) for an acoustic point source (black dot) near the sound channel axis. Takeoff angles are between -5 and +5° from the horizontal. Note the different scales on the y-axis.

During the transition from ocean to land, seismoacoustic signals can be converted effectively to body and surface waves, thus becoming detectable by land-based and ocean-moored instruments alike (e.g., Stevens et al., 2001; Kosuga, 2011). Helffrich et al. (2006) and Ito et al. (2012) show that T phase seismicity can significantly improve earthquake detection and relocation where seismic coverage by conventional methods is poor. Furthermore, high incidences of T phases recorded by remote island stations aided in locating a number of volcanically active sites across the Pacific region, including, amongst others, Kaitoku Seamount in the Volcano Islands (Izu-Bonin Arc), Rumble Seamounts in the southern Kermadec Arc, the Teahitia-Mehitia volcanic complex near Tahiti (Talandier and Okal, 1987), and Macdonald Seamount in the Austral Islands (Talandier and Okal, 1984).

Seismic detections of T phases are normally made by inspecting records of oppor-

tunity, for example gathered by readily available land-based networks (Buehler and Shearer, 2015) or ocean bottom seismometer deployments (Snelling, 2015). However, it has been shown that the conversion and loss of seismoacoustic energy at the ocean-land interface is a complex function of local bathymetry, distance between source and receiver as well as receiver and conversion point, and signal frequency (Koyanagi et al., 1995; Kosuga, 2011). Attenuation during the conversion process may hinder, or inhibit entirely, the detection of T phases by land-based seismometers, making it more favorable to record the acoustic signal in the water column directly (Stevens et al., 2001). Following the successful use of the clandestine US Sound Surveillance System (SOSUS) for identifying hydroacoustic phases of earthquakes and volcanic eruptions (e.g., Norris and Johnson, 1969; Northrop, 1974), the Pacific Marine Environmental Laboratory (PMEL) developed a designated, autonomous hydrophone system for scientific ocean monitoring (Fox et al., 2001). Depending on the target site, up to half a dozen bottom-moored instruments can be deployed and then recovered at distances of tens to a few hundred kilometers, thus enabling acoustic coverage for regional observations of mid-ocean ridge earthquakes (Smith et al., 2003; Williams et al., 2006), bioacoustic sources (Nieukirk et al., 2004), and submarine volcanic eruptions, including, for example, activity at Axial Volcano (Dziak et al., 2011), Anatahan Volcano (Dziak et al., 2005), NW Rota (Schnur et al., 2017), West Mata (Dziak et al., 2015), and Hunga Ha'apai-Hunga Tonga (Bohnenstiehl et al., 2013).

We note that some ambiguity exists in current literature regarding the applicability of the term 'T phase', which is sometimes used synonymously for signals recorded on land-based seismometers and water column hydrophones. Here, we adapt the terminology of the International Association of Seismology and Physics of the Earth's Interior (IASPEI) and limit the term 'T phase' to arrivals that partially travel in the ocean sound channel and are registered by land-based stations. This measure excludes Chapter 2 so as to maintain consistency with its published version.

1.3 Volcanic activity at Monowai, 26°S Kermadec Arc

Monowai is an active submarine volcanic center at 25.89°S, 177.18°W in the northern Kermadec Arc, Southwest Pacific Ocean (Figure 1.3a). The center consists of a stratocone, rising from approximately 1200 m to less than 100 m below sea level and 12 km in diameter at its base, a number of parasitic side cones, and a 10 km wide, approximately 600 m deep caldera with ring faults and a central mound to the northeast (Wormald et al., 2012, Figure 1.3b). The stratocone and caldera are located within a 20 km wide graben, part of an en-echelon rift system that spans the length of the arc (Paulatto et al., 2014).

Eruptive activity at Monowai has been well-documented for almost four decades by designated expeditions, passing vessels, and during flyovers conducted by military aircrafts, but may have been witnessed as early as 1877 (Mastin and Witter, 2000). Observations typically include pumice rafts, discolored water, and vigorous gas emissions at the sea surface (Davey, 1980), suggesting that volcanism onsite is, at least in parts, phreatomagmatic and explosive (Graham et al., 2008; Wright et al., 2008). Leybourne et al. (2012) also note hydrothermal venting in at least three discrete locations near the summit of the cone and the southwestern caldera wall.

As a result of ongoing volcanic processes, seafloor topography at Monowai is highly dynamic: Comparing high-resolution bathymetric datasets of the main stratocone, Chadwick et al. (2008b) observe depth changes of up to 176 m between surveys in 1998, 2004, and 2007, and suggest that gradual oversteepening of the summit area due to the addition of new material and subsequent sector collapses may alter in a cyclic pattern. Wright et al. (2008) estimate average annual growth rates of the stratocone at around 0.01 km^3 in volume, and 47 m in height in between distinct collapse events. Repeat swath mapping in May and June 2011, immediately before

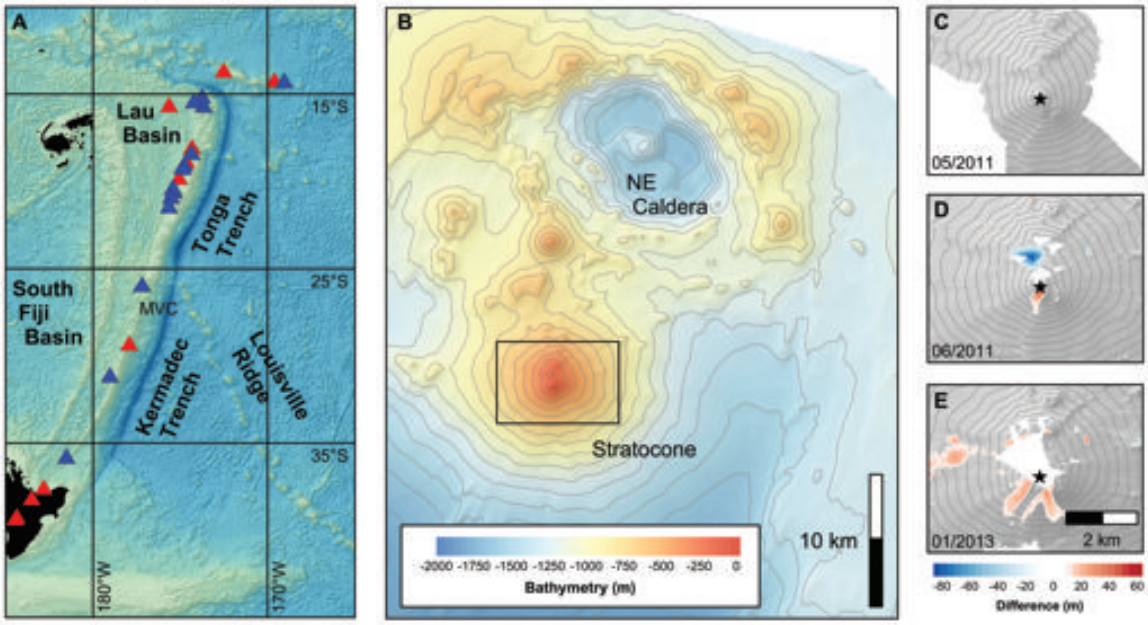

Figure 1.3: Monowai Volcanic Center. (a) Overview of the Tonga-Kermadec Arc area, including observed or inferred volcanic eruptions over the past 2000 years, and Monowai Volcanic Centre (MVC) at 26°S. (b) Seafloor topography of the main cone and the caldera to the northeast. The black rectangle outlines the position of subfigures 1.3c to 1.3e. Grey lines represent 100m contour intervals. (c-e) Shaded view of the cone during mapping campaigns aboard R/V SONNE in May 2011, June 2011 (Watts et al., 2012), and January 2013 (Werner et al., 2013). Black stars mark the location of the May 2011 summit for orientation. Grey lines represent water depth contoured at 50m intervals. Bathymetric differences between the consecutive surveys are contoured at 5 m intervals. Red and blue coloring indicates areas of growth and collapse, respectively.

and after a volcanic episode occurred, revealed topographical differences of tens of meters within a period of 18 days alone (Watts et al., 2012), including a sector collapse of 18 m at the northern flank of the edifice and the growth of a 72 m high summit cone (Figure 1.3c-d). Most recent bathymetry gathered in January 2013 shows a number of new deposits along the southern and western flanks of the volcano (Figure 1.3e), all in the range of up to 30 m difference compared to the June 2011 survey and potentially a result of renewed, downslope evacuation of material from the top of the edifice. Unfortunately, the summit area could not be surveyed due to a sudden increase in volcanic activity during the swath mapping campaign (Werner et al., 2013).

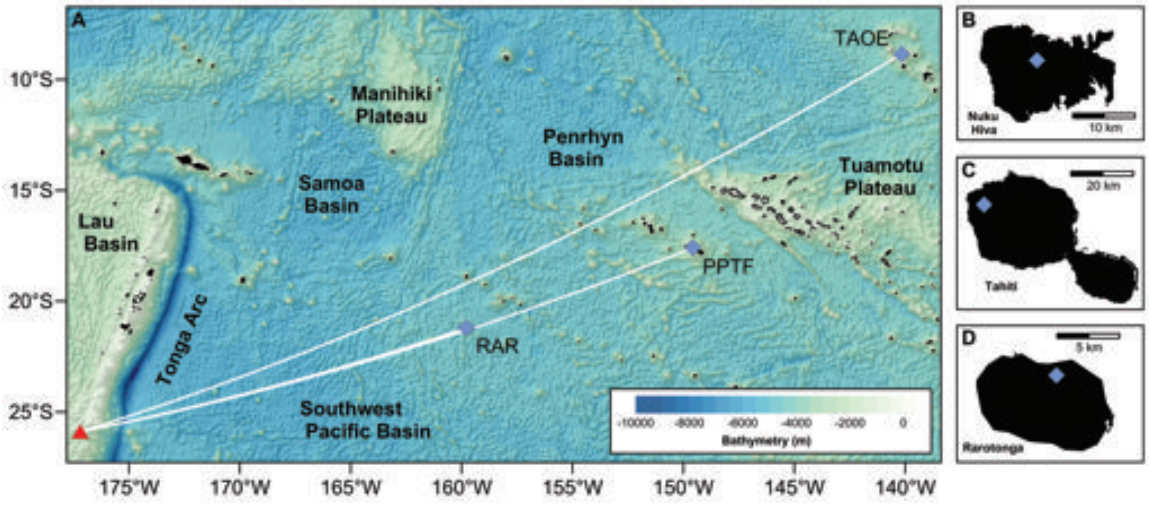

Figure 1.4: (a) During the May 2011 eruption, reported by Watts et al. (2012), T phases associated with volcanic activity at Monowai (red triangle) were recorded by three land-based broadband seismometers (blue diamonds) located at (b) the Marquesas Islands (TAOE), (c) Papeete (PPTF), and (d) Rarotonga (RAR). Source-receiver distances are 4340 km, 2991 km, and 1847 km, respectively. Corresponding T phase arrivals are shown in Figure 1.5.

T phases generated by volcanic activity at Monowai have been intermittently observed in the Southwest Pacific region (Talandier and Okal, 1987). In the case of the May 2011 eruption, a five day long burst of arrivals was recorded at broadband seismometers located at Rarotonga (Cook Islands), Papeete (Tahiti), and Marquesas Islands (Figures 1.4 and 1.5), thereby directly linking seismoacoustic observations

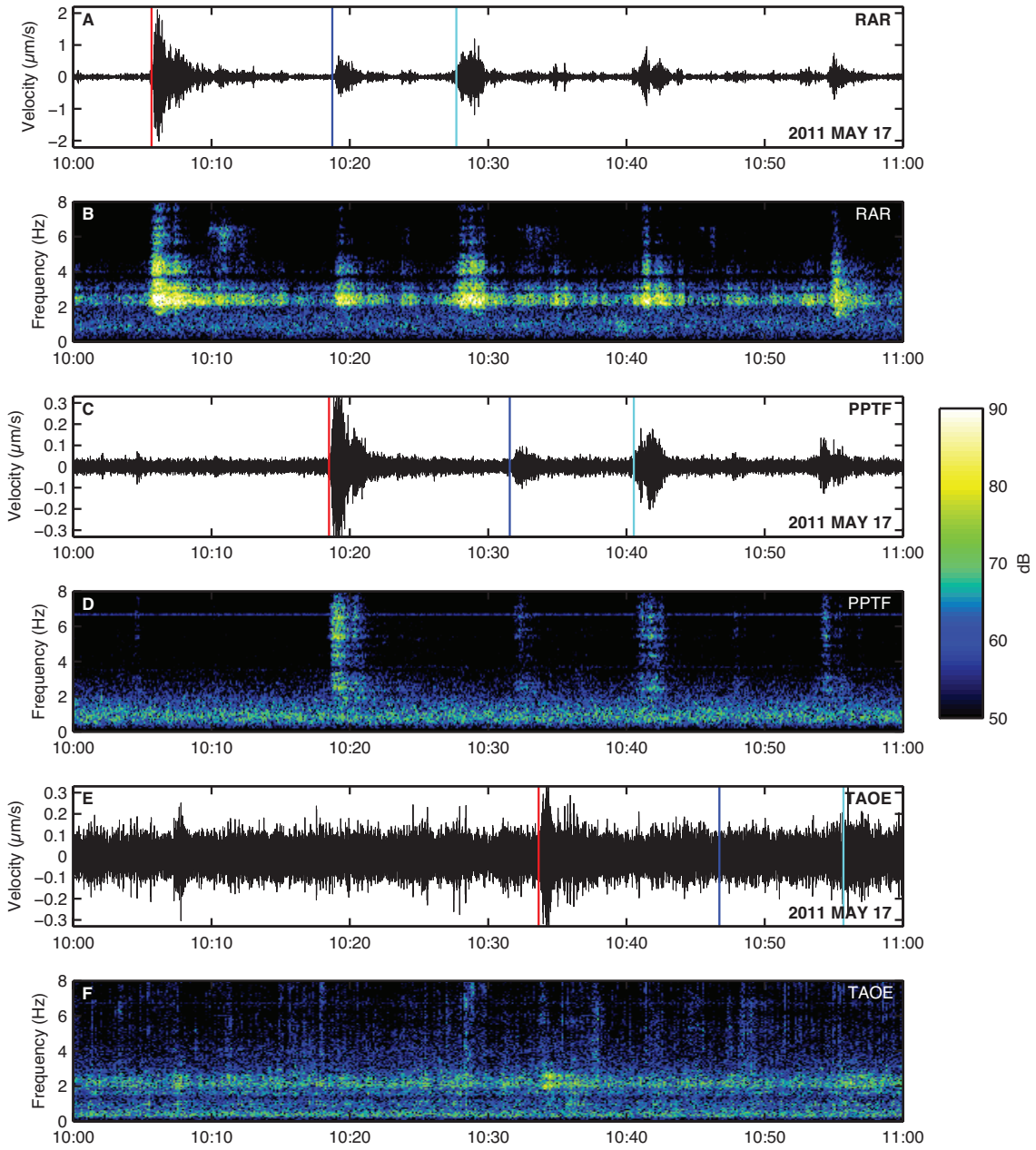

Figure 1.5: Seismic traces and spectral plots of T phases associated with the May 2011 eruption at Monowai, recorded at Rarotonga (RAR), Papeete (PPTF), and the Marquesas Islands (TAOE). Data is recorded at 20 Hz, with the exception of the TAOE station, where the sampling rate is 50 Hz. After correcting for instrument response, a mean and trend are removed and recordings are high-pass filtered at 2 Hz. Spectral data is normalized to highlight the gradual attenuation of the signal as it propagates away from the source, with stations shown at increasing distance from top to bottom. Colored lines highlight three distinct T phases in the record of RAR station and assume a propagation speed of 1480 m/s, thus corresponding well to the arrival times of the same events at PPTF station. Only the strongest event (red line) can be distinguished at station TAOE.

and changes in seafloor depth due to submarine volcanic activity for the first time. Assuming a linear relationship between the duration of the burst and the volume of material newly deposited, Watts et al. (2012) estimate annual growth rates at about 0.7 km^3, assuming a steady increase during two to three eruptive episodes per year. This rate is ten times higher than values previously calculated for Monowai (0.07 km^3 per year, cf. Chadwick et al., 2008b; Wright et al., 2008), and two orders of magnitude higher than implied from repeat surveys at other submarine arc volcanoes, for example Kick 'em Jenny in the Lesser Antilles (Lindsay et al., 2005), thus highlighting both the larger volume of material deposited during the May 2011 event compared to previous eruptions as well as the dynamic nature of volcanic processes at Monowai.

Due to its continuing record of intermittent activity, Monowai is an ideal candidate for studying submarine arc volcanism. However, continuous efforts are impeded by the volcano's remote, undersea location. Although T phases have been detected at the three permanently installed broadband seismometers previously described, they are not suited for the long-term observation of volcanic activity at Monowai: Compared to RAR data (Figure 1.5a-b), T phase signals appear highly attenuated at PPTF (Figure 1.5c-d), and only the strongest events are detected at TAOE, most likely due to the station's high ambient noise levels above 2 Hz (Figure 1.5e-f). Furthermore, seismometers at Tahiti typically suffer from extremely high ambient noise levels during daytime, rendering half of all recordings at this location unusable for standard seismic processing, including signal relocation (Figure 1.6). As a result, T phase arrivals currently cannot be reliably accredited to Monowai. To better study activity at the volcano, an alternative network of seismic or hydroacoustic sensors would be needed, preferably in locations that compliment pre-existing data and allow for detection and long-term tracking of volcanic episodes. Although designed for a different purpose, such an infrastructure already exists, as described in the next section.

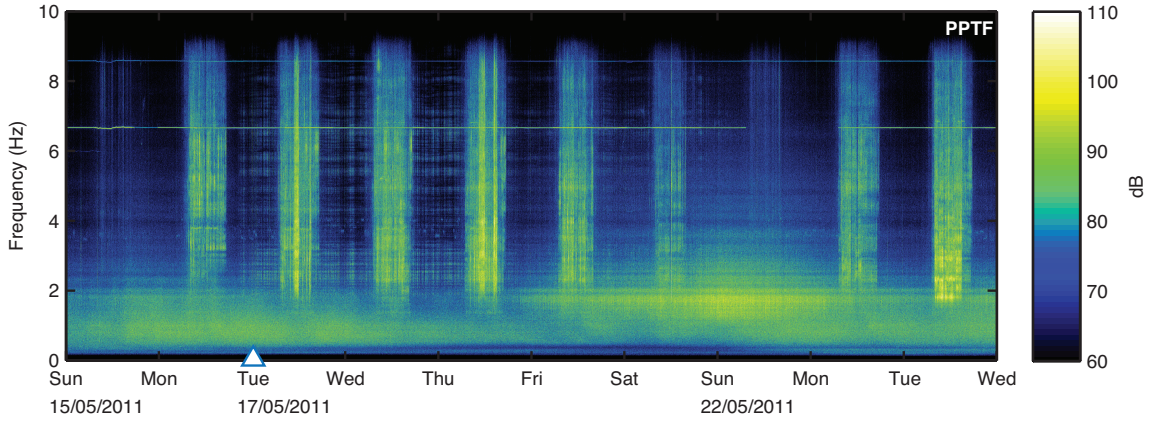

Figure 1.6: 10-day spectrogram of broadband seismic recordings at the PPTF station, beginning on Sunday, 00:00 15 May 2011. Data is sampled at 20 Hz, high-pass filtered at 1 Hz and displayed in Tahiti local time (UTC-10). Note the high levels of ambient noise during weekday daytime, most likely due to anthropogenic sources. The two distinct lines at 6.5 and 8.5 Hz probably correspond to one or more hydroelectric power plants in the area. Following previous observations by Le Pichon et al. (2004), episodic increases in low-level ambient noise below 2 Hz, such as around 22 May, may be caused by the breaking of larger ocean waves along the Tahiti shoreline ('surf noise'). T phases from Monowai are observed best in between the broadband bursts from Tuesday, May 17, to Thursday, May 19, in the 2-6 Hz frequency range. The white triangle highlights the relative position of data shown in Figure 1.5c-d. The dB scale refers to instrument counts only.

1.4 The International Monitoring System

The Preparatory Commission for the Comprehensive Nuclear-Test-Ban Treaty Organization (CTBTO) was established by the signatory states of the Comprehensive Nuclear-Test-Ban Treaty (CTBT) of 1996. As part of the verification regime of the treaty, which requires state parties "[...] not to carry out any nuclear weapon test explosion or any other nuclear explosion [...]" (Article I) on land, in the atmosphere, and in the ocean, a global sensor network was put in place, the International Monitoring System (IMS). The primary task of the IMS is to monitor the planet for clandestine nuclear tests by the means of continuous seismic, infrasonic, and hydroacoustic measurements. In addition to this waveform component, the network comprises stations to measure aerial concentrations of certain radioactive particles and noble gases, which can be by-products of nuclear explosions. As of October 2017, 209 waveform and 80 radionuclide stations were operational and certified worldwide (Figure 1.7a), with a total of 337 stations scheduled for completion by the time the treaty enters into force.

Seismic, infrasound, and radionuclide data gathered by the IMS helped to successfully detect, identify, and further investigate the six announced nuclear tests conducted by the Democratic Peoples Republic of North Korea since 2006 (Bowers et al., 2002; Selby et al., 2003; Becker et al., 2010; Assink et al., 2016). However, since the beginning of its installation 20 years ago, the comprehensive network has given rise to the scientific study of phenomena beyond the realm of nuclear non-proliferation, ranging from investigations on earthquake rupture and distribution (Guilbert et al., 2005; Hanson and Bowman, 2005b), ocean acoustic propagation and underwater noise created by icebergs (Evers et al., 2013; Evers and Snellen, 2015), to the infrasonic tracking of bolides (Brown et al., 2013) and the detection of volcanic eruptions (Fee et al., 2010; Matoza et al., 2011a,b), to name just a few examples. IMS data further aids in disaster mitigation and relief efforts: In the aftermath of the Fukushima Dai-

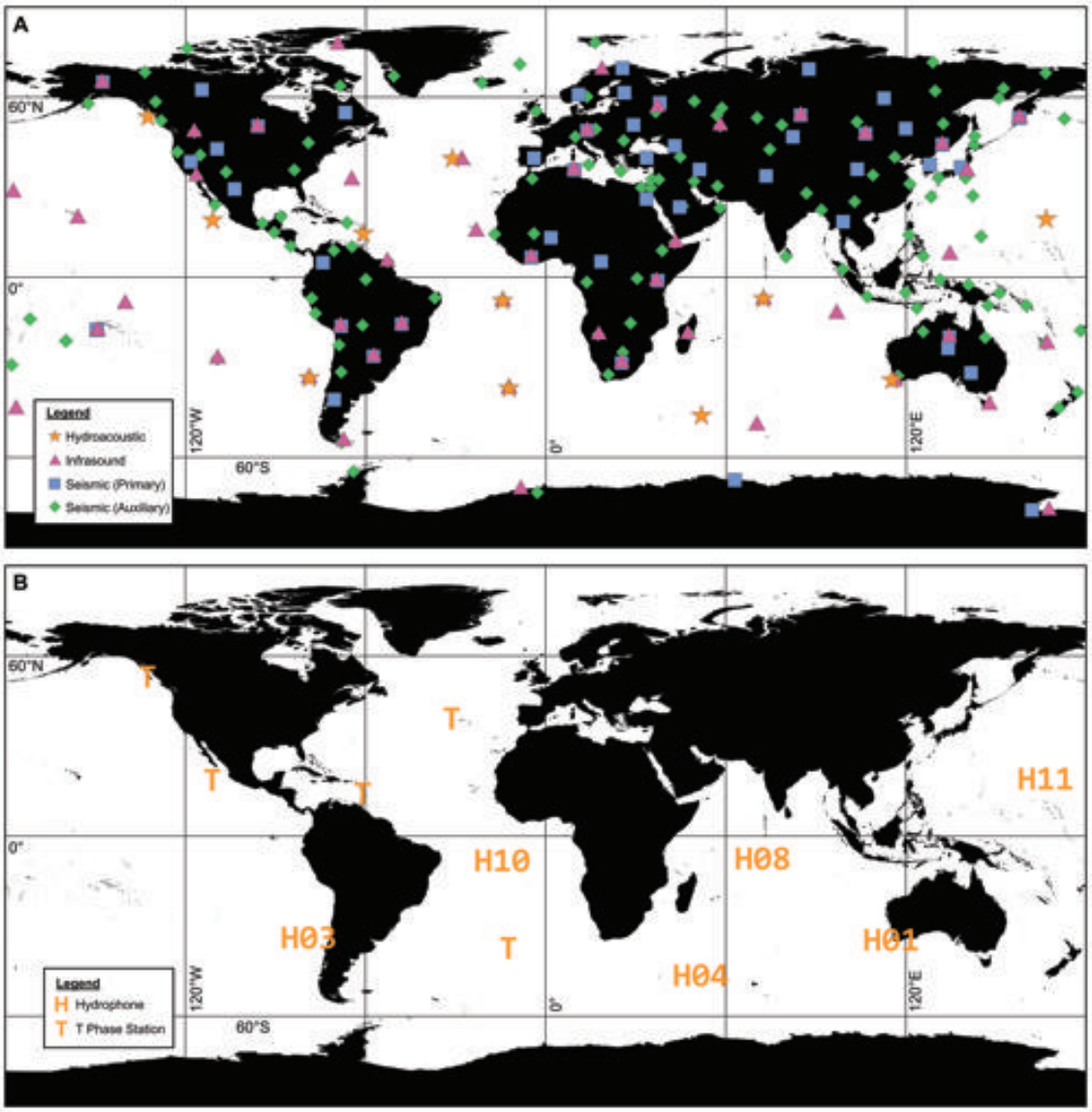

Figure 1.7: The International Monitoring System. (a) As of October 2017, the IMS consists of 209 seismic, infrasound, and hydroacoustic stations around the globe. Radionuclide stations and noble gas laboratories are omitted for clarity. (b) The hydroacoustic waveform component of the network includes five high-gain seismometers (marked T) and six hydrophone stations (marked H).

ichi power plant accident in March 2011, sensors maintained as part of the IMS proved to be a critical tool for monitoring the distribution of radioactive fallout around the globe (Schoeppner et al., 2012). Furthermore, IMS instruments are capable of serving as part of tsunami early warning systems (e.g., Hanson and Bowman, 2005a).

Access to the IMS database is free and facilitated through the virtual Data Exploitation Centre (vDEC), an online repository maintained by the CTBTOs International Data Centre (IDC), Vienna. The vDEC platform serves as an archive for IMS recordings and provides external users with access to IDC software and raw waveform data, normally at a lag time of three months. Authorization is granted directly by the Secretariat of the CTBTO and limited to an initial period of two years, after which an application for extension can be filed.

1.4.1 The IMS hydrophone network

The IMS comprises a total of six hydrophone receiver sites (Figure 1.7b). With the exception of the installation at Cape Leeuwin, Western Australia, these stations consist of two arrays, typically located at opposing sites of remote ocean islands in order to avoid acoustic blockage and maximize aperture sensitivity (Figure 1.8). Three hydrophones are bottom-moored near the local sound channel axis, at depths between 700 and 1000 m below sea level. Array elements are positioned in a horizontally aligned, tripartite configuration and inter-element spacing of 2 km, thus allowing for angle of arrival calculations of acoustic phases while also ensuring data redundancy in case of instrument failure. Due to the efficient propagation of low-frequency sound in the SOFAR channel, a mere six stations suffice to achieve coverage of the broad global ocean (Hanson et al., 2001).

Five so-called 'T phase' stations augment the IMS hydrophone network. These high-gain seismometers are optimized for the detection of seismoacoustic phases resulting from the conversion of acoustic energy at the ocean-land interface, and only

differ from standard broadband instruments by their concerted incorporation in the IMS network, a higher than usual sampling frequency of up to 100 Hz, and their designated proximity to the shoreline of steeply sloped ocean islands (Okal, 2001). T phase stations are single element, land-based instruments lacking the azimuthal constraints that can be derived from array-type processing of their hydrophone counterparts, but have the advantage of being more cost-efficient to install, operate, and maintain.

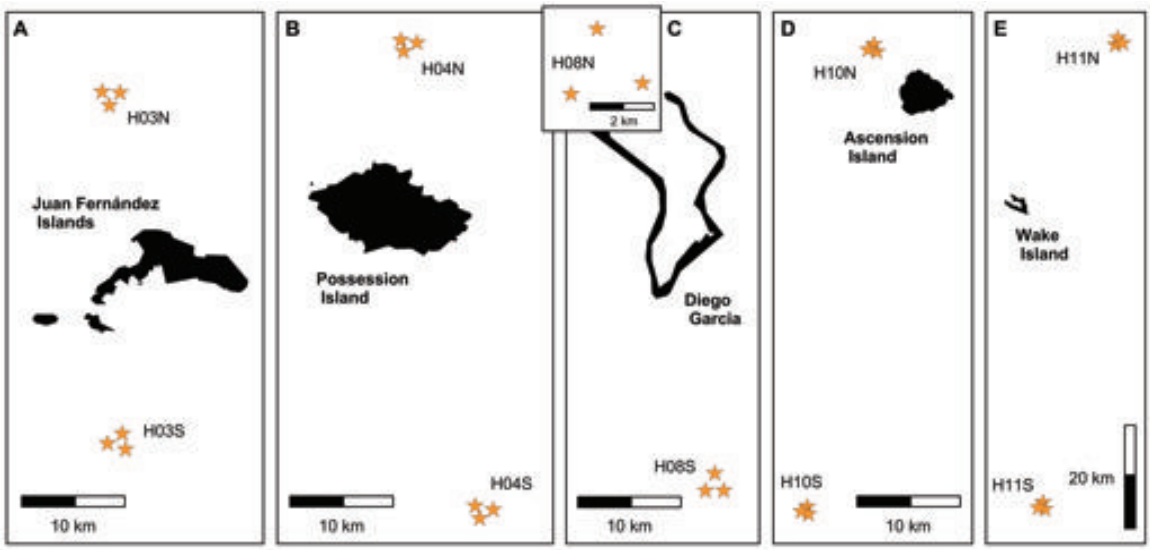

Figure 1.8: Hydrophone stations of the IMS network. Triplet arrays are deployed on opposing sites of remote islands, with the last letter of the array name, normally N (north) or S (south), indicating the position relative to the shoreline. H01W, which only consists of a single triplet 150 km west of Cape Leeuwin, Australia, has been omitted for space reasons. H08N (inset) is located approximately 200 km to the northwest of the Diego Garcia archipelago.

Hydroacoustic stations must reach a minimum uptime of 97.5% to be certified and included in the monitoring network. Global coverage and high data continuity make the IMS hydrophone component a valuable asset in underwater acoustic research, in particular when requiring long-term datasets, e.g. for the study of ocean noise levels (Brown et al., 2012; Woolfe and Sabra, 2015), marine mammal vocalization (Le Bras et al., 2016), or, as shown in the here presented work, the systematic search for submarine volcanic activity. However, overall data availability can vary due to

instrument failure or loss: For example, IMS station H03 at Juan Fernández Islands, located 700 km west off the coast Chile, was destroyed in the tsunami of the 2010 Maule earthquake (Fritz et al., 2011), and, due to the remoteness of the location and the logistical complexity involved in the re-installation process, could only be repaired in 2014. Despite these difficulties, the final hydroacoustic station was installed and certified at Possession Island, Crozet Island archipelago, as recent as June 2017, thus completing the underwater network 15 years after the beginning of its installation. With the exception of the northern array at Diego Garcia (H08N) and one element of the southern array at Ascension Island (H10S), all stations are online and fully operational as of October 2017.

In this thesis, we investigate recordings from IMS hydrophones located at Ascension Island (H10), Juan Fernández Islands (H03), and Wake Island (H11). Hence, a more detailed description of these stations can be found in the Chapters 2, 3, and 4, respectively.

1.4.2 Hydroacoustic data

The CTBTOs International Data Centre (IDC) receives station recordings in near-real time via satellite uplink for routine data inspection. The sampling rate of IMS hydrophones is 250 Hz, with a flat frequency response between approximately 1 and 100 Hz. Similar to standard seismic processing, coherent acoustic phases are automatically detected by evaluating short-term (STA) and long-term (LTA) power ratios over a range of frequency bands between 2 and 80 Hz, thus extracting discrete arrivals from the incoming data stream (Hanson et al., 2001). Array-type analysis of hydrophone triplet data uses a derivative of the Progressive Multi-Channel Cross-Correlation algorithm (PMCC, Cansi, 1995) to estimate signal back azimuths, duration, energy distribution over time, and frequency content. Based on these parameters, hydroacoustic phases are classified as terrestrial ('T'), waterborne ('H'), or noise ('N'). While

arrivals marked 'T' are commonly associated with low-frequency sounds caused by earthquakes, 'H phases' are generated by in-water sources, for example explosions, and therefore are of particular interest in the context of test-ban-monitoring. Gathering results from automated processing of all three waveform technologies, a global association routine issues a first Standard Event List (SEL), which is later reduced by the application of probabilistic models and interactive analyst review in order to keep the number of inaccurate, missed or false detections at a minimum (Arora et al., 2013; Koch, 2013). The final data product, the Reviewed Event Bulletin (REB), is a comprehensive catalogue of all events identified by the IMS network.

The majority of arrivals registered by IMS hydrophones is generated by earthquakes located along mid-ocean ridges and subduction zones (Graeber and Piserchia, 2004; Hanson and Bowman, 2005b, Figure 1.9a). Icebergs often produce distinct patterns of low-frequency sound as they calve, move about, collide and break up (Figure 1.9b), enabling 'acoustic tracking' of their position across circumpolar waters (Chapp et al., 2005; Evers et al., 2013). Anthropogenic noise, for example offshore drilling, airgun shooting during seismic surveys (Figure 1.9c), and explosions due to military testing are frequently observed by IMS stations, even over megameter distances, and contribute to underwater sound levels below 100 Hz (Nieukirk et al., 2004). Local sources at distances of up to a few hundred kilometers typically include whale calls and engine noise from commercial shipping (Sousa and Harris, 2015).

Prior to the work presented here, IMS hydroacoustic data had not been extensively used to study submarine volcanic events. In fact, only one eruption had been reported in the record: In May 2010, South Sarigan Seamount, a submarine volcano in the central Mariana Arc, erupted over the course of three days, with arrivals detected by seismic, infrasound, and hydroacoustic IMS stations, including the Wake Island hydrophone arrays (Heaney et al., 2013, Figure 1.9d). Fusing data from all three waveform components, Green et al. (2013) were able to derive a detailed chronology

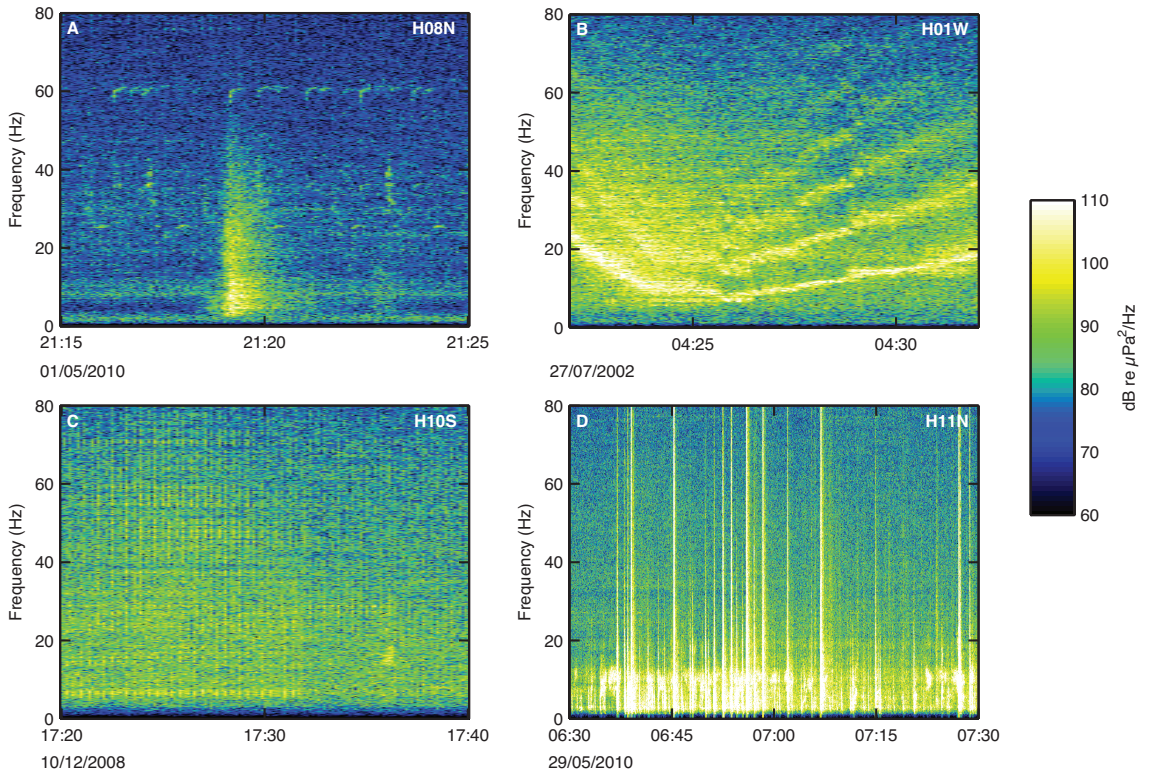

Figure 1.9: Four examples of underwater signals received by the IMS hydrophone network. Note the different time scales. (a) T phase associated with a 3.6 m_b earthquake along the Central Indian Ridge. Whale calls are observable between 25 and 40 Hz, and at around 60 Hz. (b) Ice-generated tremor from an iceberg in the Southern Ocean, as described by Chapp et al. (2005). Note the presence of distinct overtones and gliding of the fundamental between 8 and 20 Hz. (c) Seismic surveying in the equatorial Atlantic Ocean. Air gun shots are fired at 11 sec intervals, populating the entire frequency range of the hydrophone. (d) Submarine volcanic activity at South Sarigan Seamount, Mariana Arc. Individual events resemble the T phase of the tectonic earthquake shown in (a), but arrivals are more numerous and create a quasi-continuous wave train between 2 and 12 Hz, with occasional bursts up to 80 Hz and higher.

of the episode. However, so far only a fraction of submarine eruptions were detected at teleseismic distances, and in even fewer cases the volcano breached the sea surface, thus ruling out both seismic and infrasonic methods of observation. This thesis makes a first attempt to tackle the problem by exploring the potential of the IMS hydrophone network for remotely detecting volcanic activity in the global ocean, using Monowai as a natural laboratory for long-range hydroacoustic measurements of an undersea volcano.

1.5 Objectives and outlook

The main aim of this thesis is to detect and track submarine volcanic activity at Monowai by the means of long-range underwater acoustic data, as recorded by the IMS hydrophone network. Following previous findings by Watts et al. (2012), Chapter 2 investigates seismic and hydroacoustic observations associated with the May 2011 eruption at Monowai, which was detected as far away as Ascension Island in the Equatorial Atlantic Ocean. Data gathered by the IMS hydrophone array south of Juan Fernández Islands, Southeast Pacific Ocean, allows for the reconstruction of a long-term record of activity at the volcano between 2003 and 2004, and from 2014 to 2017, which is described in detail in Chapter 3. Considering results and techniques developed and implemented in the two previous chapters, Chapter 4 focuses on acoustic measurements of the 2014 submarine eruption at Ahyi Volcano, Northern Mariana Islands. A synthesis of results, final conclusions, and directions for future work are presented in Chapter 5.

The three core studies presented in this thesis each intend to make an original contribution to the fields of submarine volcanism and long-range ocean acoustics. Where applicable, the relation to content already published or submitted for peer review is stated at the beginning of the respective chapter.

Chapter 2

Ultra-long-range hydroacoustic observations of submarine volcanic activity at Monowai

A modified version of the following study has been published as

Metz, D., Watts, A. B., Grevemeyer, I., Rodgers, M., Paulatto, M. (2016),

Ultra-long-range hydroacoustic observations of submarine volcanic activity, Kermadec Arc

Geophys. Res. Lett., 43(4), 15291536, doi:10.1002/2015GL067259

2.1 Introduction

Estimations on the number of active volcanoes in the worlds oceans range from hundreds to thousands, and only a few active sites have been studied in detail due to their inherent inaccessibility. Monowai Volcanic Centre at 25.89°S, 177.18°W in the northern Kermadec Arc comprises an active submarine stratovolcanic cone, a number of parasitic cones, and a flanking caldera with a small central dome (e.g., Wormald et al., 2012; Paulatto et al., 2014). The center has a well-documented record of more than five decades of activity (e.g., Davey, 1980; Talandier and Okal, 1987), including

discolored surface water, intermittent observations of changes of seafloor depth due to on-going magmatic activity, large-scale sector collapses, and swarms of tertiary phase arrivals ('T phases') recorded at broadband seismic stations in the southwest Pacific region (Chadwick et al., 2008b; Wright et al., 2008). Repeat swath bathymetric mapping has revealed the highly dynamic nature of Monowai cone, the summit of which has shallowed by ∼67 m since 2004. Its most recent documented eruption was during 14 May to 1 June 2011, when significant morphological differences were observed aboard R/V SONNE (expedition SO215), including the development of a ∼72 m high-summit cone and a flanking sector collapse of ∼18 m (Watts et al., 2012). During this period, a 5 day long burst of T phases was recorded at broadband seismic stations on Rarotonga (Cook Islands), Papeete (Tahiti), and Marquesas Islands (Figure 2.1a), thereby directly linking seismoacoustic observations and changes in seafloor depth due to submarine volcanic activity for the first time. Apart from the Monowai Volcanic Centre, recent reports of T phases generated by submarine explosive volcanism along the wider Tonga-Kermadec area include West Mata, Hunga Haapai-Hunga, and Brothers Volcano (Dziak et al., 2008; Bohnenstiehl et al., 2014).

T phases are low-frequency sound waves that travel in the Sound Fixing and Ranging (SOFAR) channel, a distinct layer of low sound wave speed in the oceanic water column (Tolstoy et al., 1949; Ewing et al., 1951). The SOFAR channel effectively serves as an acoustic waveguide for underwater signals of various origins, with the large majority generated by earthquakes at plate boundaries, for example, along subduction zones and mid-oceanic ridge crests (Smith et al., 2002; Graeber and Piserchia, 2004). During the transition from ocean to land, the seismoacoustic signal trapped in the deep sound channel can be converted effectively and thus becomes detectable by both ocean-moored hydrophones and land-based seismometers (Stevens et al., 2001), often providing significant improvement in event detection and relocation where instrument coverage is poor (e.g., Tolstoy and Bohnenstiehl, 2005;

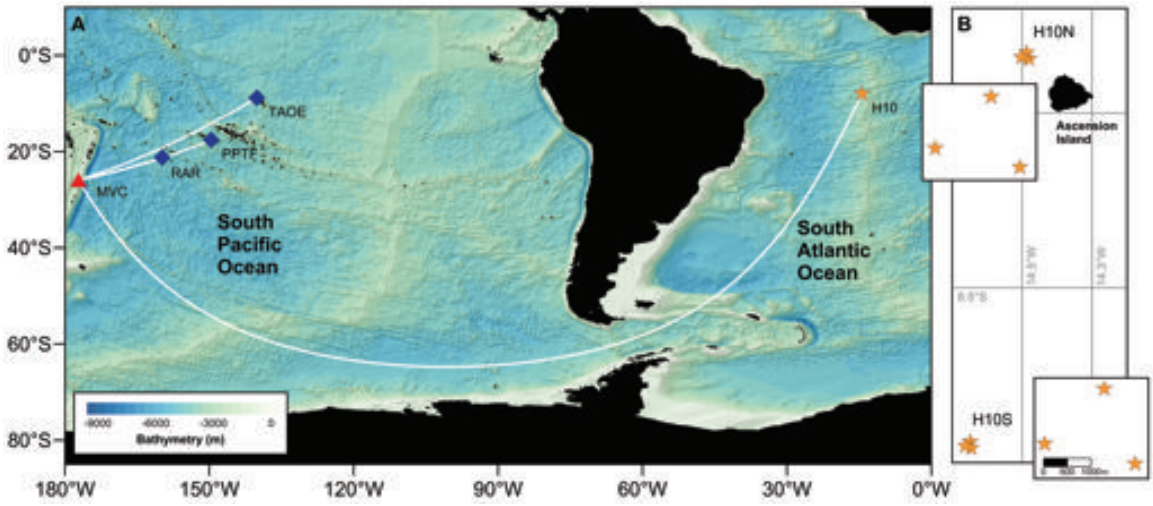

Figure 2.1: (a) Location map of Monowai Volcanic Centre (MVC, red triangle) and IMS station H10 (orange star). T phases of the May 2011 eruption were recorded at three regional broadband stations (blue diamonds) at Rarotonga (RAR), Papeete (PPTF), and Marquesas Islands (TAOE). The stations are located at 1847 km, 2991 km, and 4340 km distance from the volcano, respectively. Bathymetry is taken from the 2008 GEBCO grid. (b) Position map of the H10S and H10N hydrophone arrays near Ascension Island with insets for individual components. Geodesic distances between Monowai and the hydrophone arrays are 15,717 km (H10S) and 15,834 km (H10N).

Ito et al., 2012).

T phase seismicity is a key feature of the hydroacoustic waveform component of the International Monitoring System (IMS) that is maintained by the Comprehensive Nuclear-Test-Ban Treaty Organization (CTBTO). As of 2015, a total of ten hydroacoustic receiver sites are in operation worldwide, six of which are hydrophone triplet arrays, typically deployed near the axis of the SOFAR channel (Okal, 2001). In this study, we focus on recordings from IMS station H10 at Ascension Island, equatorial South Atlantic Ocean, the only hydrophone station in the network to record the five-day long episode of explosive activity documented by Watts et al. (2012) at the Monowai Volcanic Centre, southwest Pacific Ocean (Figure 2.1).

2.2 Hydroacoustic data and direction-of-arrival calculations

IMS Station H10 consists of two tripartite arrays of bottom-moored hydrophones located northwest and southwest of Ascension Island (Figure 2.1b). The triplets, H10N1-3 and H10S1-3, respectively, are positioned at approximately 875 m depth and equidistant inter-hydrophone spacing of 2 km. Acoustic measurements are made at 250 Hz sampling rate and transmitted in real time to the International Data Centre (IDC) in Vienna for routine processing and analyst review (Hanson et al., 2001). Following the onset of the eruption at Monowai Volcanic Centre on 17 May 2011, both H10 arrays recorded a high incidence of hydroacoustic T phases.

To determine the direction of arrival of these signals, we follow an approach previously introduced by Heaney et al. (2013) for the investigation of volcanogenic T phase arrivals associated with the 2010 eruption at Sarigan Seamount. Hydrophone recordings are corrected for instrument response and a mean and trend is removed. A two-pole band-pass filter with a low- and high-cutoff frequency of 4 Hz and 12 Hz, respectively, is applied to enhance the signal-to-noise ratio of arrivals from Monowai and to avoid noise contamination from either end of the spectrum, e.g., through ocean microseism, whale vocalization, or ship screw noise, and in general reflects the frequency range at which T phases would be expected to efficiently propagate within the SOFAR channel due to its inherent geometry (Hanson and Bowman, 2006).

Hydrophone recordings were subdivided into 1-min long windows over a continuous period of 5 days between 06:00 UTC 17 May and 06:00 UTC 22 May 2011. Peak delay times Δt are calculated from pairwise, normalized cross-correlation of the windowed data. The angle of arrival θ, which represents the geodesic back azimuth along the great circle path between receiver and source, is then derived from the peak delay times between pairs of hydrophones positioned at distance d and averaged over

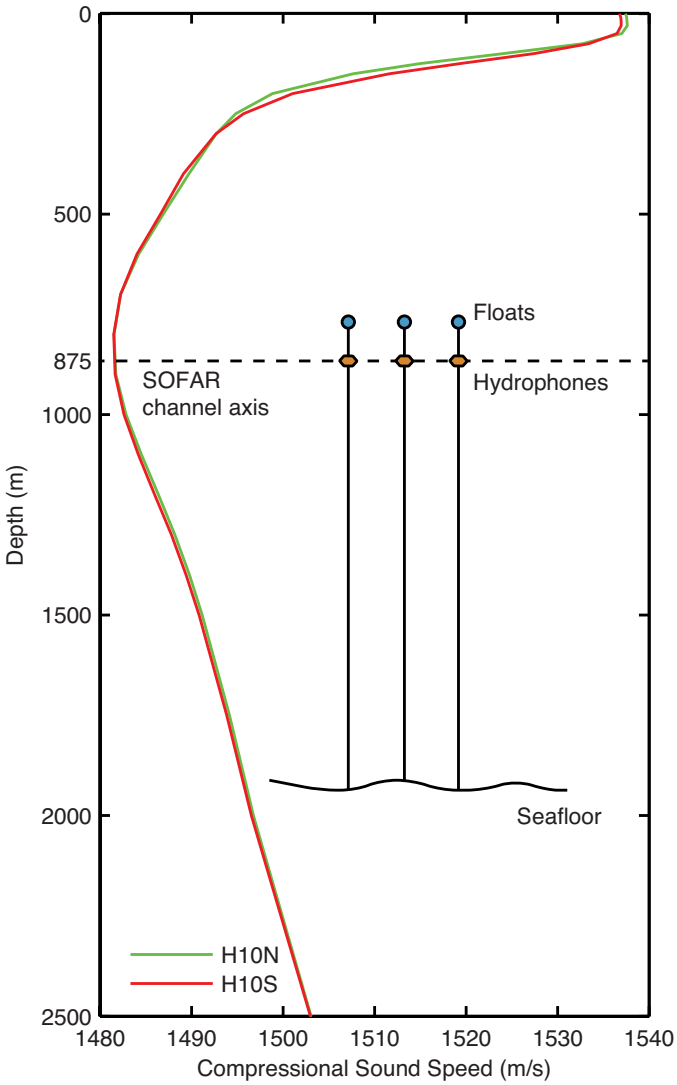

Figure 2.2: Vertical sound speed profiles at H10S and H10N and schematic outline of the instrument setup of one hydrophone triplet array. The profiles show distinct minima of 1482 m/s at ∼875 m depth, which corresponds to the local depth of the SOFAR channel axis and the average mooring depth of the hydrophones. Water column data is taken from the 2001 World Ocean Atlas.

the array. Since the spacing of the array elements (i, j) is multiple orders of magnitude smaller than the source-receiver distance and temperature variations between hydrophones are expected to be minimal (cf. Evers and Snellen, 2015), we can assume a planar wave front for a point source in the acoustic far field:

$$\theta_{i,j}\left(\Delta t\right) = cos^{-1}\left\{\frac{c\Delta t}{d_{ij}}\right\} \tag{2.1}$$

where v is the propagation speed across the array. Geometric ambiguity of the inverse cosine function is resolved by an a priori estimation of both the signal source location and v, which can be inferred from local water column data and is fixed at 1482 m/s for the H10 station (Figure 2.2). Only time windows with an average correlation coefficient greater than 0.33 are used in (2.1) to eliminate weakly correlated arrivals below background noise levels.

2.3 Observations at the Ascension Island array

Our calculations show that volcanic activity at the Monowai Volcanic Centre stabilizes back azimuths over an approximately 5 day long period, representing a persistent source of acoustic energy at both arrays of the Ascension Island station.

The onset of the eruption at 09:00 UTC on 17 May is clearly recognizable in the spectrogram of hydroacoustic measurements, shown for the southern array in Figure 2.3a. Here one of the most striking features is a continuous, low-level noise band in the 18-25 Hz range, which we attribute to marine mammal vocalization in the area. T phases are most notable in the 2-20 Hz range, with lengths of tens of seconds up to several minutes and average acoustic intensities of 100 to 110 dB re 1 μPa^2/Hz. Maximum levels of 125 dB re 1 μPa^2/Hz are reached during minute-long bursts of broadband, high-frequency energy, ranging up to 40 Hz and more. These arrivals occur predominantly during the first 48 h of the eruption at rates of up to 10 per

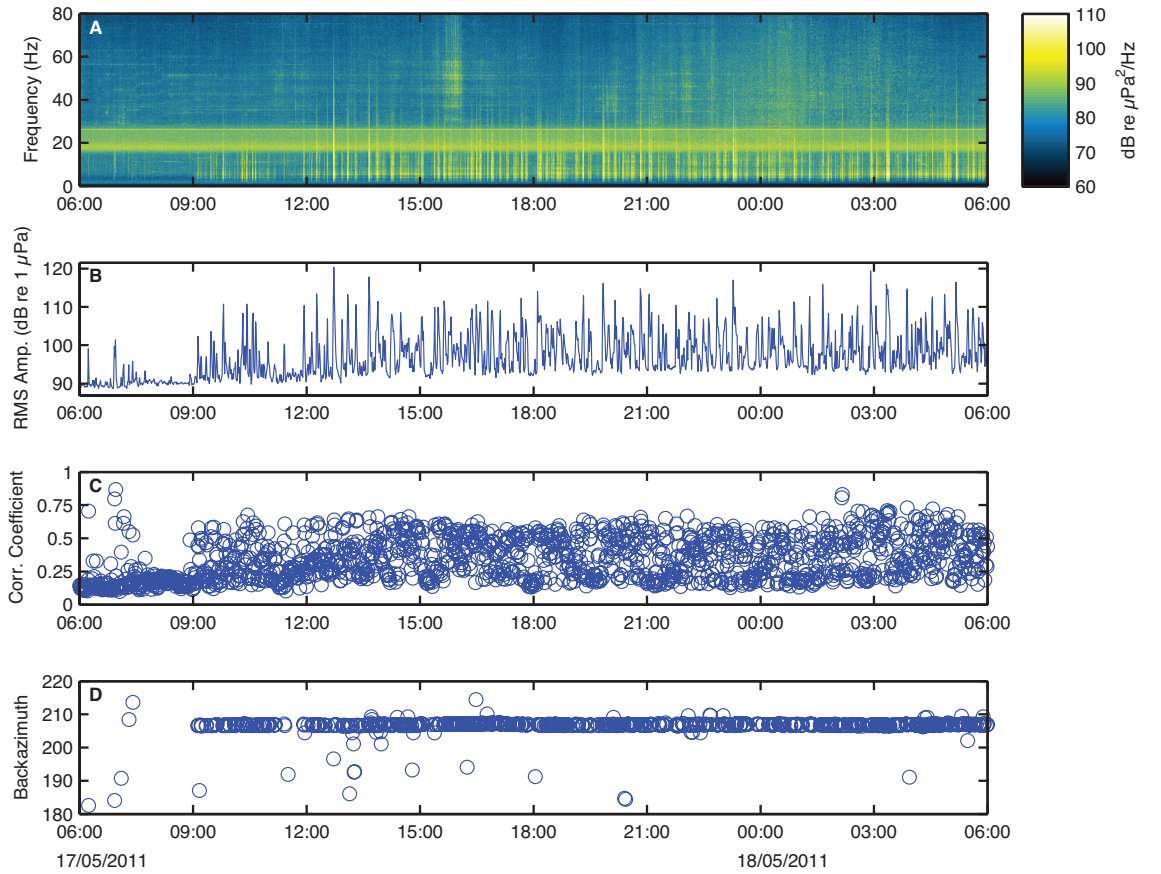

Figure 2.3: Data recorded at array H10S, beginning at 06:00 UTC 17 May 2011 showing the onset of explosive activity at Monowai. (a) Single-receiver spectrogram of the H10S1 hydrophone data. A 2 Hz high-pass filter is applied to eliminate low-frequency noise; however, wide-band contamination is present between 18 and 26 Hz, possibly due to whale calls. Note that the high-pass filter of 2 Hz, chosen to visualize the full dynamic range of the hydrophone recordings, differs from the 4-12 Hz processing band. (b) Root-mean-squared (RMS) amplitudes calculated over 1 min windows. The results of the time-difference-of-arrival processing are shown in the form of (c) correlation coefficients and (d) back azimuths averaged over the H10S array. Only time windows with an average coefficient ≥ 0.33 are used in the back azimuth calculation. The onset of the eruption at Monowai is recognizable in all four subfigures: Hydroacoustic phases, most distinguishable in the 2 to 20 Hz band, arrive from 09:00 UTC onward, accompanied by a positive shift in RMS amplitude of almost 20 dB re 1 μPa. Correlation values between hydrophones increase significantly at the same time, resulting in the distinct stabilization of the angle of arrival to within a degree of the predicted back azimuth to Monowai at 205.5°. Acoustic phases from Monowai are preceded by a T phase of distinctly lower frequency and amplitude at approximately 07:00 UTC, most likely corresponding to a mid-ocean ridge earthquake.

hour, most likely representing explosions at the magma-water interface (Chadwick et al., 2008a). With the beginning of the eruption, peak RMS values increase by almost 20 dB compared to pre-eruptive background levels (Figure 2.3b). Average correlation coefficients of the windowed hydrophone data rise sharply above the local noise floor, scattering between 0.25 and 0.8 from 17 May 09:00 UTC onward (Figure 2.3c). The angle of arrival simultaneously stabilizes around 206.5 ± 0.2° during the first 24 h of the eruption, which closely matches the predicted geodesic back azimuth to Monowai (205.5°), and clearly indicates a signal source between IMS Station H10 and the volcanic center (Figure 2.3d). While variations of up to 0.5° in signal back azimuth have been observed at other IMS triplet arrays as a result of instrument drift and changes in the near-receiver temperature regime (e.g., Hanson and Bowman, 2006; Nichols and Bradley, 2016), we further attribute the systematic offset of up to 1° from the geodesic value to the refraction of acoustic phases, induced, for example, by horizontal sound speed gradients or bathymetric interference along the source-receiver path (Munk and Zachariasen, 1991; de Groot-Hedlin et al., 2009).

The end of the eruptive episode occurs around 13:00 UTC on 22 May, when calculated back azimuths become more scattered, before cross-correlation coefficients drop beneath the detection threshold of 0.33 at 16:00 UTC (Figure 2.4). There are several pauses in activity over the course of the 5 days, ranging from tens of minutes up to a notable longer break on 21 May, when less than 30 1-min windows are detected between 00:00 and 06:00 UTC. However, the high incidence of T phase arrivals and the partial overlap of individual events and their codas result in a quasi-continuous character of the signal during most of the time, adding up to an acoustic signature that is best described as low-level, volcano-seismic tremor interspersed with explosive activity (see, e.g., Fox et al., 2001).

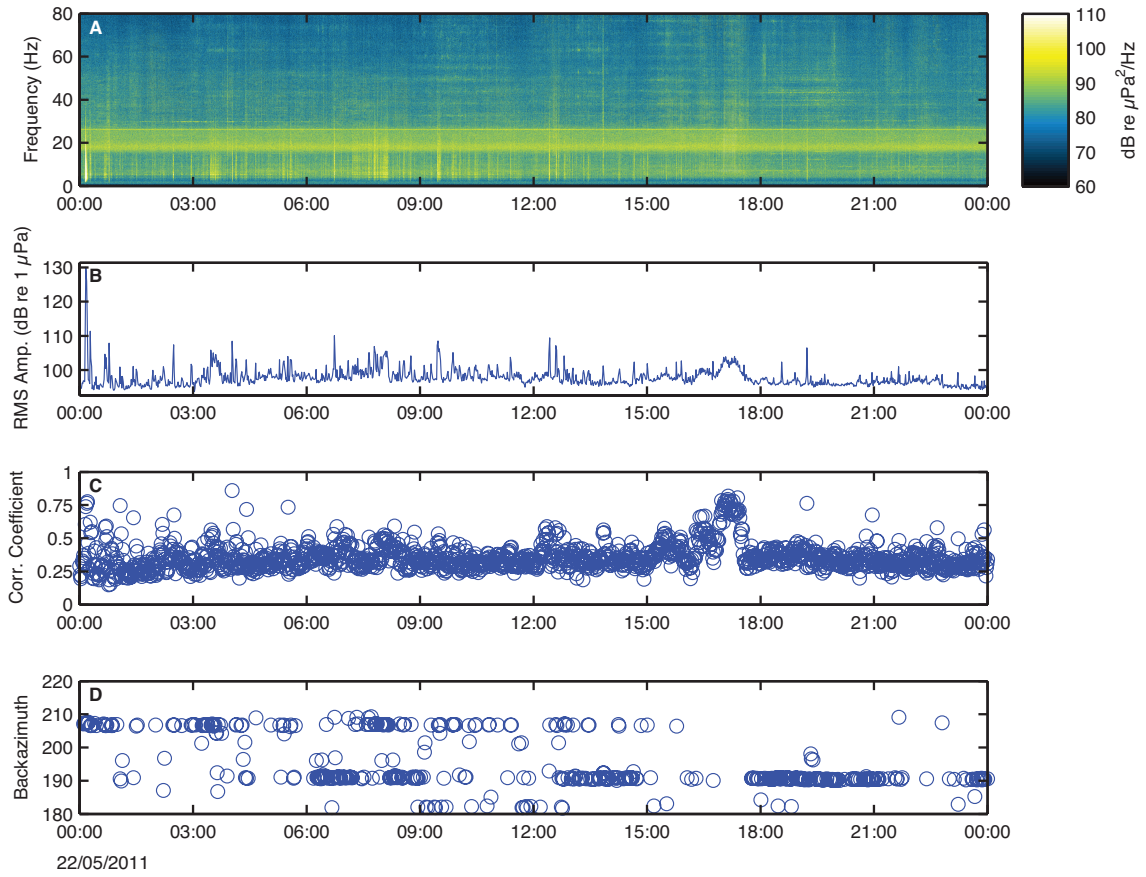

Figure 2.4: Beginning at 00:00 UTC 22 May 2011, data in (a-d) shows the end of the eruptive burst recorded at H10S. The same processing parameters apply as in Figure 2.3. RMS amplitudes and correlation coefficients are significantly lower than at the beginning of the eruption. Since the geometrical approach described in (2.1) is unable to distinguish between competing signals that reach the array simultaneously from different directions, the final stage of the eruption is partially range-overlaid, potentially by shipping noise incoming from ∼190°. The end of the main eruptive burst occurs at around 13:00 UTC on 22 May, with a last high-energy impulse at about 13:30 UTC, followed by a gradual fade-out of activity between 14:00 and 16:00 UTC.

2.4 Combining hydroacoustic and broadband seismic data

In order to confirm the azimuthal constraints of the direction-of-arrival calculations, we relate acoustic and seismic measurements in both the near field and far field in an effort to unambiguously identify volcanic activity at the Monowai Volcanic Centre as the primary signal source. T phase arrivals associated with the May 2011 eruption were detected at three seismic broadband stations at Rarotonga (RAR), Papeete (PPTF), and Marquesas Islands (TAOE) in the Pacific Ocean (Figure 2.1). However, both PPTF and TAOE seismic data are affected by high ambient noise levels during the time of the eruption, preventing the application of common relocation techniques for individual T phase events (Williams et al., 2006). Instead, we exploit relative travel time differences between the proximal RAR station and a single, distant H10 hydrophone element for our calculations.

Assuming a signal source at Monowai and a constant axial propagation speed of 1475 $\pm$ 3 m/s, a reasonable estimate for the sound speed average along the geodesic path between the volcano and Ascension Island (Munk and Forbes, 1989), nominal arrival time offsets between these two receiving stations are estimated at 156 min 43 $\pm$ 21 s. Stacking the traces according to this offset (Figures 2.5a and 2.5b) reveals a striking visual coherence between the signals, precisely aligning higher-amplitude phases and periods of quiescence. Individual T phase events appear similar in both time and frequency domains (Figures 2.5c and 2.5d). This is despite the possibility that higher frequencies tend to be lost during the ocean-land conversion process at the RAR station (Stevens et al., 2001).

In a further step to remove any ambiguity regarding the source, envelope functions are calculated from normalized RMS amplitudes for the H10S1 hydrophone and the vertical component of RAR station. There is a notable visual coherence between

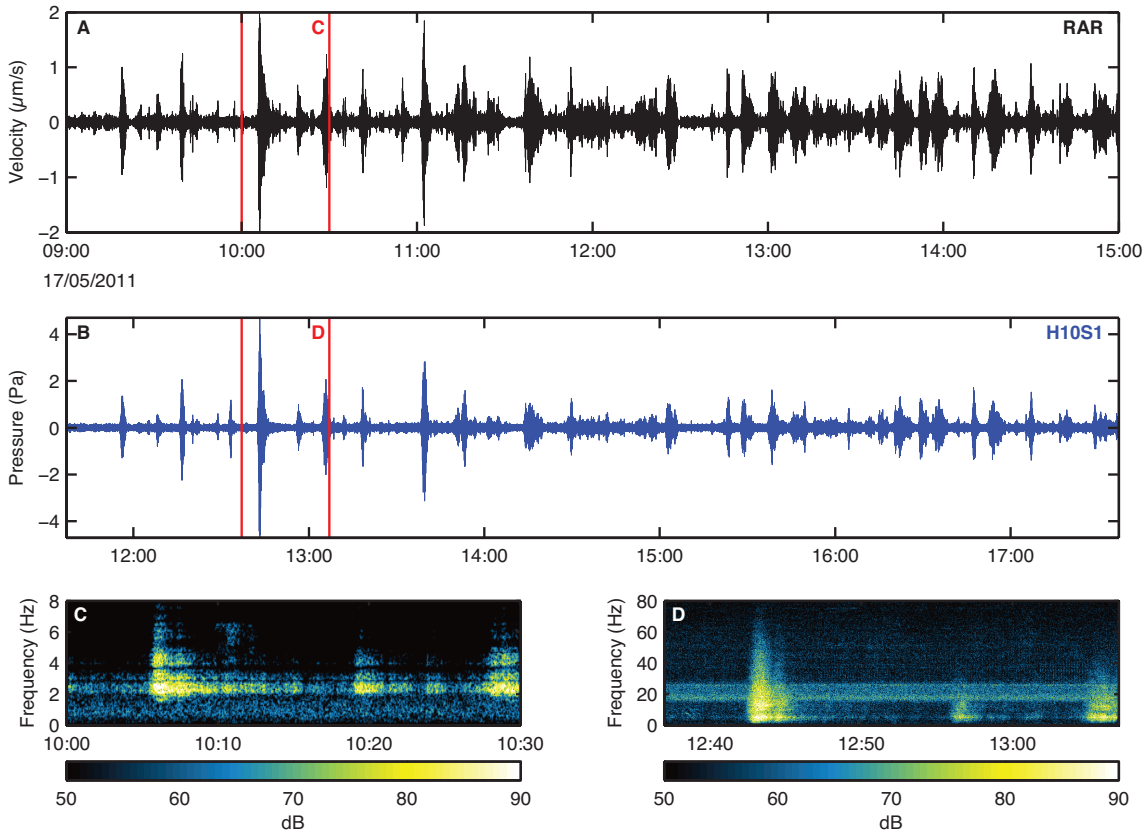

Figure 2.5: Traces of the (a) RAR vertical seismometer component and (b) hydrophone H10S1. The data are recorded at 20 Hz sampling rate at RAR and 250 Hz at H10S1, band-pass filtered at 2-6 Hz and 4-12 Hz, respectively, and show arrivals during 6 h long periods on 17 May 2011. Traces are aligned for an offset of 156 min and 12 s, the nominal travel time difference between the two receivers for a presumed signal source at Monowai. Vertical red lines delimit the time range of 30 min spectrograms of land-recorded T phases and corresponding arrivals at H10S1 as shown in Figures 2.5c and 2.5d. (c and d) The dB scale is normalized for better comparability and does not reflect absolute physical quantities. Spectral data are high-pass filtered at 2 Hz. There is a striking visual coherence between the signal envelopes in Figures 2.5a and 2.5b and relative frequency distributions of the individual bursts in Figures 2.5c and 2.5d, respectively.

the two signals (Figure 2.6a), and cross-correlation of the envelope functions from RAR and H10S1 shows a high degree of correlation (Figure 2.6b). Twenty-four hour time windows were chosen for cross-correlation as this is approximately 10 times the expected delay time between the two stations. The highest cross-correlation coefficient of the eruption is observed during the first 24 h window, with a cross-correlation coefficient of 0.92 at a lag of 157 ± 1 min (Figure 2.6b). The high level of correlation is attributed to the large number of high-amplitude, coherent arrivals during this time. This calculation is in agreement with the calculated delay time assumed in Figure 2.5 (156 min 43 ± 21 s) and confirms our initial assumption of a common signal source at Monowai.

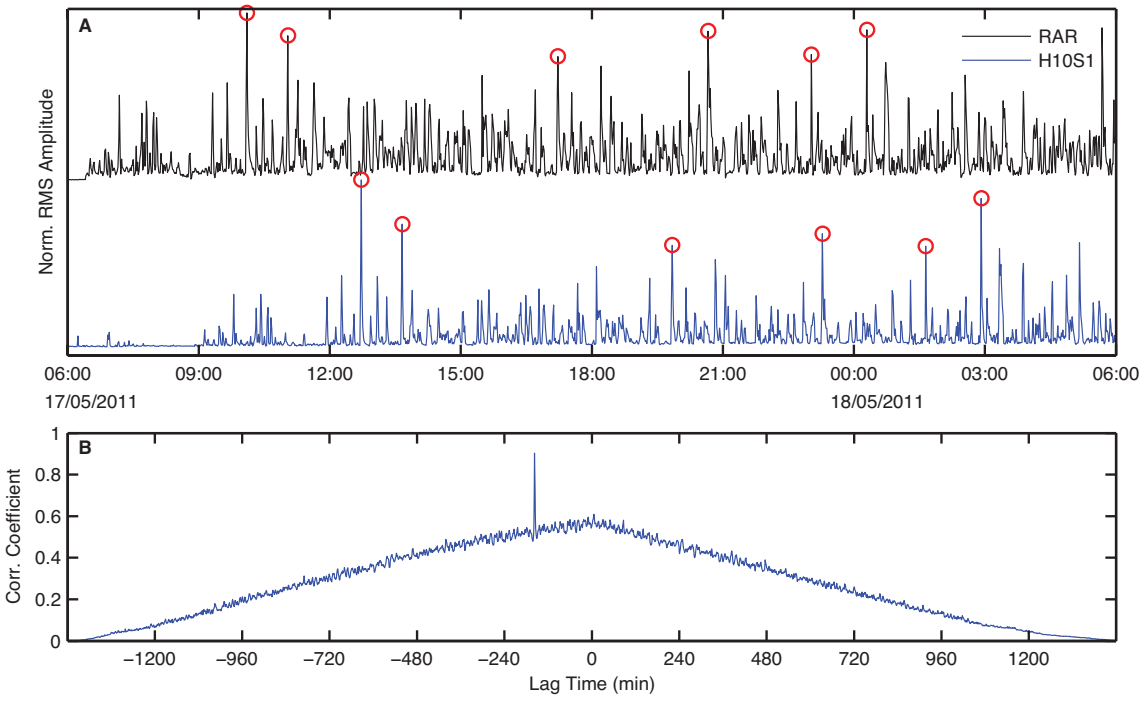

Figure 2.6: (a) Normalized RMS amplitudes at the RAR seismic station (vertical component) and the H10S1 hydrophone, calculated for 1 min windows between 06:00 UTC 17 May and 06:00 UTC 18 May. The data are band-pass filtered at 2-6 Hz and 4-12 Hz, respectively. Red circles highlight corresponding RMS peaks for clarity. (b) Cross-correlation results of data in Figure 2.6a. The distinct 0.92 peak marks the maximum coefficient of this 24 h period. The corresponding delay time is 157 min, indicating that the signal arrives 2 h and 37 min earlier at the Rarotonga seismometer relative to the Ascension Island hydrophone.

Our observations are equivalent for both the H10S and H10N hydrophone array, located at great circle distances of 15,717 and 15,834 km respectively from Monowai. These are, to our current knowledge, the longest ranges ever reported for any naturally occurring underwater phenomena and are only superseded by the artificial source-receiver paths achieved during the 1991 Heard Island Feasibility Test (Munk et al., 1994). The significant coherence observed between the seismic and hydrophone recordings further suggest that the overall seismoacoustic structure of the eruption is conserved in the T phase signal, even over extremely long distances and propagation through different media. Nonetheless, it is important to note that seismoacoustic activity associated with the May 2011 eruption at Monowai was not detected at other sites in the southern Pacific or Atlantic Ocean, including two broadband stations located on Ascension Island itself. This illustrates, at least for the case of volcanic activity at the Monowai Volcanic Centre, the advantage of a sensitive, acoustically 'quiet' hydrophone array over single-element, land-based instruments.

Our approach holds true for subsequent eruptions at the Monowai Volcanic Centre. On 1 January 2013, a swath mapping campaign of the SO225 expedition aboard R/V SONNE had to be aborted due to a sudden increase in volcanic activity, including observations of surface-reflected shockwaves in the audible range, pumice rafts, and discolored water (Werner et al., 2013). A preliminary screening of the Ascension Island hydrophone data reveals persistent high-energy arrivals from a back azimuth of 205.5° for this time period, which in overall frequency content, spatial and temporal distribution strongly resembles our observations of the May 2011 eruption.

2.5 Investigation of potential bathymetric blockage and transmission loss modeling

Long-distance hydroacoustic propagation can be affected by bathymetric obstruction and range-dependent sound speed variations (Blum and Cohen, 1971). Furthermore, the existence of a deep sound channel is not facilitated at southern latitudes, where water masses at critical depths are dominated by the temperature regime of the Antarctic Circumpolar Current (ACC, Denham and Kibblewhite, 1970). Using an adiabatic equation model (RAM, Collins, 1993) to account for the range-dependence of both ocean stratification and seafloor topography, we therefore investigate the source-receiver path by calculating the full sound field over the geodesic profile between Monowai and the Ascension Island hydrophones (Figure 2.7).

In order to reflect the prevailing frequency content of the T phase arrivals observed at H10S, we assume an 8 Hz source, placed at 60 m below sea level, which is in accord with the most recent estimates of summit depth at Monowai (Watts et al., 2012). The nominal great circle distance is 15,717 km for the southern triplet array. Potential obstructions along the acoustic ray path include the Louisville Ridge seamount chain as well as the Pacific- Antarctic Mid-Oceanic Ridge, the Scotia Sea Ridges, the Maurice Ewing Bank, the eastern Rio Grande Rise, and the southern Mid-Atlantic Ridge.

Our modeling shows that the most severe transmission loss occurs near the Louisville Ridge seamount chain, where the crest of one of the seamounts in the chain intersects the SOFAR channel axis and the signal is partially blocked, resulting in an average reduction of 20 to 25 dB re 1 μPa. A similar effect would be expected for the area around the North Scotia Ridge and Maurice Ewing Bank, where seafloor depths are shallowest along the profile. However, the RAM model suggests that acoustic phases partially propagate as surface reflected waves south of the 60°S parallel, thereby evad-

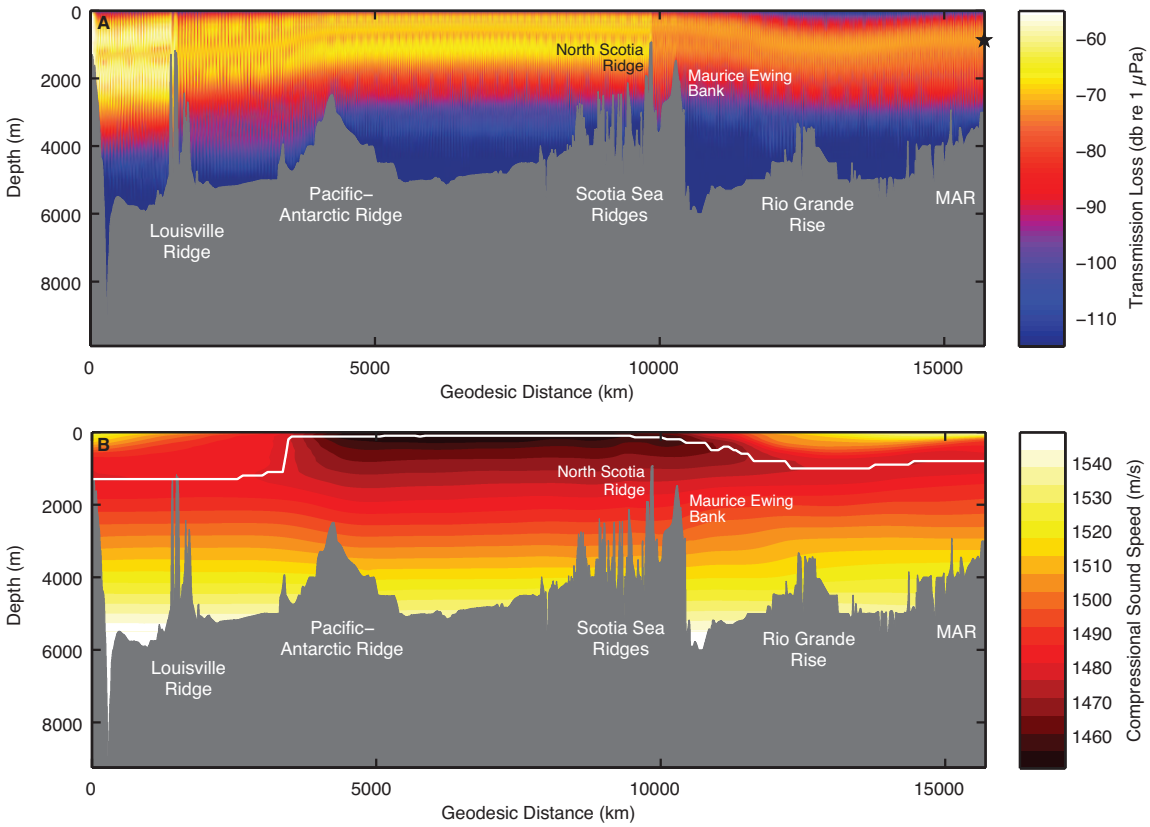

Figure 2.7: Range-dependent transmission loss and sound speed variation. (a) Two dimensional parabolic equation model (RAM, Collins, 1993) for a source-receiver path between Monowai Seamount and H10S. The model assumes an 8 Hz source at 60 m depth, corresponding to the dominant frequency of hydroacoustic arrivals and the bathymetry of the volcano. Apart from the Louisville and North Scotia Ridge, located at km 1500 and km 9500 along the profile respectively, ray paths along the SOFAR channel axis experience little obstruction and appear to be limited only by the sea surface in southern latitudes. Transmission loss for a receiver (black star) at 875 m depth is estimated to be ∼75 dB re 1 μPa. Bottom properties are set to 1700 m/s for sound speed, with attenuation parameters of 0.3 and 3.5 dB/m/kHz at 100 and 300 m below the seafloor respectively (Kibblewhite, 1989). (b) Compressional sound speed between Monowai Seamount and the southern triplet array. The white line shows the sound speed minimum at 100 m increments along the profile and roughly represents the ray path along the axis of the SOFAR channel. The path partially intersects with a Louisville Ridge seamount at ∼2000 km, but evades either of the ridges near km 10,000 due to its gradual shoaling in Antarctic waters, where the distinct minimum velocity zone caused by the cold circumpolar currents is clearly visible. In both figures, bathymetry is taken from the 2008 GEBCO grid, sampled at 100 m intervals. Water column data is taken from the 2001 World Ocean Atlas, with sound speed profiles calculated every kilometer according to Mackenzie (1981).

ing bathymetric obstruction and reducing the average effect of acoustic blockage to ∼10 dB re 1 μPa. This upward shift of the axis of the SOFAR channel is facilitated by the temperature anomaly of the ACC, which dilutes vertical sound speed gradients in the upper layers and subsequently raises the minimum velocity zone to shallower depths of up to 300 m and less (e.g., Northrop and Colborn, 1974; de Groot-Hedlin et al., 2009). Similar effects of range-dependent temperature variations on high-latitude acoustic propagation have been previously observed by Chapp et al. (2005), enabling long-distance detection of iceberg-generated tremor in the southern Indian Ocean.

Overall transmission loss along the wider sound channel axis varies between 60 and 90 dB re 1 μPa. Transmission loss at the receiver depth of 875 m at full distance averages around 75 dB re 1 μPa. This implies maximum source levels of circa 205 dB re 1 μP at 1 m at Monowai, which is comparable to amplitudes of explosive activity reported at NW-Rota 1 or West Mata volcano by Chadwick et al. (2008a) and Dziak et al. (2015). Derived source levels correspond to seismic events with body wave magnitudes of $m_b \leq 2.0$ (Fox et al., 2001), a size which appears typical for submarine explosion-type systems (e.g., Dziak et al., 1996), but generally is too small to be detected by conventional methods in remote regions by a sparse global network.

In order to further investigate the effect of the ACC on SOFAR propagation between Monowai and the Ascension Island hydrophones, we also calculate a range-independent scenario, which assumes the same model parameters, but a generic mid-latitude sound speed profile similar to the one shown in Figure 2.2. As the sound channel axis is now fixed at 1200 m and lacks the upward shift induced by the temperature anomaly of the ACC, signal attenuation at southern latitudes and across the North Scotia Ridge increases by ∼20 dB, thus relegating transmission loss at full distance to ∼95 dB re 1 μPa (Figure 2.8). As measured RMS amplitudes of signals from Monowai typically fall within 20 dB of background noise levels (cf. Figure 2.3b

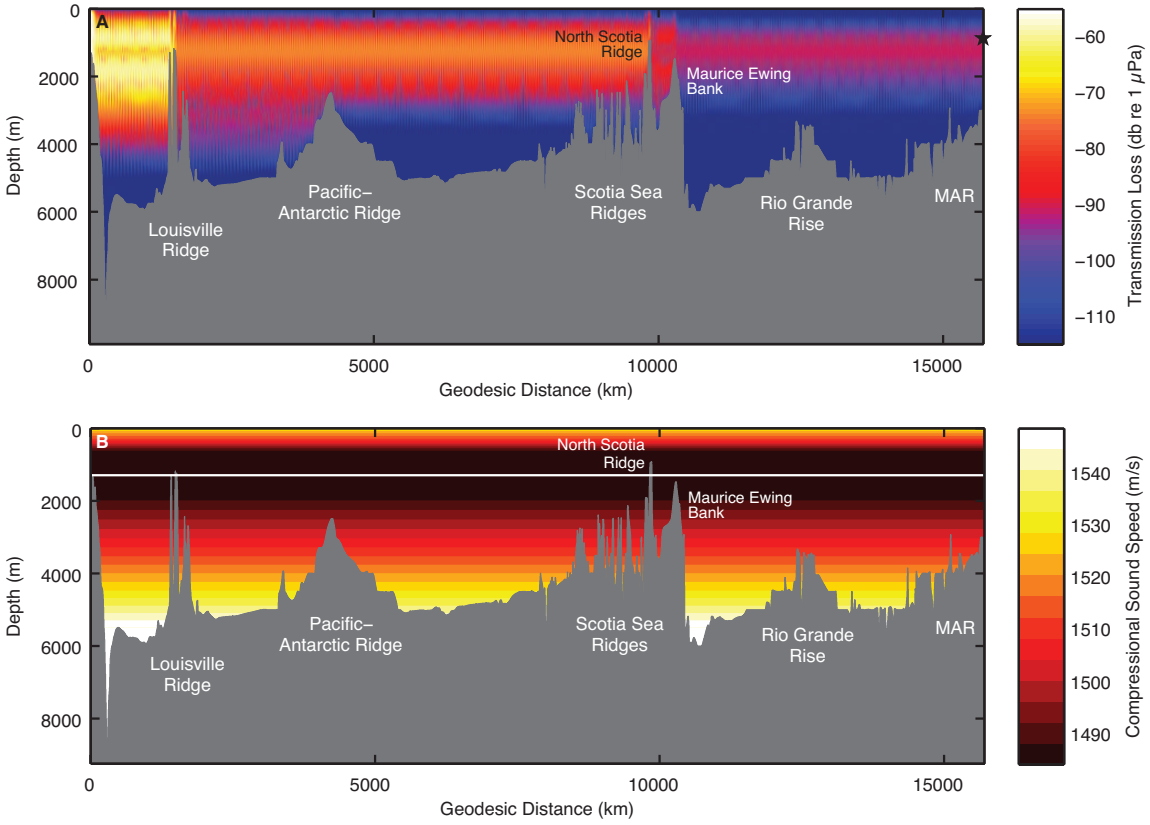

Figure 2.8: Range-independent transmission loss and sound speed variation. (a) All RAM model specifications and input data are identical with those described in Figure 2.7, except for the sound speed profile. Transmission loss for a receiver (black star) at 875 m depth is estimated to be ∼95 dB re 1 μPa, approximately 20 dB higher than in the range-dependent propagation scenario shown in Figure 2.7. Attenuation is particularly higher at southern latitudes and across the Scotia Sea Ridges. (b) The sound speed profile is constant along the entire source-receiver path. The profile corresponds to the annual mean of a typical mid-latitude location as shown in Figure 2.2. The sound channel axis (white line) lies at approximately 1200 m, now intersecting both the Louisville and North Scotia Ridge.

and 2.4b) and hence tend to be smaller than the calculated increase in transmission loss, we conclude that in absence of a low-temperature circumpolar current, long-range detection of acoustic phases from Monowai at Ascension Island may not have been possible.

2.6 Summary

Acoustic phases associated with a 5-day long episode of submarine volcanic activity at the Monowai Volcanic Centre were detected on CTBTO hydrophone installations at Ascension Island, Mid-Atlantic Ocean. The geodesic source-receiver path of approximately 15,800 km is, to our knowledge, the longest ranging, and naturally occurring hydroacoustic signal above 1 Hz ever observed in the worlds oceans. Our observations are consistent with the timing of T phase arrivals at the Rarotonga broadband seismic station for a source at Monowai. They are also consistent with the results of two-dimensional adiabatic mode calculations based on the RAM Parabolic Equation which suggest that hydroacoustic signals partially travel as surface reflected phases at shallow depths in the southern oceans, thereby avoiding significant acoustic blockage by topographic obstacles during the transition from Pacific to Atlantic waters. Our findings highlight the exceptional capabilities of the International Monitoring System of the CTBTO and its potential for remotely detecting further episodes of submarine volcanic activity and therefore better understanding the dynamics of the seafloor, both at Monowai and elsewhere, in the future.

Chapter 3

Tracking submarine volcanic activity at Monowai: Constraints from long-range hydroacoustic measurements

A modified version of the following study has been submitted for peer review with the *Journal of Geophysical Research: Solid Earth* as

Metz, D., Watts, A. B., Grevemeyer, I., Rodgers, M.,

Tracking submarine volcanic activity at Monowai: Constraints from long-range hydroacoustic measurements

3.1 Introduction

Little is known about the rates of submarine arc volcanism. Continuous surveys of known volcanoes are hindered by their remoteness and the inherent inaccessibility of the ocean environment for conventional monitoring techniques, for example satellite

altimetry, thermal imaging, or measuring atmospheric gas fluxes (e.g., Calkins et al., 2008; Mather et al., 2012). Hence, the location and timing of eruptions remain poorly constrained, and few active sites along submarine arcs have been studied over longer timescales (Embley et al., 2006; Schnur et al., 2017). Here, we attempt to overcome these observational limitations by using long-range underwater sound waves to study volcanic activity at Monowai, a submarine volcano in the Tonga-Kermadec Arc.

Located at 25.89°S, 177.18°W in the northern Kermadec Arc, Southwest Pacific Ocean, Monowai is a known example of on-going submarine volcanic activity. The edifice consists of an active stratovolcanic cone, rising from approximately 1200 to 100 m below sea level, and a flanking caldera of approximately 10 km in diameter (Wormald et al., 2012; Paulatto et al., 2014). There is a diverse record of activity at Monowai, including direct observations of discolored surface water, gas emissions, and pumice rafts (Davey, 1980). In one instance, activity was inferred from changes in sea surface chlorophyll and particulate matter content, as nutrient-rich fallout from the volcano had significantly increased local phytoplankton concentration (O'Malley et al., 2014). Further observations include onsite recordings of acoustic shockwaves (Werner et al., 2013) as well as hour to day-long swarms of T phases registered by seismometers in the Southwest Pacific region (Talandier and Okal, 1987). Swath bathymetric mapping has revealed the dynamic topography of the stratocone, which has undergone repeated phases of growth and collapse on the order of tens of meters over the past two decades (Chadwick et al., 2008b; Wright et al., 2008). During the most recent documented eruption in May 2011, a five days long burst of T phases, recorded at broadband seismometers at Rarotonga (Cook Islands), Papeete (Tahiti) and Nuku Hiva (Marquesas Islands), could be linked to the growth of a 72 m summit cone and a flanking sector collapse of 18 m (Watts et al., 2012). Furthermore, it has been shown that long-range underwater sound waves associated with the same volcanic episode have been remotely detected by a hydrophone array near Ascension

Island in the southern Equatorial Atlantic Ocean, over a geodesic range of 15,800 km (Metz et al., 2016). Activity at Monowai may have occurred as recently as October 2014 and May 2016, when seismic amplitudes at Rarotonga station rose for multiple days and discolored water was reported during flyovers conducted by the Royal New Zealand Air Force (Global Volcanism Program, 2017a).

Low-frequency underwater sound travels in the Sound Fixing and Ranging (SOFAR) channel, a distinct layer of minimum acoustic velocity in the oceanic water column (Tolstoy et al., 1949; Ewing et al., 1951). Earthquakes along active plate boundaries, i.e. mid-ocean ridges and subduction zones, are frequent sources of underwater sound signals that can be detected over hundreds to thousands of kilometers (Smith et al., 2002; Graeber and Piserchia, 2004). Hydroacoustic observations also include recordings of volcanic activity, in particular along the submarine arcs of the western Pacific region, for example at Fukutoku-Okanoba in the Volcano Islands (Dziak and Fox, 2002), South Sarigan in the Mariana Arc (Green et al., 2013), or Hunga Haapai-Hunga Tonga volcano in the Tonga-Kermadec Arc (Bohnenstiehl et al., 2013). Acoustic phases can be converted effectively during the transition from ocean to land, thus becoming detectable by both hydrophones and land-based seismometers (Stevens et al., 2001). Due to the efficient propagation of low-frequency underwater sound even over megameter distances, such seismoacoustic arrivals, also known as seismic tertiary waves or 'T phases', can be used to improve earthquake detection and relocation, especially where monitoring by conventional methods is not feasible (Helffrich et al., 2006).

Long-range propagation of low-frequency underwater sound phases is a key feature of the hydroacoustic waveform component of the International Monitoring System (IMS). As part of the verification regime for the Comprehensive Nuclear-Test-Ban Treaty (CTBT) of 1996, the objective of the IMS hydrophone network is to globally detect underwater nuclear explosions, but the comprehensive installation also

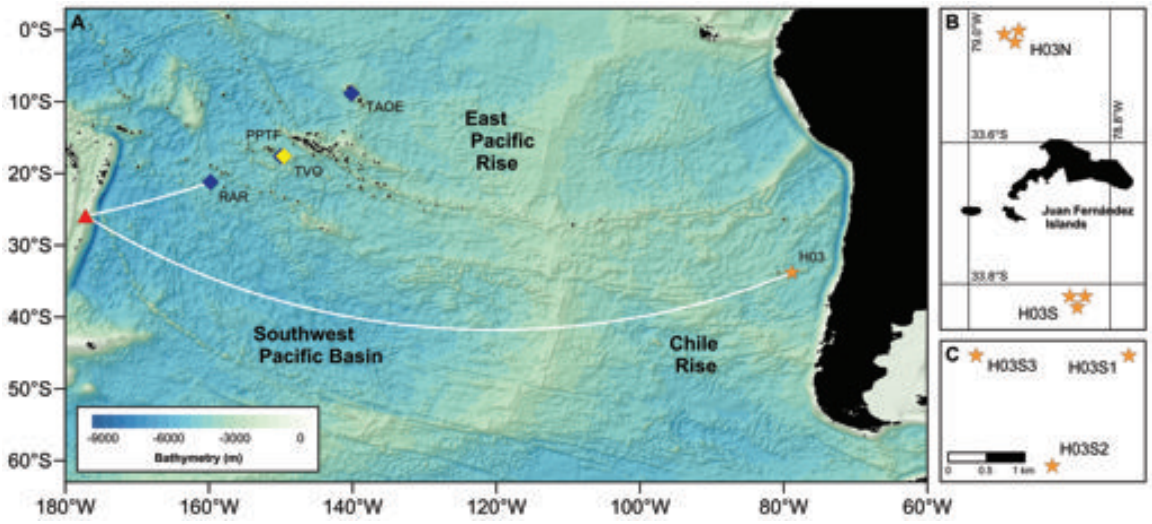

Figure 3.1: (a) Overview map of the Monowai Volcanic Centre (red triangle), IMS station H03 (orange star) and the three broadband seismic stations (blue diamonds) at Rarotonga (RAR), Tahiti (PPTF), and Marquesas Islands (TAOE). The stations are located at 1847 km, 2991 km, and 4340 km respectively from the volcano. Taravao station (TVO) of the Polynesian Seismic Network (yellow diamond) is also located at Tahiti. The white lines mark the two main source-receiver paths referred to in the methodology of this study (Sections 2 and 3). (b) Position map of the two hydrophone arrays at Juan Fernández Islands, moored approximately 15 km offshore to the north (H03N) and south (H03S). (c) Configuration of the southern H03 hydrophone array. The geodesic distance between Monowai and the triplet is 9165 km.

enables the study of natural phenomena, including, amongst others, earthquake rupture propagation (Guilbert et al., 2005; Tolstoy and Bohnenstiehl, 2005), tsunami signals (Matsumoto et al., 2016), ocean acoustic propagation (Evers and Snellen, 2015), and marine mammal vocalization (Le Bras et al., 2016; Ward et al., 2017). A total of eleven hydroacoustic receiver sites are in operation worldwide, six of which are hydrophone triplet arrays, typically deployed at remote ocean islands and near the SOFAR channel axis. Here, we focus on recordings from IMS station H03 at Juan Fernández Islands, located approximately 700 km off the coast of Chile, where episodes of volcanic activity at Monowai can be detected from across the southern Pacific basin (Figure 3.1a).

3.2 Hydrophone triplet data and processing

3.2.1 Data availability and instrumentation

Station H03 of the International Monitoring System consists of two bottom moored hydrophone arrays, located approximately 15 km north (H03N) and south (H03S) of Isla Robinson Crusoe, the easternmost island in the Juan Fernández archipelago (Figure 3.1b). The southern array was in operation from July 2003 to March 2004, when data transmission ceased due to a cable failure. After the loss of the remaining installation in the tsunami following the 2010 Maule earthquake (Fritz et al., 2011), the array became fully operational again in April 2014, thus providing a record of approximately 3.5 years for the 2003-04 period and from April 2014 to January 2017. Since its first installation in 2003, H03S has exceeded its designated uptime of 97.5%, with only nine days of the entire record being omitted from our calculations due to missing or corrupted data. The three hydrophones, H03S1-3, are moored near the SOFAR channel axis at 830 m water depth (Appended Figure A.1), with elements organized in a tripartite configuration and at an equidistant spacing of 2 km (Figure 3.1c). Acoustic measurements are made at 250 Hz and transmitted in near-real time to the International Data Centre (IDC) in Vienna for routine processing and analyst review (Hanson et al., 2001).

We note that arrivals from Monowai show lower phase coherency at the northern array and appear attenuated by 4-8 dB compared to H03S. This may be due to bathymetric blockage and scattering of the incoming signal by one or more unnamed seamounts west of Isla Robinson Crusoe, where the seafloor shoals to depths of less than 150 m. As the east-west-trending archipelago effectively dissects the field of view of the two triplets, activity at Monowai cannot be reliably tracked at H03N by the methods outlined here. Hence, we limit our study to the southern array.

3.2.2 Direction-of-arrival calculations and detection

Hydrophone recordings are corrected for instrument response and the mean and trend is removed. Data is band-pass filtered between 4 and 12 Hz using a standard two-pole Butterworth filter. The cutoffs correspond to the frequencies at which long-range signals are detected most efficiently by IMS-type hydrophone arrays (Hanson and Bowman, 2006) and account for potential noise contamination from both ends of the spectrum, i.e. ocean microseism, marine mammal vocalization, and commercial shipping (e.g., Chapman and Price, 2011). As instruments are moored at similar water depths and potential sources are located in the acoustic far field, direction-of-arrival calculations follow a two-dimensional plane-wave fitting approach (Del Pezzo and Giudicepietro, 2002). Hydroacoustic recordings are subdivided into 1-min long, non-overlapping windows. Peak delay times t_{ij} between instrument pairs located at relative positions x_{ij} are derived from normalized cross-correlation of the windowed data. Subsequently, the slowness vector $p \equiv (p_x, p_y)$ of a planar wave front moving across the triplet array can be obtained by solving the following equation in a least-square sense:

$$t_{ij} = p \cdot \Delta x_{ij} \tag{3.1}$$

Apparent sound speed v across the array and angle of arrival θ, which represents the geodesic back azimuth between receiver and source along a great-circle path, are derived from

$$v = \left({p_x}^2 + {p_y}^2\right)^{-1/2} \tag{3.2}$$

and

$$\theta = tan^{-1}\left(\frac{p_x}{p_y}\right). \tag{3.3}$$

Absolute errors for values calculated in (3.2) and (3.3) are obtained from the covariance matrix of the data and subsequent propagation of two sigma standard

errors. Following a similar approach by Bohnenstiehl et al. (2013), peak delay times t_{ij}, t_{jk}, and t_{ki} between the three hydrophone pairs are summed to derive the closure function cl of the windowed cross-correlation. cl is assumed to approach zero for well-correlated signals and provides an additional quality constraint for filtering acoustic arrivals alongside the mean cross-correlation coefficient cc between the three hydrophone pairs (cf. Cansi, 1995):

$$cl = t_{ij} + t_{jk} + t_{ki} \tag{3.4}$$

A number of detection criteria are put in place to separate coherent acoustic phases from ambient noise. In order to eliminate arrivals not traveling in the SOFAR channel, signals not arriving within ± 50 m/s of 1481 m/s in a 1-min window are omitted from the data set, with 1481 m/s being the mean annual sound speed of the sound channel axis at Juan Fernández, estimated from data provided by the 2005 World Ocean Atlas (Appended Figure A.1). The minimum mean correlation coefficient between the hydrophone pairs is set to 0.3, which is consistent with empirically derived thresholds used by Nichols and Bradley (2016) and Li (2010) for IMS-type arrays of the same aperture and roughly corresponds to the noise floor for 1-min windows in the 4-12 Hz band (Metz et al., 2016). Following Graeber and Piserchia (2004) and Bohnenstiehl et al. (2014), the detection threshold of the closure function is set to |48| ms, corresponding to a maximum mismatch of 12 sampling intervals at 250 Hz.

3.2.3 Uncertainty analysis

We investigate the accuracy of returned back azimuth and sound speed values using air gun shots produced during the 2017 CEVICHE seismic reflection experiment during cruise MGL1701 of R/V Marcus G. Langseth (Rolling Deck to Repository Program, 2017). In January 2017, a seismic survey was carried out along the continental margin

off-coast south central Chile and in the field of view of the H03S hydrophone array (Figure 3.2). As acoustic coupling into the deep sound channel is a function of seafloor slope, aspect, and depth near the signal source (Blackman et al., 2004; Bohnenstiehl et al., 2012), calibration data is limited to a subset of shots generated between 23:00 UTC 19 January and 05:00 UTC 21 January 2017 during survey line MC08R. During this time, the vessel passed through an area close to the continental shelf, where the seafloor topography is expected to be relatively even and the measured water depth varied by less than 200 m, thus enabling the constant deployment of homogeneous calibration shots at a source-receiver distance of 567 $\pm$ 7 km. As the incoming signal arrives at H03S from a southeastern direction, potential blockage due to the protruding bathymetry of the eastern Juan Fernández archipelago is avoided.

Applying the previously defined detection thresholds for sound speed, correlation coefficient, and closure function, a total of 1689 1-min detections are made at the H03S array. As the vessel moves along the survey line at a southwestern heading, back azimuths and sound speed distinctly stabilize between 109 and 129° and near 1480 m/s, respectively (Figure 3.2a-b). A comparison of the derived and the geodesic angles of arrival shows that detections are accurate to within 0.2° and 0.4° at one and two standard deviation uncertainty (Figure 3.2c). We also observe a systematic error of -1.3 $\pm$ 0.2°, which corresponds to an offset of 5-10 km abaft the vessel and, following Bohnenstiehl et al. (2012), suggests that coupling into the deep sound channel may take place in the form of bottom-up reflection of acoustic energy at the seafloor. Derived sound speed values average at 1474 m/s and are well within two standard deviations ($\pm$ 14 m/s) of the nominal estimate of 1481 m/s (Figure 3.2d). The offset could be explained by the movement of the hydrophone moorings due to deep ocean currents as well as local variations in ocean temperature, and hence, apparent sound speed across the array (e.g., Evers and Snellen, 2015).

As acoustic recordings are binned to discrete intervals, individual shots are not

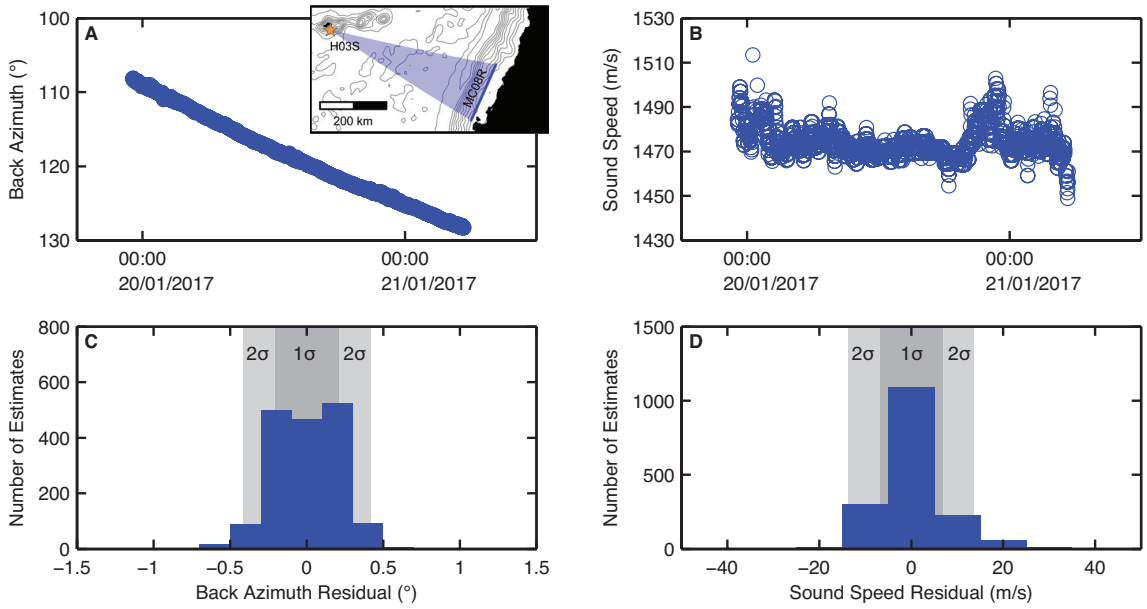

Figure 3.2: Uncertainty analysis of back azimuths calculated from H03S hydrophone triplet data. (a-b) Back azimuth and sound speed of 1689 1-min detections (blue circles) of 4013 air gun shots generated along a seismic reflection profile of the CE-VICHE experiment between 23:00 UTC 19 and 05:00 UTC 21 January 2017. The inset shows the location of the seismic sources along profile MC08R between 109 and 130° back azimuth (dark blue line and shaded area), as seen from the southern H03 array (orange star). The survey is carried out at a southwestern heading and at an average distance of 567 ± 7 km from H03S, with start and end coordinates of the included shots at 35.36°S, 73.00°W and 37.07°S, 73.77°W. Grey bathymetric contour lines are spaced at 500 m intervals. (c) Distribution of residuals between observed and geodesic back azimuth of the detections shown in Figure 3.2a. Dark and light grey shaded areas mark one and two sigma standard deviations at 0.2 and 0.4°, respectively. A systematic error of -1.3 ± 0.2° is omitted for clarity. (d) Distribution of residuals between observed and nominal sound speed across the array. The detections shown in Figure 3.2b average at 1474 ± 7 m/s, at an offset of 7 m/s from the value indicated by the 2005 World Ocean Atlas (1481 m/s). One and two standard deviation uncertainties are at 7 and 14 m/s respectively.

identified. However, an estimate of data completeness can be made using the proportion of 1-min detections: Over a 30-hour period 4013 shots were deployed. Dividing this total by the average number of shots per minute (2.25) results in 1784 possible 1-min detections at H03S during the survey time. As 1689 1-min detections were made, we conclude that completeness is at least 95% within the defined detection thresholds. We also note that this proportion is not improved significantly by lowering one or all detection thresholds, which indicates that missing shots may have been misfired or blocked prior to their arrival at the H03S array, such that data completeness may in fact be even higher.

Excluding the systematic error, our calculations show that acoustic sources can be identified accurately to within 0.4° and 14 m/s (two sigma standard deviation) by the defined detection parameters. Measured uncertainties associated with derived back azimuths and slowness are consistent with values reported for IMS-type hydrophone deployments of the same configuration (Graeber and Piserchia, 2004; Hanson and Bowman, 2006).

3.3 Tracking volcanic activity at Monowai

3.3.1 Density-based clustering

Previous observations of distinct bursts of T phases, recorded by regional seismic stations, suggest that volcanic activity at Monowai typically occurs in episodes of hours to a few days in length (e.g., Chadwick et al., 2008b). In order to identify such discrete times of unrest in our data set, we exploit the fixed geometrical relationship between Monowai and the IMS hydrophone station. As arrivals associated with activity at the volcano move across the array and detection thresholds are applied, coherent phases stabilize along a distinct back azimuth over a short period of time, indicating a stationary, quasi-continuous source (Figure 3.3). A density-based spatial clustering

algorithm, DBSCAN (Ester et al., 1996)[1], can then be implemented to identify such densely-packed groups of detections, and hence detect and track episodes of volcanic activity in the data set.

DBSCAN is based on the calculation of nearest neighbor distances and requires two input parameters: a minimum number of points m to form a cluster, and a search radius ϵ in the parameter space. The clustering process considers time and back azimuth of 1-min detections in a Cartesian plane and can be abstracted as follows: Data points with at least m points within a radius of ϵ are core points, which may either form a new cluster, or be assigned to a preexisting one if a core point already exists within ϵ distance. Data points reachable from a core point, but with less than m points in their ϵ neighborhood, are assigned to the cluster of the core point. All other data points are classified as noise. For this study, the minimum number of points m, i.e. 1-min detections, is set to 60, which corresponds to the shortest period of activity previously observed at Monowai, i.e. an hour-long eruptive collapse event in May 2002 (Wright et al., 2008). We define the search radius ϵ as 12 hours along the x-axis and 0.5° along the y-axis, which reflects the estimated accuracy of the plane wave fitting routine and is twice the duration of the longest known intra-eruptive pause in activity at the volcano (Metz et al., 2016). As DBSCAN is computationally expensive and low-frequency arrivals from Monowai are not expected to vary by more than a few degrees (Bohnenstiehl et al., 2014), the spatial domain of the data set is limited to a ten degree range centered around the geodesic back azimuth to Monowai ($243.8 \pm 5°$).

Given the above parameter settings, the shortest possible cluster identifiable by the DBSCAN algorithm would span 60 consecutive 1-min detections between 238.8 and 248.8° over the course of one hour along a constant back azimuth. Vice versa, the shortest, least dense cluster would hold 60 1-min detections along a constant back

[1]The relevant code, as implemented by the Yarpiz Project, was obtained from the MathWorks FileExchange under 'DBSCAN Clustering Algorithm'.

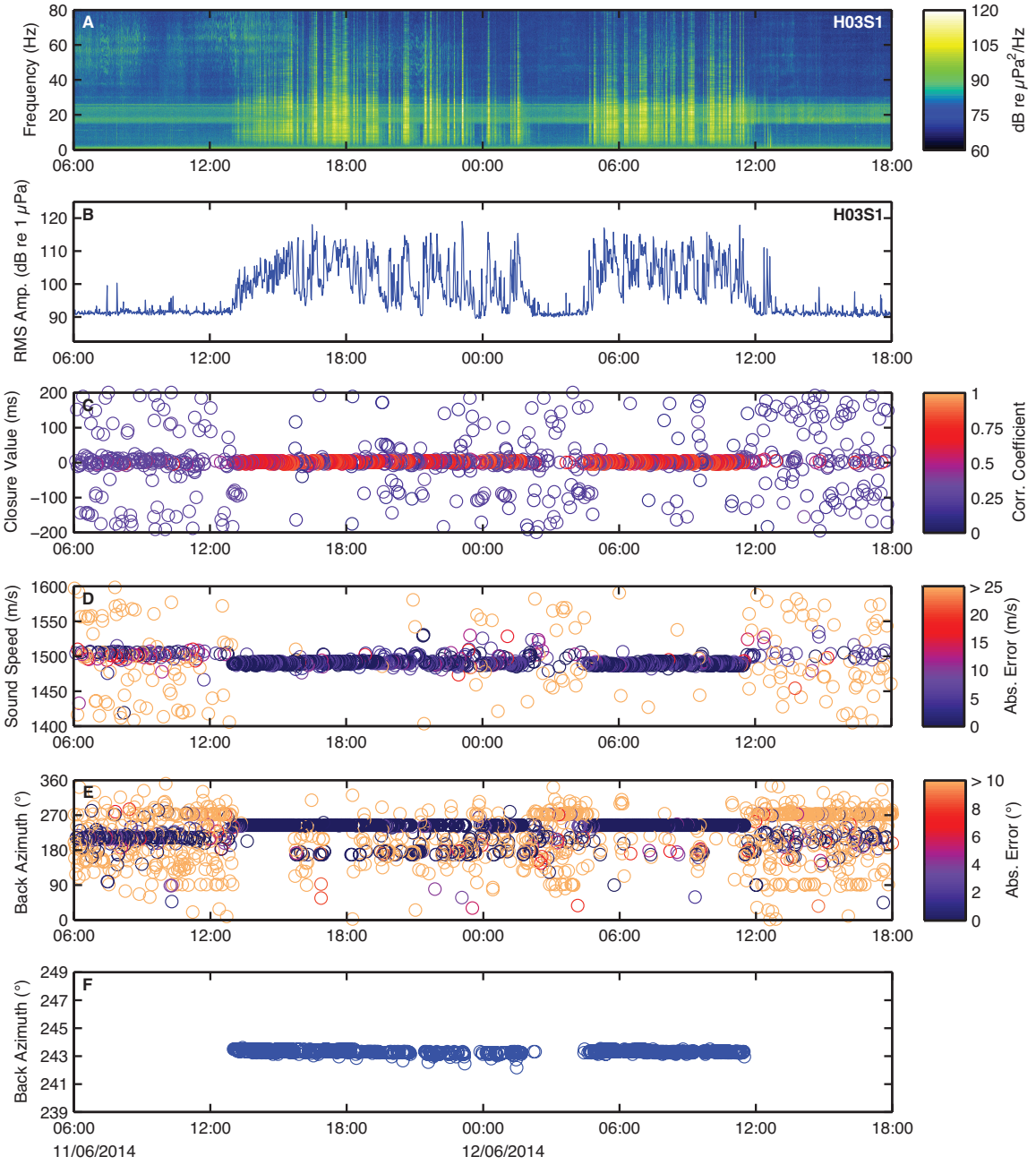

Figure 3.3: See next page for caption.

Figure 3.3: 36 hours of hydroacoustic data recorded at station H03S, beginning at 06:00 UTC 11 June 2014. Appended Figure A.2 shows the corresponding 36 hours of data recorded at the northern triplet array. (a) Single-receiver spectrogram of the H03S1 hydrophone data. A 2 Hz high-pass filter is applied to minimize background noise; however, wide-band contamination is present between 18 and 26 Hz, most likely due to whale calls. Note that the high-pass filter of 2 Hz, chosen to visualize the full dynamic range of the hydrophone recordings, differs from the 4-12 Hz processing band.(b) Root-mean-square (RMS) amplitudes calculated over 1-min windows in the 4-12 Hz band. Processing parameters and results of the plane wave fitting routine are shown in the form of (c) closure function of summed lag times and mean correlation coefficient between hydrophone pairs, (d) apparent sound speed across the array, and (e) back azimuth. Arrivals from Monowai are recognizable in all subfigures: Hydroacoustic phases, most distinguishable between 2 and 20 Hz, arrive from 13:00 UTC onward, accompanied by a positive shift in RMS amplitude of up to 25 dB re 1 μPa above the noise floor. Coherent phases clearly stabilize at a sound speed of 1480-1485 m/s and back azimuth of $\sim$243.4°, indicating a continuous signal that travels in the deep sound channel and that is within 0.4° of the geodesic angle of arrival for a source at the volcano (243.8°). (f) shows 1-min detections after filtering the data using the previously defined thresholds of $cc > 0.3$, $cl < 48$ ms, and a sound speed range of 1431-1531 m/s.

azimuth and be registered at over twice the length of the search radius, i.e. 24 hours. However, Figure 3.4a shows that due to the episodic nature of activity at Monowai (Chadwick et al., 2008b) and the low number of detections arriving from a similar direction, clustering results are extremely robust: Typically, hundreds to thousands of detections are made over short time scales and from similar azimuth, which reduces the effect of the initial parameter setting. For example, relaxing m to 120 and ϵ to 1° and 24h, respectively, for the data shown in Figure 3.4a, results in the same number of clusters, with more than 99% of identical detections made.

3.3.2 Comparison of hydroacoustic and seismic recordings

Due to the large source-receiver distance between the volcano and the hydrophone array, some uncertainty exists as to whether clusters formed by the DBSCAN algorithm truly represent activity at Monowai, or relate to other sources along the same great circle path, for example swarms of tectonic earthquakes along the Chile and

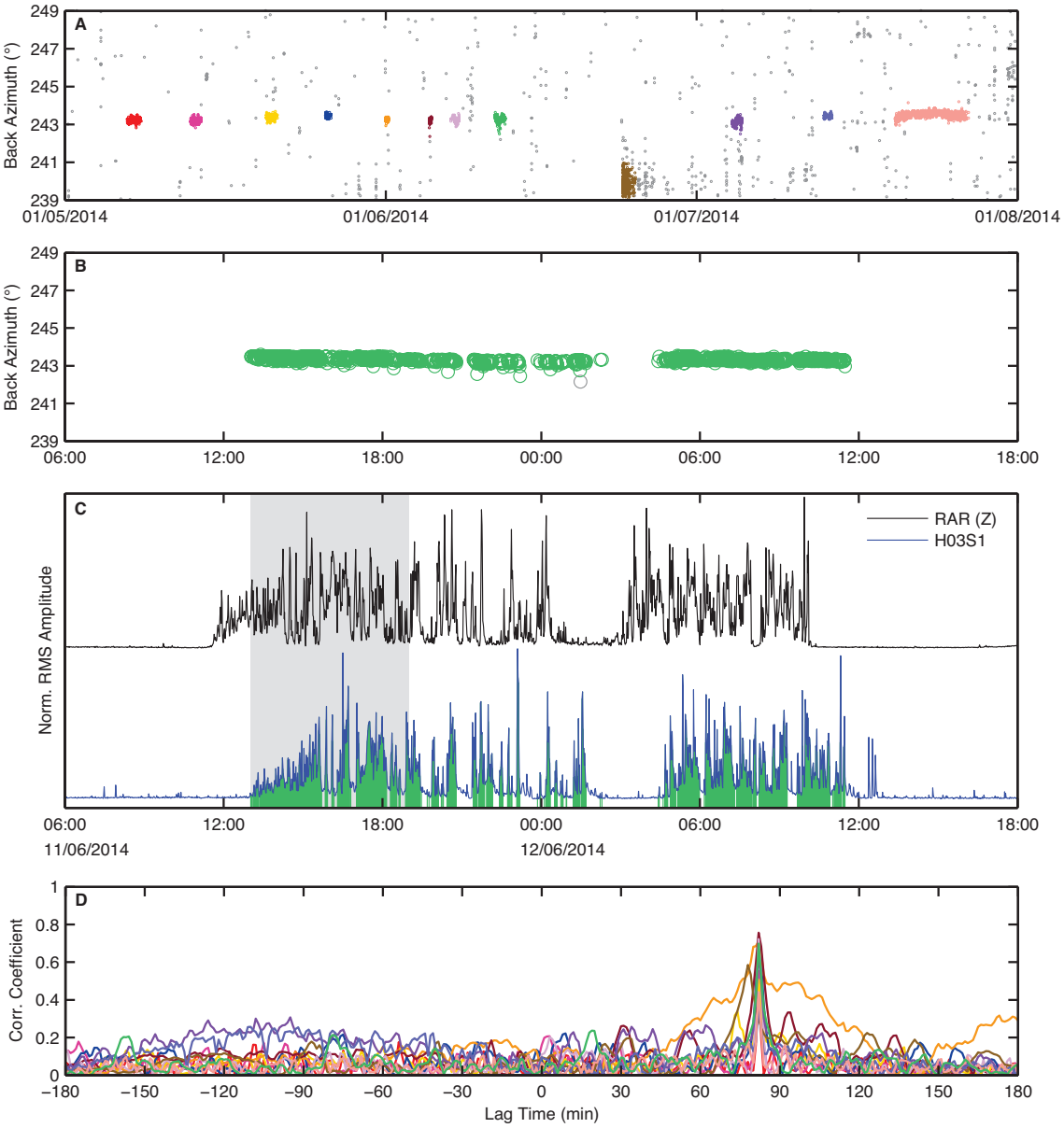

Figure 3.4: See next page for caption.

Figure 3.4: Density-based clustering and signal cross-correlation. (a) Results of the DBSCAN algorithm for a three-month period, beginning at 00:00 UTC 1 May 2014. Colored circles mark 1-min detections assigned to a cluster by the DBSCAN algorithm, using a minimum number of $m = 60$ and a search radius ϵ of 0.5° on the y-axis and 12h on the x-axis. Grey circles are noise. (b) Back azimuths of clustered detections between 06:00 UTC 11 June 2014 and 18:00 UTC 12 June 2014. Data corresponds to the green cluster in Figure 3.4a and the volcanic episode shown in Figure 3.3. (c) Normalized RMS amplitudes at the RAR broadband station (vertical component) and the H03S1 hydrophone, calculated over 1-min windows. The data are band-pass filtered at 2-6 Hz and 4-12 Hz, respectively. Green stems correspond to 1-min detections associated with the cluster shown in Figure 3.4b. The grey shaded area represents the six-hour period with the highest density of detections and delimits the segments of the RMS envelopes used in the cross-correlation. (d) Cross-correlation results of clusters shown in Figure 3.4a (matching colors). The distinct peaks of the correlation coefficients indicate lag times of 82 min, suggesting that the signals arrive 1 h and 22 min earlier at the Rarotonga seismometer relative to the H03S1 hydrophone at Juan Fernández Islands, which matches a source location at Monowai. The brown cluster corresponds to a shallow (< 20 km hypocenter depth) 6.9 m_b magnitude earthquake, and its subsequent aftershock sequence, that occurred on 23 June 2014 at 30.0°S, 177.53°W in the central Kermadec Arc, which is in agreement with the peak delay time of 78 min. Since the cluster fails to match the designated lag of 82 min, it is not added to the long-term record of volcanic episodes at Monowai.

East Pacific Rise. However, direct relocation of T phase arrivals is not always possible, as seismic recordings at PPTF and TAOE station suffer from high ambient noise levels above 2 Hz. Instead, we resort to relative travel time differences between the broadband seismometer at Rarotonga and a single element of the H03S array as a measure to unambiguously identify Monowai as the signal source (Metz et al., 2016).

For the time span of each cluster, envelope functions are calculated from normalized 1-min RMS amplitudes for the vertical component of the seismic station and hydrophone H03S1 (Figure 3.4b-c). In the case of Figure 3.4c, the two signals appear visually coherent, and cross-correlating their envelopes reveals a high degree of correlation at a peak delay time of 82 min (green line in Figure 3.4d). This is in agreement with the nominal arrival time offset between RAR and H03S1, which is estimated at 82 min 24 $\pm$ 14 sec (cf. Appended Figure A.3), assuming a source at Monowai and an average propagation speed of 1480 $\pm$ 5 m/s along the SOFAR channel axis (Munk and Forbes, 1989, see Figure 3.1a for source-receiver paths). We account for possible noise contamination of the derived envelopes, for example due to nearby ship traffic, seismic surveying, and earthquakes along the Tonga-Kermadec Arc or the Chilean subduction zone, by limiting the cross-correlation to the 6-hour segment of a cluster during which the highest number of 1-min detections are made. If the maximum correlation coefficient peaks at the designated delay time of 82 min, the cluster is added to the long-term record of activity at Monowai. This validation process is repeated for all clusters formed by the DBSCAN algorithm.

3.4 Results

3.4.1 Volcanic activity at Monowai, 2003-2004 and 2014-2017

Following the approach outlined in the previous sections, a total of 82 clusters, consisting of 196,949 1-min detections over the course of 3.5 years, were identified and

tracked back to Monowai, thus providing discrete times of activity at the volcano in the record of the H03S array between July 2003 and March 2004, and from April 2014 to January 2017 (Figure 3.5a-b). Remarkably, more than 98% of all detections within the processing window of 243.8 ± 5° are associated with activity at Monowai, suggesting that the volcano is the predominant source of low-frequency sound in the central Tonga-Kermadec Arc region.

Individual volcanic episodes last from a few hours to a maximum of 14 days and typically occur days to weeks apart, yet rarely exceeding more than one month of acoustic quiescence. Arrival rates can exceed 1320 1-min detections (i.e. a cumulative sum of 22 hours) per day and average at 725 across all episodes, indicating that, overall, acoustic phases from Monowai are registered every two minutes at the hydrophone array during times of volcanic activity (Figure 3.5c-d). Notably, the longest pause in activity follows an intense series of four episodes in October and November 2014 that account for more than 20% of all registered detections and sustain some of the highest arrival rates in the data set (Figure 3.5e-f). Eruptive activity at Monowai during this time had also been noticed in the form of pumice rafts near the location of the volcano in late October 2014 (Global Volcanism Program, 2017a), which confirms our hydroacoustic observations and the results of the clustering algorithm. On a second occasion (Global Volcanism Program, 2017a), reports of discolored surface water near Monowai coincide to the day with a cluster of detections in May 2016.

Mean RMS amplitudes per episode range from 88 dB to 110 dB re 1 μPa in the 4-12 Hz band, thus exceeding background noise levels ($\sim$90 dB re 1 μPa, cf. Figure 3.3b) by up to 20 dB (Figure 3.5g-h). We observe peak values of up to 128 dB for individual detections, which is on the same order as long-range acoustic measurements of the May 2011 eruption (Metz et al., 2016). Although a detailed analysis of the frequency domain is beyond the scope of this study, we find a distinct absence of narrowband, harmonic tremor throughout the data set, which is different from other

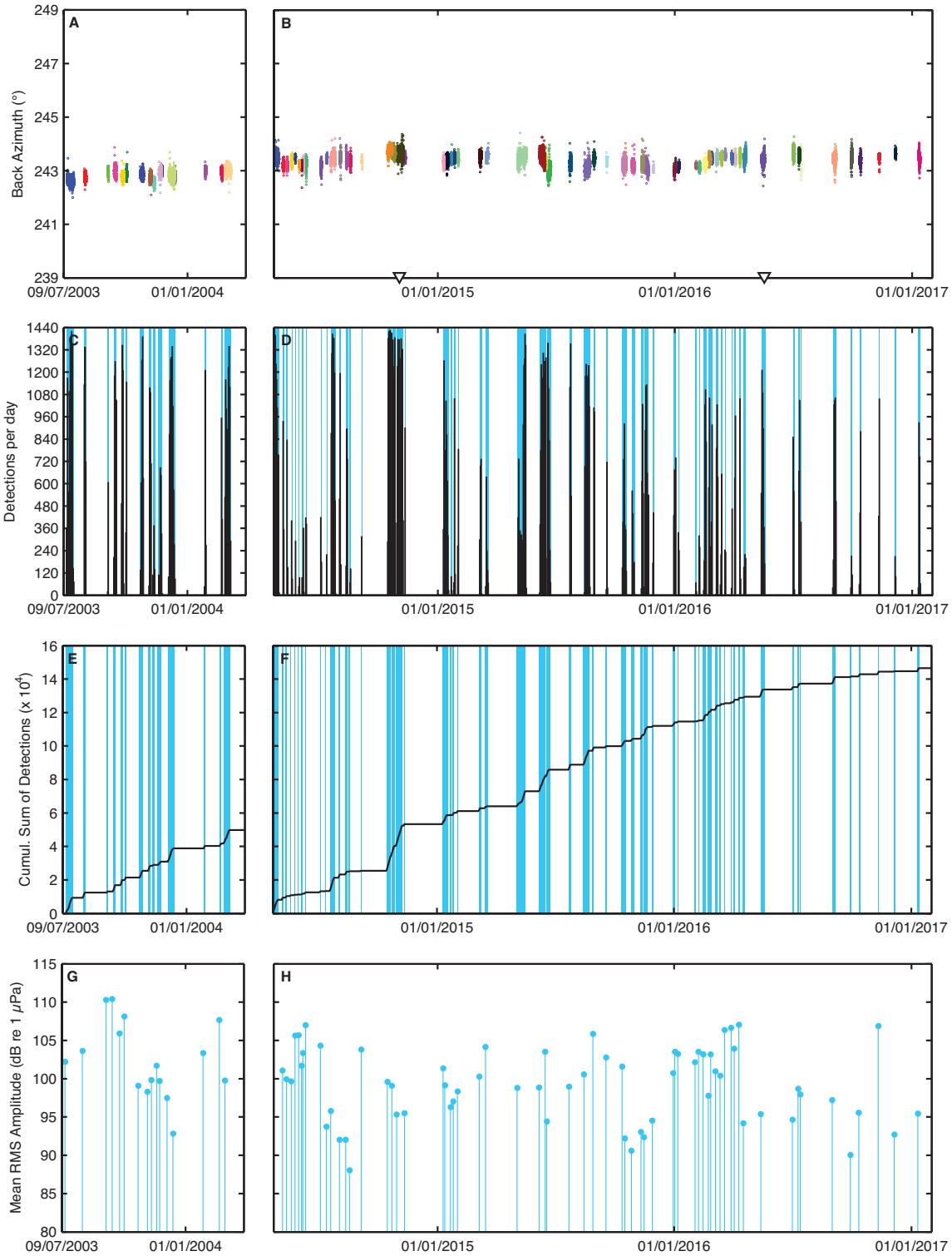

Figure 3.5: See next page for caption.

Figure 3.5: Record of volcanic activity at Monowai, 10 July 2003 to 25 March 2004 (left column), and 23 April 2014 to 31 January 2017 (right column). (a-b) Clustering results of hydroacoustic detections at H03S arriving from within 5° of the geodesic back azimuth to Monowai, i.e. from 238.8° to 248.8°. 82 clusters (different colors) were identified in the record, comprising a total of 196,949 1-min detections. Note that derived back azimuths vary slightly between the 2003-04 and 2014-17 period due to the different positions of H03S hydrophone elements before and after their reinstallation in 2014. White triangles mark observations of floating debris and discolored water on 31 October 2014 and 19 May 2016, respectively (Global Volcanism Program, 2017a). (c-d) Number of 1-min detections per calendar day. Blue shaded areas correspond to clusters shown in Figure 3.5a-b. (e-f) Cumulative sum of detections, calculated separately for both periods. 49,838 detections are made from July 2003 to March 2004, and 147,111 between April 2014 and January 2017. (g-h) Mean RMS amplitudes of the identified clusters, calculated from 1-min windows in the 4-12 Hz band.

active sites in the Tonga-Kermadec Arc, e.g. Brothers or West Mata (Dziak et al., 2008; Bohnenstiehl et al., 2014). Instead, activity at Monowai consists of coherent, seconds to minute-long arrivals in the 4-20 Hz band, with occasional broadband bursts of up to 80 Hz and more, most likely representing an ensemble of signals generated by different processes, including volcano-tectonic earthquakes, fluid-driven oscillation, brittle fracturing, explosive fragmentation, and mass wasting events at the seafloor-ocean interface (Caplan-Auerbach et al., 2017, see also Figure 3.3a).

We further investigate whether activity at Monowai differs between the two subsets of volcanic episodes in 2003-04 and 2014-17. Results from a two-sample Kolmogorov-Smirnov-Test (Massey, 1951) suggest that clustered detections from the two periods come from the same continuous distribution (5% significance level), indicating no significant change in the style of activity within the means of the tested statistical parameters, i.e. mean RMS acoustic magnitude in the 4-12 Hz band, episode duration, inter-episode time, and number of detections per day. We attribute the offset between mean back azimuths of volcanic episodes, averaging at 242.8 ± 0.3 and 243.4 ± 0.3° (two sigma standard deviation) for the 2003-04 and 2014-17 period, respectively, to the repositioning of the hydrophone sensors during the 2014 reinstallation of the H03

station. The systematic, counterclockwise deviation of 0.4 to 1° from the geodesic angle of arrival (243.8°) probably reflects a cumulative effect of uncertainty in sensor positioning (Nichols and Bradley, 2016), array geometry, and right-lateral refraction of the acoustic signal along its great circle path following horizontal temperature gradients in the southern Pacific Ocean as well as between the hydrophone elements (de Groot-Hedlin et al., 2009; Evers et al., 2017). Our estimates are in agreement with Evers et al. (2013) and Green et al. (2013), who estimate the error inherent to IMS-type triplet deployments at $\geq 0.4°$.

In addition to volcanic episodes that can be traced back to Monowai, the DBSCAN algorithm identified a small number of other sources along the Tonga-Kermadec Arc. These clusters are usually associated with shallow (< 30 km focal depth), large magnitude tectonic earthquakes at locations distant from the volcano, and therefore produce different lag times during the cross-correlation procedure. For example, Figure 3.4 shows clustered 1-min detections of a catalogued 6.9 m_b event on 23 June 2014 in the central Kermadec Arc (IRIS ID No. 4722859). The event produced numerous aftershocks in the range of 4.9 to 6.3 m_b over the following five days, thus explaining its detection by the clustering algorithm. In two cases, clusters neither match the back azimuth and delay time for a source at Monowai, nor the location and timing of a known seismic event. These arrivals may be linked to volcanic activity at other locations in the Tonga-Kermadec Arc and are discussed in subsection 4.4 in more detail.

3.4.2 Relation to previous studies of T phase seismicity at Monowai

In a previous study, Chadwick et al. (2008b) investigated volcanic activity at Monowai between 1998 and 2007 from T phases recorded at TVO station, a broadband seismometer that is located at Taravao, Tahiti-Iti (Figure 3.1a), as part of the Polynesian

Seismic Network (RSP, Talandier and Kuster, 1976). Although the T phase dataset overlaps with the 2003-2004 period of this study, comparison of the two records is not straightforward: Hydrophone data is binned to 1-min intervals and detection is based on signal coherence, whereas registered T phases represent discrete events defined by short-term/long-term filtering of energy ratios, and analyst review. Therefore, we focus here on timing and relative distribution rather than the absolute number of arrivals from the volcano.

Between July 2003 and March 2004, a total of 869 T phases were detected at the TVO seismometer and traced back to Monowai using further RSP stations for source location (Chadwick et al., 2008b). We find that 854 of these events, a relative share of 98.3%, fall within the bounds of one of the 16 episodes identified by density-based clustering of 49,838 hydroacoustic detections of the same time period (Figure 3.6). In all cases, 1-min detections precede the onset of T phase events registered at TVO by hours to days. For example, during the 8.5-days-long episode in February 2004, the first T phase event is registered more than five days after the first hydroacoustic arrival. During the same episode, T phase activity at TVO also ceases 18 hours prior to the last 1-min detection. On average, hydroacoustic detections are made 27 hours earlier, and outlast registered T phase events by 15 hours across all clusters of the 2003-2004 period. Furthermore, no T phases were observed during the episodes in mid-November and mid-December 2003, both of which are within the bottom quarter of derived mean RMS acoustic magnitudes (98 and 92 dB re 1 μPa respectively, cf. Figure 3.5g).

Although differences in the timing of individual episodes exist, Figure 3.6 shows an excellent correlation (coefficient 0.98) between the normalized cumulative number of hydroacoustic detections at H03S and T phase events registered at the TVO station, indicating high similarity between the two time series. From this, we conclude that a) the relative distribution of arrivals is comparable between both datasets, confirming

results from density-based clustering, and b) volcanism at Monowai indeed occurs in discrete episodes, with little to no activity observed in between. We further note that the ratio of hydroacoustic arrivals to T phases varies between a factor of 18 to 800 across all episodes. This disparity cannot be explained solely by differences in data segmentation, but is most likely due to a combined effect of signal attenuation during the ocean-land conversion process, high noise levels at the seismometer that inhibit the detection of weaker events, and bias introduced by the parameter setting for declaring a T phase event in the seismic record of the TVO station. Thus, our findings illustrate the advantage of the acoustically quiet hydrophone array over the land-based seismometer in detecting volcanic activity at Monowai, despite being located 6200 km further away from the source.

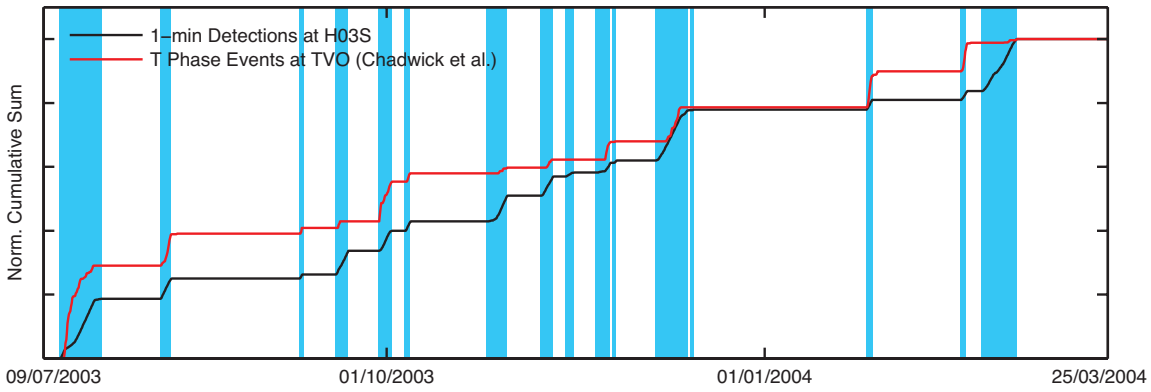

Figure 3.6: Comparison of the normalized cumulative number of 1-min detections at the southern H03 array (black line) with T phase events registered at TVO station of the Polynesian Seismic Network (red line) between July 2003 and March 2004 (Chadwick et al., 2008b). 854 of the 869 T phase events fall within the bounds of one of the 16 episodes of activity as defined by this study (blue shaded areas, see also Figure 3.5e). The black and red lines are highly similar at a cross-correlation coefficient of 0.98.

3.4.3 Resolution and seismic magnitude estimation

RMS amplitudes of 1-min detections associated with volcanic activity at Monowai follow a right-skewed normal distribution (Figure 3.7a), indicating that only events

above a certain threshold are fully detected at the H03S array. In an attempt analogous to the derivation of the magnitude of completeness in seismic catalogues, we calculate the acoustic resolution of the data set according to the maximum curvature method by Wiemer and Wyss (2000). Here, the amplitude level above that all arrivals can be successfully identified is defined as the data bin with the highest number of detections and roughly corresponds to the maximum value of the first derivative of the cumulative distribution shown Figure 3.7b (Woessner and Wiemer, 2005), i.e. 97 dB re 1 μPa. We interpret the relatively gradual drop-off of detections below this threshold as a combined effect of data segmentation, which can lead to the splitting of arrivals across two or more 1-min windows, and low-level variations in background noise, for example due to ice-generated tremor at southern latitudes (cf. Talandier et al., 2006), earthquake swarms, and commercial shipping (Sirovic et al., 2013). It is therefore reasonable to assume that activity at Monowai extends to levels beyond the detection threshold of the H03S array, and may occur even more frequently than constrained by our approach.

In a further step, hydrophone and seismometer recordings of tectonic earthquakes catalogued by the global IMS network are compared to estimate seismic magnitudes of activity at Monowai (Figure 3.7c). We account for attenuation of the signal in the solid earth and along the deep sound channel by constraining earthquake data to events with a catalogued depth of less than 80 km and a source-receiver distance similar to the geodesic path between the volcano and the H03S array, i.e. 8900 to 9200 km. Since Monowai itself is located within an aseismic 'gap' near the intersection of the Tonga-Kermadec Arc with the Louisville Ridge (Wyss et al., 1984; Bassett and Watts, 2015), only 28 earthquakes, scattered between 25 and 30°S along the northern Kermadec Arc to the south of the 'gap' (see inset of Figure 3.7c), fulfill the above criteria and were registered by the H03S1 hydrophone (Appended Table A.2). At an average arrival length of 63 seconds and typically band-pass filtered between 4 and 12

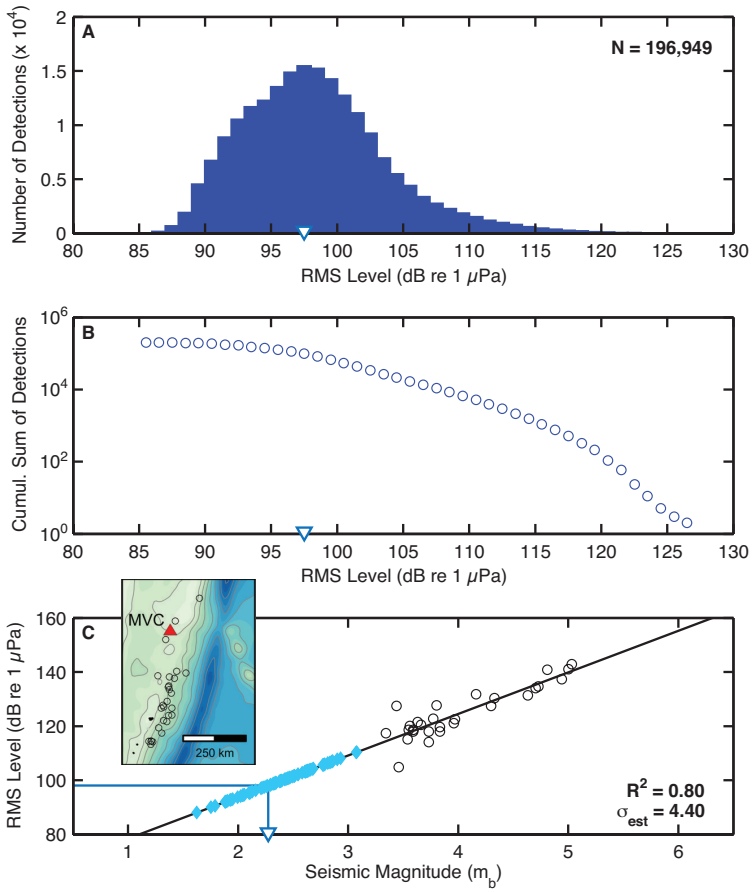

Figure 3.7: Resolution and seismic magnitude. (a) RMS amplitude distribution of all 196,949 1-min detections recorded at IMS hydrophone H03S1 binned to 1 dB intervals. The blue and white filled triangle marks the level of acoustic resolution at 97 dB re 1 μPa, calculated according to Wiemer and Wyss (2000). (b) Cumulative frequency-magnitude distribution of 1-min detections shown in Figure 3.7a. Note the logarithmic scaling of the y-axis. (c) RMS pressure amplitude of 28 earthquakes (black circles) registered by the IMS seismic network and hydrophone H03S1. Events are located between 25 and 30°S along the Kermadec Arc (see inset), at source-receiver distances of 8950 to 9175 km and focal depths of up to 80 km. The black line marks the least-square fit of the regression, which is significant at $R^2 = 0.80$ and an error of 4.40 dB re 1 μPa. Following the derived trend, acoustic resolution of 97 dB re 1 μPa corresponds to a body wave magnitude of 2.2 m_b at Monowai (blue line and triangle). Mean RMS amplitudes of the 82 episodes range from 88 to 110 dB re 1 μPa (light blue diamonds), suggesting comparable mean magnitudes between 1.6 and 3.1 m_b. Acoustic amplitudes of individual arrivals translate into a seismic magnitude range of 1.4 to 4.2 m_b, with less than 1000 events greater than 3.5m_b.

Hz, the automated parameter setting of the IMS processing stream closely matches the aggregate approach used in this study.

The equation of the least-square regression line shown in Figure 3.7c,

$$RMS\ Level\ (dB\ re\ 1\ \mu Pa) = 63.1 + 15.4 m_b \tag{3.5}$$

indicates a linear relationship between acoustic and seismic measurements. The derived trend is significant ($R^2 = 0.80$) and in good agreement with observations by Pulli and Upton (2002) for the 2001 M_W 7.7 Bhuj earthquake sequence recorded at IMS hydrophones in the Indian Ocean. Acoustic resolution of 97 dB corresponds to a magnitude of completeness of 2.2 m_b which is an order of magnitude lower than the smallest tectonic event previously detected by IMS seismometers in the central Kermadec Arc region (3.3 m_b). Following this first order approximation, mean magnitudes of volcanic episodes at Monowai range from 1.6 (88 dB) to 3.1 m_b (110 dB) and are consistent with presumed levels of activity at the volcano during its 2011 eruption ($\sim$2 m_b, Metz et al., 2016). Since only a small number of individual arrivals reach peak amplitudes greater than 120 dB ($>$ 3.5 m_b), overall levels of activity at the volcano most likely are too low to be resolved by a sparse network of land-based seismometers over teleseismic distances.

3.4.4 Further observations of volcanic activity in the Tonga-Kermadec Arc

As described in section 4.1, two of the clusters formed by the DBSCAN algorithm could not be linked to activity at Monowai or known seismic events along either the Tonga-Kermadec Arc or the East Pacific Rise, and therefore are investigated further.

The first cluster consists of 525 1-min detections received at the H03S array over the course of five days in December 2014. Acoustic phases arrive from a mean back

azimuth of 246.4°, thus corresponding to a location in the southern Tonga Arc, approximately 400 km north of Monowai (Figure 3.8a-b). The activity is best described as a suite of short (< 5 sec), transient arrivals at frequencies below 16 Hz, rarely exceeding background noise levels by more than 10 dB in the 4-12 Hz processing band (Figure 3.8c-d). Known volcanically active sites in the area include Volcano 14, where hydrothermal venting was observed by Stoffers et al. (2006) during expedition SO167 aboard R/V SONNE, as well as a shallow seamount at 22.9°S, 176.4°W, also

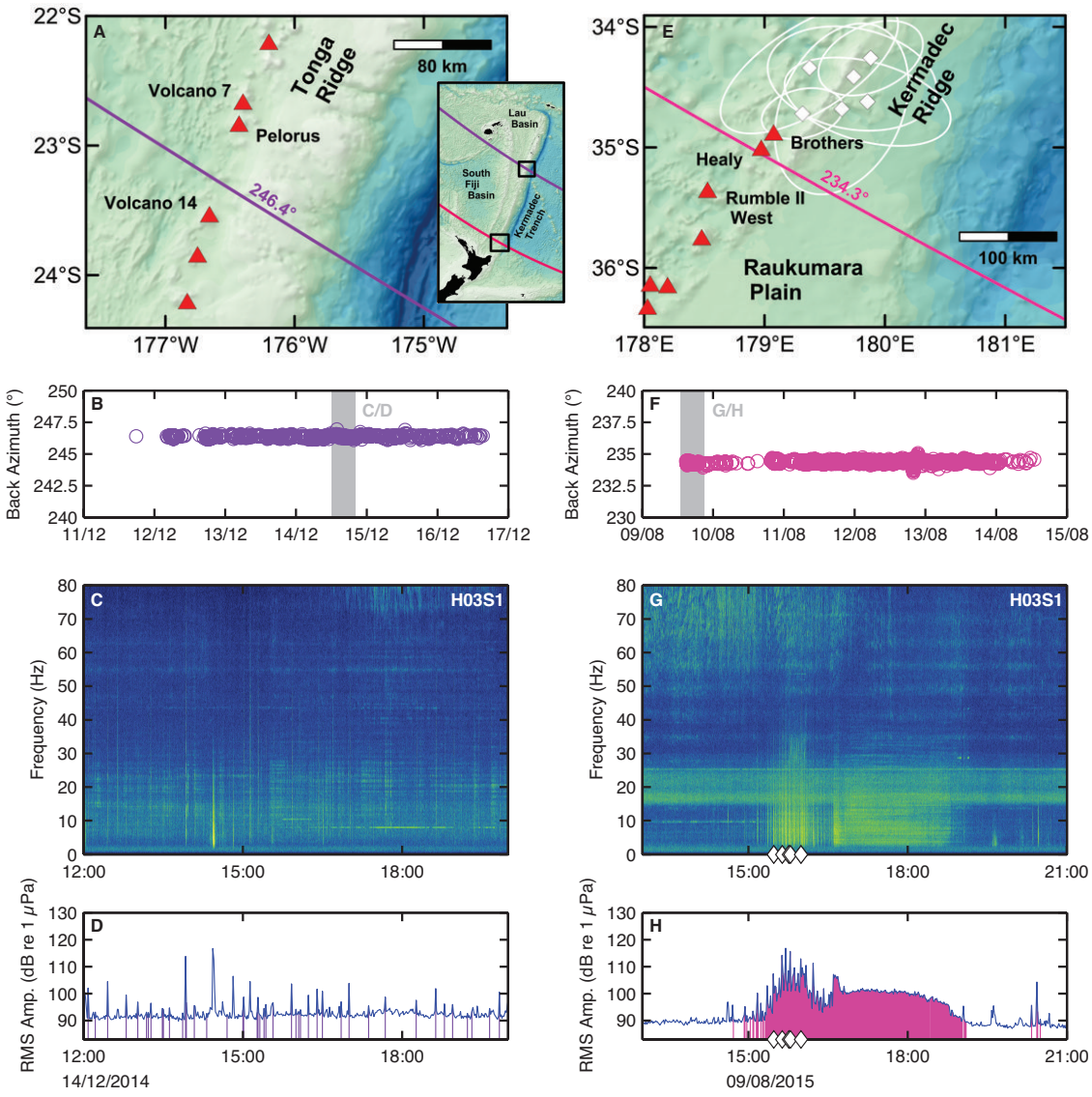

Figure 3.8: See next page for caption.

Figure 3.8: Observations of two presumed episodes of volcanic activity in the Tonga-Kermadec Arc. Note that in accordance with their appearance in the text, subfigures follow a column-wise order, but are captioned row by row. (Row 1: a,e) Back projection of mean azimuths (colored lines) of clustered 1-min detections across the southern Tonga and Kermadec Arc (see inset of Subfigure 3.8a for map locations). White diamonds in Subfigure 3.8e mark the epicenters and respective error ellipses of six seismic events registered by the IMS network northeast of the Healy and Brothers domain at the beginning of the cluster. (Row 2: b,f) Back azimuths of detections over the course of the two episodes. Grey shaded areas mark the positions of the spectrogram and RMS data shown in the following subfigures. (Row 3: c,g) 8-Hours single receiver spectrograms of hydrophone data recorded at H03S1, beginning at 12:00 UTC 14 December 2014 and 13:00 UTC 09 August 2015, respectively. In Subfigure 3.8g, background noise due to whale vocalization is present in the 16-26 Hz band, partially overlapping with the acoustic arrivals of earthquakes shown in 3.8e (white diamonds), and the distinct tremor signal between 16:30 and 19:00 UTC. (Row 4: d,h) 1-min RMS amplitudes during the 8-hours time windows. Colored stems indicate times of detections at the H03S array. White diamonds correspond to hydroacoustic arrivals of earthquakes shown in Subfigure 3.8e.

known as Pelorus or Pelorus Reef, that was previously identified as an acoustically and hydrothermally active source by Bohnenstiehl et al. (2014) and Massoth et al. (2007), respectively. Assuming a similar degree of horizontal refraction along the 9290 km long source-receiver path as between Monowai and H03S, i.e. a counterclockwise deviation of about 0.4° from 246.8°, back azimuths fall within 10 km of Pelorus, making it the most likely signal source. However, activity at an uncharted edifice between 23.5°S and Pelorus represents an equally plausible explanation for our observations, as seafloor topography in the area is poorly covered by high-resolution multibeam data and there exists a notable gap in the sequence of otherwise more or less evenly spaced volcanic edifices.

In August 2015, a five-day-long cluster of 2039 detections arrives from 234.3°, which coincides with the geodesic back azimuth to Healy, and is within 0.3° for a source at Brothers volcano in the southern Kermadec Arc (Figure 3.8e-f). At peak times, activity occurs at a rate of up to 500 detections per 12 hours, with broadband, impulsive arrivals in the range of 100 to 120 dB re 1 μPa, lasting between seconds

and tens of seconds (Figure 3.8g-h). In the past, hydrothermal plumes were observed at both sites (de Ronde et al., 2001), and Dziak et al. (2008) report intermittent seismic activity and harmonic tremor at Brothers over the course of several months in 2005. However, it is not possible to attribute acoustic arrivals to either edifice with absolute certainty: The near-perfect match between observed and geodesic back azimuth favors a source at Healy, but considering the same angular offset derived for arrivals from Monowai (0.4°) shifts the back projected path northwards and within 15 km of Brothers volcano.

Interestingly, six earthquakes with epicenters located 50-150 km northeast of Brothers and with magnitudes of between 3.6 and 4.7 m_b were registered by the IMS network prior to the onset of activity and are amongst the first arrivals of the cluster formed by the DBSCAN algorithm. Earthquake arrivals are then followed by a two hours long period of sustained broadband tremor that precedes the beginning of the main burst by approximately 24 hours. Since tremor events can indicate resonance in a fluid-filled chamber or conduit (Chouet, 1996), often preceding or accompanying volcanic eruptions (e.g., McNutt and Nishimura, 2008), we speculate that the 2015 episode at Healy or Brothers volcano may have occurred in response to, or was aided by, dynamic stress changes induced by the nearby earthquake swarm (Walter et al., 2007). Since error ellipses are not well defined in a ridge-parallel direction (cf. Figure 3.8e), one could also assume that the seismic events in fact occurred much closer to, or directly at, one of the volcanoes. In this case, earthquakes could be interpreted as the result of, rather than the cause for, a submarine eruption, signaling, for example, a dyking event or the initial breaching of the magma chamber (Bohnenstiehl et al., 2013). Evidently, these interpretations only represent two of multiple possible scenarios and a more detailed analysis, which is beyond the scope of the study presented here, is needed in the future.

3.5 Discussion

Our observations of activity at Monowai are in good agreement with previous studies (cf. Chadwick et al., 2008b) and suggest that the 82 clusters identified by the DBSCAN algorithm indeed correspond to volcanic episodes. Even though studies of submarine volcanism remain difficult to compare due to the inherent differences of their respective surveying methods, we note that few other known sites, i.e. West Mata in the northern Tonga Arc (Bohnenstiehl et al., 2014) and NW Rota-1 in the Northern Mariana Islands (Chadwick et al., 2008a; Schnur et al., 2017), comprise an equally extensive record of unrest. At an average rate of 23 discrete episodes per year, our observations surpass previous estimates for activity at Monowai by one order of magnitude (Watts et al., 2012). These estimates were based on the growth rate of the volcano during the 5-day long eruption event in May 2011 and comparing it to the growth during 2007 and 2011 based on repeat bathymetric surveys. As Watts et al. (2012) point out, the growth rate observed during the 2011 event was unusually high compared to other submarine volcanoes (e.g. Kick'em Jenny in the Lesser Antilles arc) and is probably not typical of the preceding four years of activity. Irrespective, the rates of activity determined in this paper notably exceed those of other sites previously studied by the means of long-term seismoacoustic recordings, for example Macdonald Seamount and the Teahitia-Mehetia region in the South Pacific (Norris and Johnson, 1969; Talandier and Okal, 1987), making Monowai one of the most active submarine sites currently known.

At a cumulative length of 137 days of 1-min detections over the course of 3.5 years, Monowai is a major source of coherent low-frequency sound in the record of the southern hydrophone array at Juan Fernández Islands. For instance, arrivals from the volcano amount to 39% (196,949) of all detections at H03S (510,464), and more than 25% of the cumulative root-mean-square energy received in the 4-12 Hz band. Even though more sophisticated methods exist to distinguish in-water nuclear

explosions from other seismoacoustic sources, for example by performing advanced spectral analysis (e.g., Tuma et al., 2016), activity at the volcano has to be taken into account when deriving test-ban relevant calibrations of the IMS hydrophone station at Juan Fernández Islands, e.g. during the derivation of short and long-term ocean noise levels (Brown et al., 2012). At a mean correlation coefficient of 0.61, acoustic phases from Monowai also represent an extremely coherent component of the ambient sound field at the H03S array. Future studies therefore need to assess whether persistent arrivals from the volcano can interfere with the hydroacoustic detection of earthquakes and other treaty-relevant events, both of which fall in frequency and amplitude ranges similar to those of the identified volcanic episodes (Hanson et al., 2001; Hanson and Bowman, 2005b).

We find no significant relationship between local levels of seismicity and volcanism at Monowai. Over the course of the ∼3.5 years long record, less than two dozen earthquakes, usually between 4 and 6.5 m_b magnitude and focal depths greater than 100 km, were detected within a 75 km radius from the volcano. None of these events occurred during or within two days prior to a volcanic episode. Bohnenstiehl et al. (2014) observe an increase in activity at numerous submarine volcanoes in the Tofua and Tonga Arc in response to two $M_W > 8.0$ earthquakes in the southern Pacific region. Comparing events of similar magnitude ($M_W \geq 7.5$) in the South Pacific region to our record of activity shows no such effect, suggesting that the volcanic regime at Monowai may be unresponsive to the static and dynamic stress changes induced by seismic activity. We note, however, that activity triggered by external parameters, e.g. earthquakes or tidal forces, has been shown to occur at relatively low levels (Tolstoy et al., 2002) and hence, may remain undetected by the distant hydrophone array.

Previous studies report numerous, potentially active volcanic edifices in the Tonga-Kermadec Arc region (Stoffers et al., 2006; Massoth et al., 2007). Yet, only two

episodes retrieved from the ∼3.5 years long record of the H03S hydrophone array are not associated with activity at Monowai. The absence of further detections of active sites may be due to various reasons. For instance, shoaling bathymetry might block acoustic ray paths, as most known active submarine volcanoes along the Tonga-Kermadec Arc are located to the west of the crest of north-south trending Tonga and Kermadec ridge that reaches depths of 500 m or less (cf. Figure 3.8). Coupling of acoustic energy into the SOFAR domain may also be less efficient at certain sites, for example when the source is located too far below the sound channel axis (Blackman et al., 2004). Furthermore, it is possible that activity at other volcanoes is weaker, thus remaining below detectable levels, or occurs at frequencies outside the 4-12 Hz processing range used in this study.

Explosive volcanism can generate atmospheric sound waves that are frequently detected by IMS infrasound sensors (e.g., Matoza et al., 2011b, 2017). Due to the high impedance contrast of the ocean-atmosphere boundary, sound emitted by a submarine volcano can become airborne only after the edifice reaches the sea surface (Green et al., 2013; Nishida and Ichihara, 2016). However, in cases where the acoustic wavelength significantly exceeds the in-water source depth (Godin, 2007), low-frequency underwater sound waves may transcend the anomalously transparent sea surface and propagate as atmospheric signals. This process is known as evanescent wave coupling and was first observed in a geophysical system by Evers et al. (2014) for the 2004 M_W 8.1 Macquarie Ridge earthquake. During times of activity at Monowai, no corresponding arrivals are registered in the IMS processing stream at the three closest infrasound stations, i.e. IS22 at Port Laguerre (1674 km source-receiver distance), IS36 at Chatham Islands (2001 km), and IS24 at Tahiti (3014 km), suggesting that an equivalent phenomenon is not present at Monowai, and that the volcano probably failed to breach the sea surface during the time periods studied here.

3.6 Conclusion

We examined a 3.5-year record of hydrophone recordings at Juan Fernández Islands, Southeast Pacific Ocean, for long-range underwater sound waves from Monowai, Kermadec Arc. Our results show that the volcano was intermittently active between July 2003 and March 2004, and from April 2014 to January 2017. Density-based clustering of hydroacoustic arrivals identified 82 discrete episodes of volcanic activity during this time. Episodes occur on average twice per month, typically range from hours to multiple days in length, and amount to 137 days in total, making Monowai one of the most active sites of submarine volcanism currently known on Earth. Comparing acoustic and seismic measurements of earthquakes in the Kermadec Arc suggests a magnitude range of 1.4 to 4.2 m_b for detected events at the volcano. At a comparable body wave magnitude of 2.2 m_b, acoustic resolution of the H03S hydrophone array surpasses regional broadband networks by at least one order of magnitude for seismic activity at Monowai. Density-based clustering of arrivals from further persistent sources along the Tonga-Kermadec Arc revealed signs of volcanic activity at Healy or Brothers volcano in August 2015, and at a location near 23°S in the southern Tonga Arc in December 2014. Our findings are consistent with previous studies and show that remotely tracking submarine volcanic activity by the means of hydroacoustic measurements is feasible, even over basin-scale distances.

Finally, we note that the clustering algorithm applied in this study could be adapted for other array-type hydrophone deployments with relative ease, enabling the systematic scanning of waveform data for persistent sources of low-frequency ocean sound, i.e. further volcanically active sites. Our findings highlight the importance of the IMS array H03S in studying volcanism at Monowai and have implications for early warning measures: While episodes cannot be forecasted, the delay time at which ships in the area can be warned of an increase in activity at the volcano is limited only by the acoustic travel time to the H03S array and the relay time of waveform

data to the International Data Centre, all in all totaling less than three hours.

Chapter 4

Hydroacoustic investigation of the 2014 eruption at Ahyi volcano, 20.4°N Mariana Arc

The following study is intended for submission to

Geophysical Research Letters as

Metz, D. & Grevemeyer, I.,

Hydroacoustic measurements of the 2014 eruption at Ahyi volcano, 20.4°N Mariana Arc

4.1 Introduction

Ahyi is a submarine volcano located at 20.42°N, 145.03°E in the northern Mariana Arc, northwestern Pacific Ocean (Figure 4.1a). The edifice consists of a 12 km wide, hydrothermally active stratovolcanic cone that rises from approximately 2000 m to 70 m below sea level at a location 20 km southeast of Farallon de Pajaros (formerly Uracas), the northernmost island in the Northern Marianas Islands chain (Bloomer et al., 1989; Resing et al., 2009, Figure 4.1b). Reports of eruptive activity at Ahyi include discolored surface waters in 1979 (Global Volcanism Program, 1979), and

observations of seismic tertiary waves ('T phases') throughout the South Pacific region in 2001 (Global Volcanism Program, 2001). Volcanic episodes in the area date back until at least 1967, when hydrophones of the Sound Surveillance System (SOSUS) recorded a high incidence of underwater explosion sounds from a location 10 km southeast of Farallon de Pajaros (Norris and Johnson, 1969), indicating a possible source near Makhahnas Seamount. Further activity has been intermittently observed near Supply Reef, a shallow submarine volcano 30 km northwest of Maug Island, in 1969 and on at least three occasions in the 1980s (Global Volcanism Program, 2001).

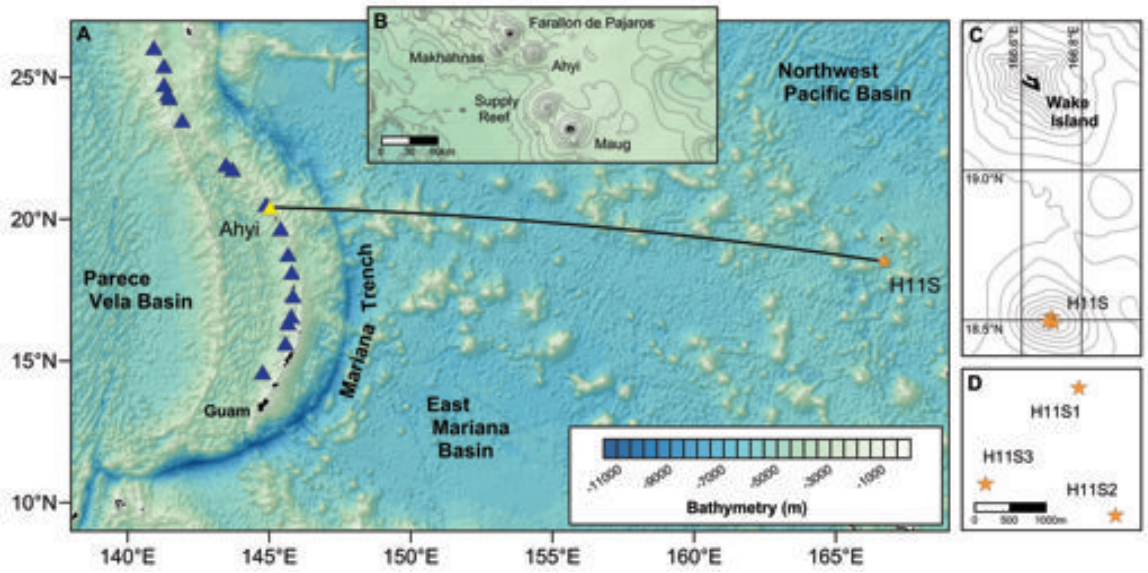

Figure 4.1: Overview map. (a) Locations of Ahyi Volcano (yellow triangle) and the H11S hydrophone array (orange star) in the northwestern Pacific Ocean. Blue triangles represent volcanic edifices with observed or inferred eruptive activity over the last 2000 years according to the Smithsonian Global Volcanism Database (Global Volcanism Program, 2013). The source-receiver distance between the volcano and H11S (black line) is 2283 km at a geodesic back azimuth of 278.9°. (b) Detailed view of the seafloor topography south of Farallon de Pajaros derived from GEBCO 2008 bathymetry. Contour colors correspond to the scale used in Figure 4.1a, with grey isolines indicating water depth at 500 m intervals. (c) Position of the H11S array 90 km south of Wake Island. Contour lines are spaced at 500 m intervals below sea level. (d) Tripartite configuration of the hydrophone elements at H11S.

In April and May 2014, Ahyi erupted over the course of two weeks. Onsite observations included explosions heard by scuba divers and aboard ships in the area, as well

as signs of volcanogenic fallout spotted at the sea surface southeast of Farallon de Pajaros (Global Volcanism Program, 2014). Over the course of the episode, broadband seismometers of the USGS Northern Mariana Islands network (FDSN code MI) and hydrophones in the western Pacific region registered a multitude of volcano-acoustic signals that were traced back to a location near Ahyi. The volcano was ultimately identified as the site of eruptive activity from repeat bathymetric mapping during a research expedition in May 2014, which showed that the summit area had given rise to a 100 m deep crater and shoaled by ∼30 m overall compared to data collected in 2003 (Haney et al., 2014). Here, the reader is referred to the Global Volcanism Program (2017b) for a more comprehensive account of all follow-up investigations, since our study is primarily concerned with the hydroacoustic record of the 2014 episode.

Measuring long-range underwater sound can be an effective tool to overcome the observational limitations inherent to the study of submarine volcanism. In the global ocean, sound waves below a few hundred hertz travel in the Sound Fixing and Ranging (SOFAR) channel (Tolstoy et al., 1949; Ewing et al., 1951), a distinct layer of minimum acoustic velocity that facilitates acoustic propagation over distances of hundreds to thousands of kilometers. For example, hydroacoustic phases associated with the 2011 eruption at Monowai, a volcanic center in the Kermadec Arc, were recorded over a source-receiver range of 15,800 km (Metz et al., 2016). Recent observations of submarine eruptions in the Mariana Arc region include long-range hydrophone recordings of explosive activity at Anatahan Volcano (Dziak et al., 2005), NW-Rota-1 (Chadwick et al., 2012; Schnur et al., 2017) and South Sarigan Seamount (Green et al., 2013).

The detection of underwater sound phases is one of the primary tasks of the International Monitoring System (IMS), a global sensor network put in place as part of the verification regime for the Comprehensive Nuclear-Test-Ban Treaty (CTBT). Six hydrophone stations, typically configured as triplet receiver arrays and moored in

the deep sound channel, are in operation worldwide to detect nuclear explosions in the global ocean. However, IMS hydrophone data has implications beyond the realm of test-ban monitoring, for example when studying tsunami signals (Matsumoto et al., 2016), and sources of low-frequency ocean noise (Woolfe and Sabra, 2015). Here, we focus on recordings of IMS station H11 at Wake Island, where hydroacoustic arrivals associated with the 2014 eruption at Ahyi were recorded across the northwestern Pacific basin and over a geodesic distance of 2283 km.

4.2 Hydrophone triplet data and processing

4.2.1 Instrumentation

Station H11 of the International Monitoring System consists of two bottom moored hydrophone arrays, located approximately 55 km northeast (H11N) and 90 km south (H11S) of Wake Island (Figure 4.1b). The three hydrophones H11S1-3 are positioned on top of a 1200 m deep seamount and moored near the local SOFAR channel axis at approximately 740 m water depth (Appended Figure B.1), with elements organized in a tripartite configuration and equidistant spacing of 2 km (Figure 4.1c). Acoustic measurements are made at 250 Hz and transmitted in near-real time to the International Data Centre (IDC) in Vienna for routine processing and analyst review (Hanson et al., 2001).

Peak acoustic amplitudes of hydroacoustic arrivals associated with volcanic activity at Ahyi are up to 5 dB higher at H11S than at H11N. The magnitude of the offset is consistent with observations by Heaney et al. (2013) for signals of the 2010 eruption at South Sarigan Seamount, and most likely reflects different degrees of transmission loss due to bathymetric blockage and scattering along the source-receiver paths. We further note that background noise levels during times of acoustic quiescence are 1-2 dB lower at H11S, resulting in an overall higher signal-to-noise ratio compared to the

northern array (factor 1.2 to 1.5). Therefore, our study focuses on the southern Wake Island hydrophone array.

4.2.2 Direction-of-arrival calculations and detection

Hydrophone recordings are corrected for instrument response and a mean and trend is removed. Data is band-pass filtered between 4 and 80 Hz to account for the broadband character of signals typically associated with submarine volcanic activity (Bohnenstiehl et al., 2014), and minimize potential noise contamination at both ends of the spectrum, e.g. due to ocean microseism (Bromirski et al., 2005), marine mammal vocalization (Sousa and Harris, 2015), and commercial shipping (Sirovic et al., 2013). Since instruments are moored at similar water depths (∼740 m) and the array aperture is multiple orders of magnitude smaller than the distance between Ahyi and H11S, direction-of-arrival calculations follow a two-dimensional plane-wave fitting approach (Del Pezzo and Giudicepietro, 2002). Hydroacoustic recordings are subdivided into 1-min long, non-overlapping windows. Peak delay times t_{ij} between instrument pairs located at relative positions x_{ij} are derived from normalized cross-correlation of the windowed data. We obtain the slowness vector $p \equiv (p_x, p_y)$ of a planar wave front moving across the triplet array by solving the following equation in a least-square sense:

$$t_{ij} = p \cdot \Delta x_{ij} \tag{4.1}$$

Hence, apparent sound speed v and back azimuth θ are derived from

$$v = \left({p_x}^2 + {p_y}^2\right)^{-1/2} \tag{4.2}$$

and

$$\theta = tan^{-1}\left(\frac{p_x}{p_y}\right). \tag{4.3}$$

To eliminate arrivals not traveling in the deep sound channel, 1-min windows with a sound speed below 1400 or above 1600 m/s are omitted from the data set (cf. Hanson and Bowman, 2006). Derived travel time differences t_{ij}, t_{jk}, and t_{ki} between the three hydrophone pairs are summed to obtain the closure value cl of the windowed cross-correlation. cl is assumed to approach zero for well-correlated signals and thus provides a quality constraint for extracting coherent acoustic phases from the ambient noise field:

$$cl = t_{ij} + t_{jk} + t_{ki} \tag{4.4}$$

The detection threshold of the closure function is set to a maximum of |48| ms, which corresponds to a mismatch of 12 sampling intervals at 250 Hz and is consistent with values used by Graeber and Piserchia (2004) for IMS hydrophone arrays in the Indian Ocean.

4.3 Hydroacoustic observations

Volcanic activity at Ahyi begins at 00:30 UTC 24 April 2014, when the H11S hydrophone array registered high incidences of short (< 15 sec) transient arrivals spaced seconds to minutes apart and with sharp onset and termination, most likely representing an ensemble of shallow volcano-tectonic seismicity and explosions in the frequency band of up to 80 Hz (Figure 4.2a). This main episode is preceded by a minute-long, broadband impulse at 21:00 UTC 23 April, followed by two circa 30-min long bursts at 21:20 and 22:20 UTC. While the shape of the first event strongly resembles a T phase generated by a shallow focus (< 10 km) seismic event and is different from the elongated, low-frequency (< 10 Hz) arrivals generated by tectonic earthquakes (Yang and Forsyth, 2003), the two bursts exhibit sustained peak frequencies at 16 (21:20 UTC) and 6 Hz (22:25 UTC) and thus could be interpreted as tremor caused by resonance in a fluid-filled crack or conduit (Chouet, 1996). We speculate that these precursory

signals represent the initial breaching of the magma chamber walls and subsequent flow and pressure oscillations (Bohnenstiehl et al., 2013), which are then followed by the rise and opening of the magma-filled conduit and the onset of persistent activity approximately 3.5 hours later (see also Appended Figure B.2). In an alternative scenario, the spectral banding could be explained by the interference of seafloor and sea surface reflected acoustic phases that arrive at the H11S array with small time delays ('multipathing', cf. Matsumoto et al., 2011; Dziak et al., 2015). We note, however, that, since comparable arrivals are not observed during later stages, this assumption fails to explain the distinct occurrence of harmonic signals at the beginning of the volcanic episode as well as the notably different fundamental frequencies of the two presumed tremor events.

Between 23 April and 8 May 2014, 1-min detections distinctly stabilize at a back azimuth of 278.5 ± 0.3° and within 0.5° of the geodesic angle of arrival for a source Ahyi (Figure 4.2b-c, see also Appended Figure B.3). A small number of arrivals registered from ∼277.6° at the same time probably represent reflections off Maug Island. Notably, no activity at Ahyi is detected at H11S in the weeks prior to the 2014 event. Since our observations are in agreement with local eyewitness reports (cf. Global Volcanism Program, 2014) and seafloor topography suggests no other volcanically active sites along the great circle path between the volcano and the hydrophone array, we interpret low-frequency arrivals shown in Figure 4.2b-c (blue circles) to be associated with the eruption at Ahyi. During the 15 days long episode, RMS amplitudes exceed pre-eruption background levels by 10-30 dB and typically range from 100 to 130 dB re 1 μPa in the 4-80 Hz frequency band, with 180 to 380 1-min detections counted per 12 hour interval (Figure 4.2d-e). An initial ramp up and drop in activity over the first three days of the main episode is followed by a period of gradual increase and decline of RMS levels and detection rate over approximately 12 consecutive days. We interpret this progression as an initial phase of stress release, possibly involving the deflation of

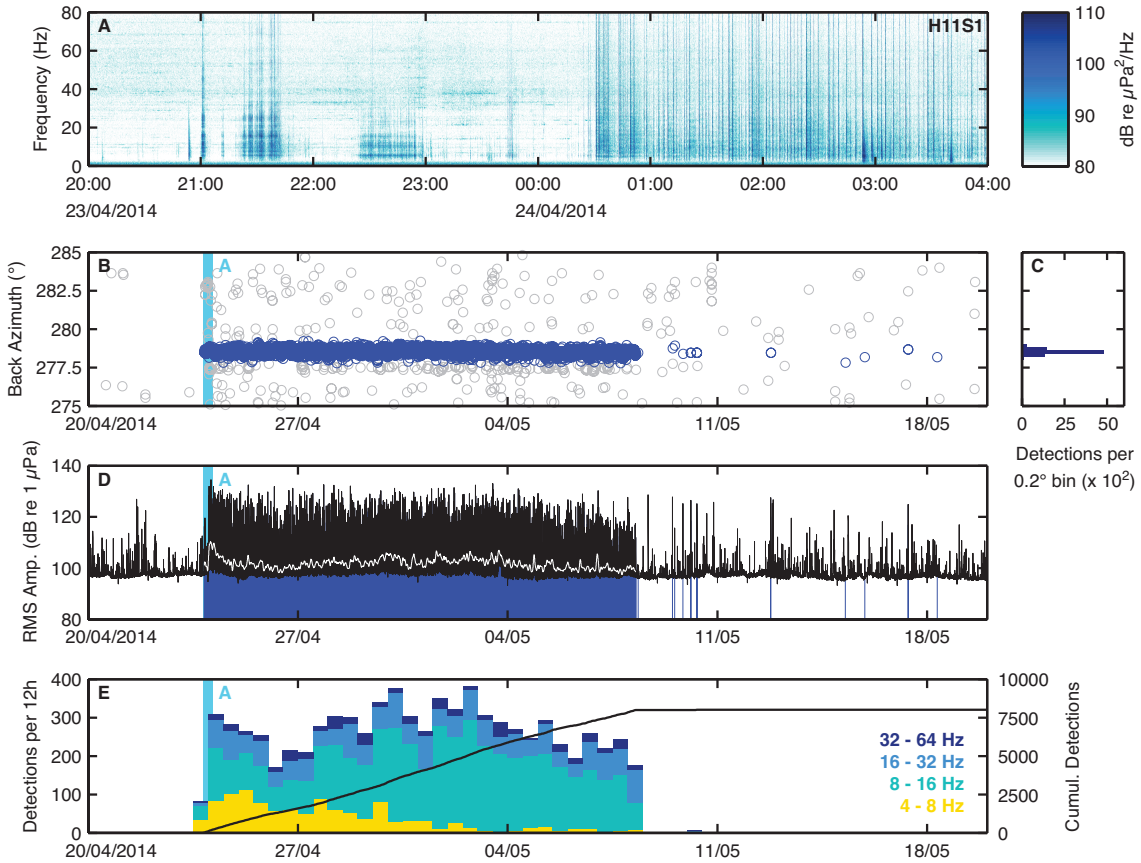

Figure 4.2: Hydroacoustic observations of volcanic activity at Ahyi. (a) Single receiver spectrogram of the H11S1 hydrophone data, beginning at 20:00:00 UTC 23 April 2014. A 1 Hz high-pass filter is applied to minimize background noise levels. (b) Back azimuths of 1-min detections between 20 April and 20 May 2014. Arrivals associated with the eruption (blue circles) are symmetrically distributed around 278.5 ± 0.3° at two standard deviation uncertainty (c). (d) Root-mean-square (RMS) amplitudes calculated over 1-min windows in the 4-80 Hz frequency band. For orientation, the white line indicates a one-hour trend. Dark blue stems correspond to detections shown in (b) and form a continuous band during the 15 days long main burst of activity. (e) Detections from Ahyi per 12h interval and peak frequency distribution across four octave bands between 4 and 64 Hz. A cumulative sum of 8003 detections (black line) is registered between 21:00 UTC 23 April and 08:06 UTC 18 May 2014. The light blue area in the bottom three subplots marks the position of the 8h-spectrogram shown in (a).

a shallow magma reservoir and subsequent formation of the newly-developed summit crater (Fornari et al., 1984), succeeded by a prolonged stage of re-pressurization until the system regains equilibrium and the volcano becomes acoustically dormant again. After 8 May, only a dozen isolated, explosion-type events are registered by the H11 hydrophones.

In a further step, we assess the peak frequency distribution of the 1-min detections in four octave bands between 4 and 64 Hz over the course of the eruption (Figure 4.2e). While arrivals in the upper bands follow a relatively uniform distribution over time, there is a notable decline in detections with peak frequencies below 8 Hz that become near absent during the second half of the episode. This trend can be observed at both H11 hydrophone arrays, and is not found in the data of 1-min windows eliminated during processing, i.e. the ambient ocean noise field. Hence, we interpret the decrease in low-frequency arrivals as a change in signal source parameters. Since volcano-acoustic signals at frequencies below ∼10 Hz are typically associated with fluid movement and oscillation in highly pressurized systems (e.g., Neuberg et al., 2006; Matoza and Chouet, 2010), their gradual cessation may be due to lower pressure gradients and subsequently reduced magma flow within, or into, the volcanic conduit towards the end of the eruption. In contrast, higher frequency events typically result from brittle fracture and, in a submarine environment, explosions at the seafloor-ocean interface (cf. Caplan-Auerbach et al., 2017), which would explain their continuous presence throughout the episode.

4.4 Resolution and seismic magnitude estimate

RMS levels of the 8003 1-min detections associated with volcanic activity at Ahyi follow a right-skewed normal distribution with a steep decline towards lower amplitudes (Figure 4.3a), indicating that events below a certain threshold may not be fully

detected. We therefore derive the acoustic resolution of the data set, also referred to as the magnitude of completeness in seismic catalogues, according to the maximum curvature method by Wiemer and Wyss (2000), in which the data bin with the highest number of detections represents the sound pressure level above that all arrivals can be successfully identified. In the case of volcanic activity at Ahyi, acoustic resolution is assumed to be 98 dB re 1 μPa.

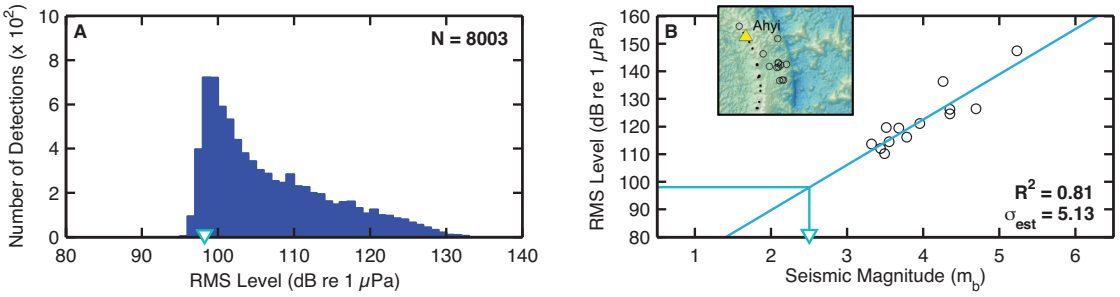

Figure 4.3: Resolution and comparable seismic magnitude. (a) RMS amplitude distribution of 1-min detections recorded at IMS hydrophone H11S1. Data is binned to 1 dB intervals. The green triangle marks the level of acoustic resolution at 98 dB re 1 μPa, calculated according to Wiemer and Wyss (2000). (b) RMS pressure amplitude of 13 earthquakes (black circles) registered by the IMS seismic network and hydrophone H11S1 between 2012 and 2017. Events are located along the central Mariana arc at 2283 $\pm$ 250 km distance from the H11S array and up to 80 km focal depth (see inset for epicenter locations). The linear relationship between acoustic and seismic magnitude (bright blue line) is significant at an error of 5.13 dB and accounts for 81% of the variance in the data set (R^2 = 0.81). Following the derived trend, acoustic resolution of 98 dB re 1 μPa corresponds to a body wave magnitude of 2.5 m_b (green line and triangle).

In order to infer comparable seismic magnitudes of events at Ahyi, we relate acoustic and seismic measurements of tectonic earthquakes registered by the global IMS network along the central Mariana Arc (Figure 4.3b). We account for potential attenuation of the earthquake signal in the solid earth and along the deep sound channel by limiting the data set to events with a catalogued depth of less than 80 km and a source-receiver distance similar to the great circle path between Ahyi and the southern Wake Island array, i.e. 2283 $\pm$ 250 km. Since RMS amplitudes are routinely calculated over the entire length of the arrival in the IMS processing stream, data is

further constrained to events with an arrival length of 40 to 80 seconds at the H11S1 hydrophone to match the 1-min segmentation of our aggregate approach (Appended Table B.1). The equation of the regression line in Figure 4.3b,

$$RMS\ Level\ (dB\ re\ 1\ \mu Pa) = 56.9 + 16.3 m_b \tag{4.5}$$

indicates a surprisingly linear relationship between acoustic and seismic magnitude ($R^2 = 0.81$) and is consistent with observations by Pulli and Upton (2002) for earthquakes in the Indian Ocean. A minimum seismic magnitude of 2.5 m_b, corresponding to the acoustic resolution of 98 dB, can be successfully resolved at H11S1 and is almost one order lower than the smallest tectonic earthquake detected by the global IMS seismometer network in the central Mariana Trench region. Using the derived trend as a first order approximation, we estimate comparable body wave magnitudes for events at Ahyi between 2.5 and 4.6 m_b, which is, for example, similar to presumed levels of activity at Brothers Volcano (2.4 to 3.2 m_b) in the Kermadec Arc (Dziak et al., 2008), and at Fukutoku-Okanoba in the Volcano Islands (3.5 to 4.7 m_b, Dziak and Fox, 2002).

4.5 Acoustic energy release

Due to its potentially harmful effect on marine ecosystems, underwater noise from anthropogenic sources, in particular commercial shipping (McKenna et al., 2012) and seismic exploration (Nieukirk et al., 2004), has become an increasingly relevant topic in ocean conservation and policy making (e.g., Papanicolopulu, 2011; Williams et al., 2015). Yet, there exists little knowledge on the contribution of solid earth processes, i.e. earthquakes and volcanic activity, to the ocean soundscape. Following procedures outlined by Hildebrand (2009) and previously implemented by Bohnenstiehl et al. (2013), we therefore attempt to quantify the amount of acoustic energy radiated into

the water column during the 2014 eruption at Ahyi.

In a first step, acoustic intensity I is derived from (units in brackets)

$$I = \frac{p^2}{z} \quad (\mathrm{W/m^2}) \tag{4.6}$$

where p represents the source pressure level at 1 m distance and the specific acoustic impedance z is given as the product of the nominal density and sound speed of seawater, fixed at 1030 kg/m^3 and 1480 m/s, respectively. Assuming that energy at the volcano is released into an acoustic half-space, we calculate the signal power P as the product of intensity and the geometric factor 2π:

$$P = I \times 2\pi \quad (\mathrm{J/s}) \tag{4.7}$$

Finally, acoustic energy E is defined as the linear product of power and duration T:

$$E = P \times T \quad (\mathrm{J}) \tag{4.8}$$

The above calculations are carried out in non-overlapping 1-sec windows over the 8003 1-min detections registered at hydrophone H11S1 during the eruption, resulting in a total of 480,180 measurements. Background noise levels of 97 dB, corresponding to 1 dB below the acoustic resolution of the array, are removed beforehand (Holt et al., 2009). Results from range-dependent parabolic equation modeling (Collins, 1993) indicate a mean transmission loss of 141 dB along the 2283 km long source-receiver path for signals in the 4-80 Hz band (Figure 4.4), and are accounted for in the subsequent calculation of pressure levels referenced to 1 m distance from the source (Matsumoto et al., 2011).

Results show that during the eruptive episode, source levels at Ahyi were on the order of 245-275 dB re 1 μPa at 1 m and a total of 9.7 10^{13} J of acoustic energy

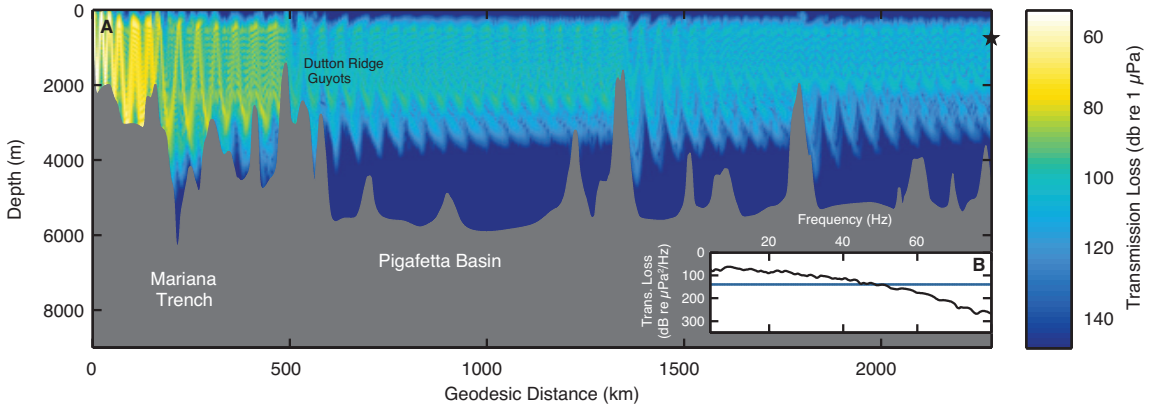

Figure 4.4: Transmission loss estimates obtained from a two-dimensional parabolic equation model (RAM, Collins, 1993). (a) Exemplary source-receiver profile for a 32 Hz signal between Ahyi and the H11S1 hydrophone (black line in Figure 4.1a). The instrument is moored at a distance of 2283 km and near 750 m water depth (black star). The model assumes a source at 70 m below sea level, corresponding to the approximate summit depth of the volcano. Bottom properties are set to 1700 and 2200 m/s for sound speed, with corresponding attenuation parameters of 0.3 above and 0.05 dB/m/kHz up to 150 m below the seafloor, respectively. Sound speed profiles are calculated every kilometer according to Mackenzie (1981), using water column data provided by the 2005 World Ocean Atlas. Bathymetry is taken from the 2008 GEBCO grid and sampled at 100 m intervals. (b) Transmission loss for frequencies in the 4-80 Hz band (black line) calculated at 0.2 Hz intervals and smoothed using a 1 Hz wide moving-average filter. The blue line marks the mean at 141 dB re 1 μPa at 1 m.

was radiated in the 4-80 Hz band over the course of 8003 minutes (∼5.6 days). The yield estimate is similar to calculations by Bohnenstiehl et al. (2013) for the 2009 eruption at Hunga Ha'apai-Hunga Tonga volcano in the Tonga Arc (1.7 to 4.7 10^{13} J over 2.7 days), and confirms that the contribution of submarine volcanic activity to the ocean soundscape is indeed substantial. For example, acoustic energy released at Ahyi exceeds the annual input from seismic surveying by a factor of two (3.9 10^{13} J, Hildebrand, 2005), and is almost four times higher than previous estimates for the cumulative energy of all sonar activities in the global ocean combined (2.6 10^{13} J, Hildebrand, 2005). However, unlike underwater noise produced by sonar, ship traffic and seismic surveying, volcanic episodes represent intense, yet localized and often short-lived events. Hence, their ecological impact remains difficult to assess, and

it is not known to which degree marine mammals are affected by, or have become habituated to, these natural sources of low-frequency sound.

4.6 Conclusion

An IMS hydrophone station located at Wake Island, Northwest Pacific Ocean, detected underwater sound phases associated with the 2014 eruption at Ahyi. Volcanic activity occurred in two bursts over the course of 15 days, preceded only by a 3.5-hours long period of precursory events. There is a notable absence in low-frequency (< 8 Hz) arrivals during the later stages of the eruption, which could be interpreted as the result of decreasing pressure gradients and subsequent reduction in fluid movement in the volcanic system. We exploit the linear relationship between acoustic RMS amplitude and body wave magnitude of shallow tectonic earthquakes along the Mariana Arc to approximate the seismic range of activity at Ahyi. The resolution of the H11S hydrophone array surpasses broadband network data by more than half a magnitude, successfully identifying seismic events at Ahyi as low as 2.5 m_b. Acoustic energy released during the eruption is on the order of 9.7 10^{13} J, suggesting that the contribution of solid earth sources to the ocean soundscape may be much higher than previously thought. Our findings highlight the potential of the Wake Island hydrophone array for remotely studying volcanic activity at Ahyi and may aid in detecting further active sites along the Mariana Arc, and elsewhere, in the future.

Chapter 5

Conclusion

5.1 Summary

We have demonstrated that the remote detection of submarine volcanic activity using International Monitoring System (IMS) hydroacoustic data, even over basin-scale source-receiver distances, is indeed feasible. The key findings of the studies undertaken in this thesis can be summarized as follows:

- Low-frequency underwater sound waves generated by the May 2011 eruption at Monowai, a submarine volcano in the northern Kermadec Arc, are detected by an IMS hydrophone array located at Ascension Island, Equatorial Atlantic Ocean, and over the unprecedented source-receiver distance of ∼15,800 km.

- Combining results from direction-of-arrival calculations and cross-correlation of waveform data recorded by one of the hydrophones and a broadband seismometer located at Rarotonga, Cook Islands, unambiguously identifies Monowai as the signal source.

- Results from transmission loss modeling suggest that acoustic propagation at southern latitudes is facilitated by the anomalous temperature regime of the

Antarctic Circumpolar Current, which causes an upward shift of the SOFAR channel axis and thus reduces the effect of bathymetric obstruction along the source-receiver path.

- Using the record of IMS station H03, Juan Fernández Islands, density-based clustering of hydroacoustic arrivals reveals 82 discrete episodes of volcanic activity at Monowai during the periods when data was available, i.e. between July 2003 and March 2004, and from April 2014 to January 2017. Episodes are typically spaced days to weeks apart and last from six hours up to 14 days. At a combined total of 137 days of arrivals over the course of ∼3.5 years, Monowai is one of the most active submarine arc volcanoes currently known.

- The timing of volcanic episodes is consistent with observations of discolored water and pumice rafts near Monowai and previous studies of T phase seismicity.

- Comparing seismic and acoustic magnitudes of shallow tectonic earthquakes along the Kermadec Arc places detected seismic events at the volcano between 1.4 and 4.2 m_b

- Further observations suggest volcanic activity at a location near 23°S in the southern Tonga Arc in December 2014, and at the Healy or Brothers volcano in the southern Kermadec Arc in August 2015.

- Acoustic phases associated with the 2014 eruption of Ahyi volcano, Northern Mariana Islands, can be identified in the record of IMS station H11 at Wake Island, northwestern Pacific Ocean.

- Explosive volcanic activity occurred in two bursts over the course of 15 days. Activity is accompanied by a notable decrease in arrivals below 8 Hz that is interpreted as a shift in signal source parameters, potentially caused by the

gradual reduction in pressure-driven oscillation and fluid flow towards the end of the eruption.

- Seismic events as low as 2.5 m_b are successfully identified in the record of the H11S array, thus surpassing the resolution of broadband network data by more than half an order of magnitude.

- Acoustic energy released during the eruption at Ahyi is on the order of 9.7 10^{13} J, indicating that the activity contributed substantially to the low-frequency ocean soundscape.

- The methods developed and implemented in the study of Monowai and Ahyi are suitable for detecting and tracking activity at these two submarine volcanoes in the future, and for identifying persistent acoustic sources, i.e. further volcanically active sites, in the record of other IMS hydrophone arrays.

5.2 Concluding remarks and recommendations

Following the investigation of the long-term record of activity at Monowai from IMS data, future studies could involve the systematic scanning of hydrophone triplet recordings for persistent sources of low-frequency sound. For instance, density-based clustering of arrivals registered at IMS station H11, Wake Island, may aid in identifying further volcanic episodes along the Izu-Bonin-Mariana Arc, which hosts a number of potentially active sites (Baker et al., 2008; Resing et al., 2009), at least two of which, South Sarigan Seamount and Ahyi, erupted since the installation of the hydrophone arrays in 2009 and were retrieved successfully in the hydroacoustic record (Green et al., 2013; Heaney et al., 2013). Complementing IMS data, spatial coverage of such an attempt could be improved by the use of auxiliary systems, for example the DONET multi-sensor network currently deployed in the Nankai Trough, Japan (e.g.,

Nakano et al., 2013). In an analogous study, data from the IMS hydrophone arrays recently installed at Crozet Islands in the southern Indian Ocean may provide insights into volcanic activity in the South Sandwich island arc, which is located within the unobstructed field of view of the station at approximately 5000 km source-receiver distance.

Density-based clustering of arrivals registered at the northern hydrophone array at IMS station H10, Ascension Island, shows that Monowai was intermittently active between 2005 and 2016 (Appended Figure C.1). However, a quantitative comparison with data recorded at IMS station H03, Juan Fernández Islands, indicates that acoustic resolution is insufficient at the H10 arrays to reliably detect and track activity at the volcano. This is most likely due to the increase in transmission loss along the significantly longer source-receiver path. Observations of volcanic signals from Monowai at both H10 and H03 hydrophones could be analyzed in more detail in the future, for example by directly relating spectral properties and arrival times of acoustic phases, and subsequently reconciling such measurements with results from broadband transmission loss modeling and ray tracing (Blackman et al., 2004; de Groot-Hedlin et al., 2009). Since relative travel time differences between the two hydrophone stations are in essence a function of temperature gradients along the source-receiver path (Munk, 1989), studying changes of such differences over longer periods may aid in identifying both seasonal or multi-year trends in the Southern Ocean, thus using acoustic propagation of signals from the volcano as a natural thermometer with which to monitor the temperature of the ocean (Munk and Forbes, 1989; Dushaw and Menemenlis, 2014)

Due to the high sensitivity of the acoustic measurements compared to conventional seismic recordings, IMS hydrophone data is not only suited to study the distribution and rates of seismicity along subduction zones and mid-oceanic ridges (Hanson and Bowman, 2005b), but also comprises an extensive record of ice-generated sounds, in

particular at stations positioned below the 30°S parallel. We note, for example, that aside from arrivals from Monowai, which represents the largest individual source of low-frequency sound in the record of the H03S array, a multitude of acoustic phases from southern latitudes, primarily corresponding to parked and drifting icebergs in a region north of the Ross Ice Shelf (Talandier et al., 2006) and along the western coast of Marie Byrd Land, can be observed in the record of the IMS station at Juan Fernández Islands (Appended Figure C.2). In an effort similar to previous studies by Chapp et al. (2005) and Evers et al. (2013), who use hydrophone triplet data to investigate the distribution of ice-generated tremor and calving icebergs in the Indian Ocean, it therefore appears feasible to combine recordings from IMS arrays H01W, located offshore Cape Leeuwin, Western Australia (cf. Figure 1.8), and H03S to detect and track sources of ice-generated noise in the southern Pacific Ocean.

In order to achieve the objective of the study at hand, i.e. to detect volcano-acoustic arrivals and to compile a continuous record of activity at Monowai, we used a plane-wave-fitting routine whose detection parameters were primarily based on signal coherence, represented by the cross-correlation coefficient averaged across the triplet array and the value of the closure function (cf. Chapter 3.2.2). Such an approach is advantageous when isolating arrivals of unknown shape, number, or low signal-to-noise ratio from a continuous data stream at minimal computational cost, but is of limited use when a more qualitative assessment is needed. For example, the fixed segmentation of the band-pass filtered data does not facilitate the analysis of exact arrival times, duration, or frequency content, which may be required to estimate the source location, compare signals recorded at multiple receiver sites, or to assess the distribution of energy over time and across multiple frequency bands for further processing and classification. Future attempts may therefore include more sophisticated detection methods, using, for instance, the progressive multichannel-correlation method (PMCC, Cansi, 1995), which can provide such advanced analysis, is already

integrated in the automated IMS processing stream of array-type data and has been, for example, successfully adapted for the tracking of the rupture propagation of the 2004 M_W 9.0 Sumatra earthquake from hydrophone recordings (Guilbert et al., 2005). However, comparing the list of arrivals produced by the PMCC-based algorithm used in IMS data processing, summarized in the *hydro_features* table of the final Standard Event List (SEL3), to detections made from the plane-wave-fitting routine outlined in Chapters 3 and 4 of this study reveals a significant difference in acoustic resolution. For example, over the course of the approximately 24-hour long episode in June 2014 (cf. Figure 3.3), less than 120 hydroacoustic arrivals were identified in the record of the H03S array using PMCC analysis, compared to 801 1-min detections via plane-wave-fitting. This notable offset can be explained by the different parameter setting within the PMCC module of the IMS processing stream, which is geared towards the identification of arrivals generated by tectonic earthquakes or in-water nuclear explosions rather than volcanic activity and misses the majority of arrivals due to their low signal-to-noise ratio. Nonetheless, this case shows that a precise knowledge of the 'target signal' is required for the identification of volcano-acoustic arrivals: Had the results of the PMCC analysis been used in the clustering of acoustic phases during the investigation of the long-term record of activity at Monowai, either no or a much shorter volcanic episode would have been identified, depending on the timing of the detected arrivals.

Hence, we conclude that results gained from the analysis of long-range underwater sound waves from Monowai, Ahyi, and other volcano-acoustic sources must be interpreted with great care and in consideration of the limitations of the applied processing methods and detection parameters, in particular where evidence from secondary observations, e.g. measurements from locally deployed seismometers or, in the case of an explosive eruption, repeat bathymetric mapping, is not available. Following previous efforts by Watts et al. (2012) and Green et al. (2013), future studies would

therefore benefit from a combination of onsite observations and long-range acoustic measurements to better characterize submarine volcanic activity.

5.3 Future work

The results presented in the previous section provide ample motivation for further research, involving both new instrument deployments and pre-existing IMS data. Due to the frequency of volcanic episodes, Monowai is an ideal site for studying the processes associated with submarine arc volcanism. Furthermore, the IMS hydrophone network is suited to tackle geophysical phenomena beyond the realm of underwater volcanism. Two examples of potential next steps are outlined below.

5.3.1 Deploying ocean bottom seismometers at Monowai

IMS hydrophones have proven to be a suitable tool for detecting episodes of volcanic activity at Monowai in the acoustic far field. However, such long-range measurements lack the resolution of local networks and provide limited information on exact location, depth, magnitude, and focal mechanism of seismic events within the volcanic edifice. These parameters are routinely derived for many well-monitored subaerial volcanoes around the world (e.g., Power et al., 2013), and have proven critical for detailed investigations of volcanic processes (Ketner and Power, 2013; Rodgers et al., 2013), for example when tracking magma ascent prior to an eruption (Aki and Koyanagi, 1981) and studying the influence of tidal forcing on volcanic activity (e.g., McNutt and Beavan, 1981; Sottili and Palladino, 2012).

The shortcomings of long-range acoustic measurements can be overcome by the ship-based deployment of ocean bottom seismometers (OBSs) at the seafloor. Figure 5.1a shows a possible configuration for a set of 19 instruments distributed around Monowai, 15 of which are configured in a double ring-shaped pattern at distances of

8-10 and 25-35 km, respectively. Using an inner and outer ring of sensors enhances network resolution for seismic sources located at or underneath the volcanic center and assures data redundancy in case instruments are lost, either due to technical failure or in the event of a larger eruption. Notably, high-resolution multibeam and backscatter data are available for all chosen sensor locations, none of which were affected by changes in seafloor depth due to volcanic activity in the past (Watts et al., 2012). An additional four OBSs could be placed at distances of 120-150 km to study acoustic propagation in the far field and monitor regional seismicity. Aperture and number of instruments of the network outlined here resemble subaerial monitoring systems, e.g. at Mt. Taranaki, New Zealand (Sherburn and White, 2006), or Piton de la Fournaise, Réunion island (Battaglia and Aki, 2003), and are configured for the measurement of P and S wave arrivals at multiple receiver sites to enable standard seismic event detection and relocation.

We further suggest the implementation of two seismic triplet arrays (ARE and ARW), located at opposing sides of the center (Figure 5.1b), to detect signals from the volcano that travel as direct waves at the seafloor-ocean interface, also known as 'Ti phases'. These phases typically propagate at group velocities of around 1500 m/s (Butler and Lomnitz, 2002; Butler, 2006) and, similar to 'conventional' T phases passing through the deep sound channel, experience little attenuation at frequencies below 100 Hz, thus facilitating a tripartite array configuration comparable to IMS hydrophone stations. Recording Ti phases at local OBS sensors represents a cost-efficient, feasible alternative to temporary moorings of SOFAR hydrophones when studying volcanic activity at Monowai from short distance.

Since array tracking of Ti phases is essentially a two dimensional problem, it can be addressed by the same plane wave fitting procedure applied to IMS hydrophone data in Chapters 3 and 4 of this thesis. However, given the shorter distance between Monowai and the local OBS arrays, it is necessary to re-evaluate the validity of the

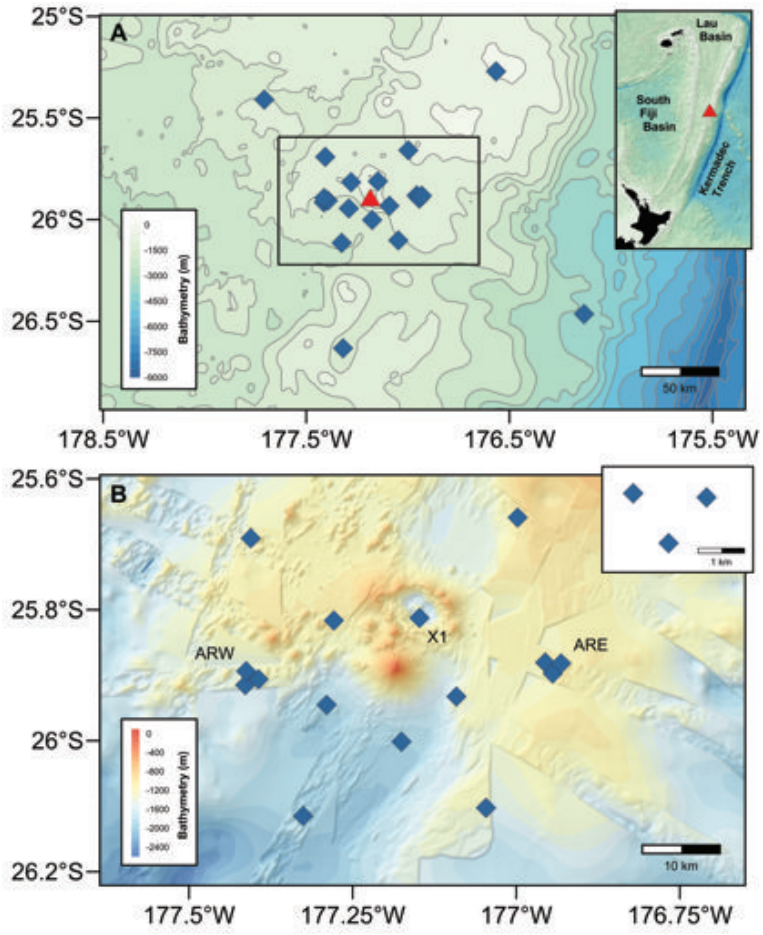

Figure 5.1: Potential configuration for a temporary deployment of ocean bottom seismometers at Monowai. A total of 19 instruments (blue diamonds) are distributed around the volcano (red triangle). In order to minimize hypocenter relocation errors, five sensors are configured in a pentagonal configuration at distances between 8 and 10 km from the cone, with another four elements at 25-35 km to ensure data redundancy. Four further OBSs could be placed at distances of 120-150 km along the to study signal propagation in different directions, i.e. along the arc, into the back arc, and the South Pacific Ocean. The network includes two seismometer triplet arrays located at opposing sides to the west (ARW) and east (ARE) of the main stratocone for deriving signal back azimuths (see inset of Figure 5.1b for configuration), thus providing additional constraints on source location. The instrument at location X1 is located within the hydrothermally active caldera (Leybourne et al., 2012) and could be equipped with additional sensors, e.g. for measuring temperature, turbidity, bottom pressure, tilt, or strong motion.

planar wave front assumption, which requires a minimum source-receiver range d_n in order to be true in the experimental sense. Following Ryan (1998), we can calculate d_n as a function of the angle of arrival θ, the wavelength of the incoming signal λ, and array aperture L:

$$d_n = \frac{(L\ sin\ \theta)^2}{2\lambda} + \frac{L}{2}\,|cos\ \theta| - \frac{\lambda}{8} \tag{5.1}$$

According to the argument of Hanson and Bowman (2006), the angle of arrival for at least one sensor pair in a tripartite array is always close to 30°, which allows us to substitute the sine and cosine term in (5.1) with 0.5 and 0.87, respectively. Assuming a maximum target frequency of up 50 Hz, which corresponds to the Nyquvist range of a potential sampling rate of 100 Hz, and a sensor spacing of 1.5 km, d_n is calculated at 11 km. Hence, the arrays ARW and ARE are positioned at more than twice the radius of the inner ring of seismometers ($\sim$20 km) to facilitate the use of plane wave fitting.

We note that studies of submarine volcanic activity that involve local, long-term deployments of seismometers so far only exist for Vailul'u Seamount, the active end member of the Samoan hot spot trail (Konter et al., 2004), Axial Volcano on the Juan de Fuca Ridge (Tolstoy et al., 1998), and Brothers Volcano in the southern Kermadec Arc (Dziak et al., 2008). Given its comparably high, steady rate of activity, Monowai is an ideal target site to add to this record: A deployment of six to eight months may already yield data on more than a dozen volcanic episodes, assuming the rate of two events per month derived in Chapter 3 still holds. Combining results from high-resolution seismic measurements with other surveying techniques, for example by equipping one instrument within the hydrothermally active caldera with temperature, turbidity, tilt, and strong motion sensors (OBS X1 in Figure 5.1b), would provide a detailed insight into the mechanics of activity at Monowai over a longer timescale, and help us to better understand submarine arc volcanism in general. Naturally, repeat

bathymetric mapping of the main edifice could be carried out during the deployment and recovery mission of the OBS fleet, adding to the pre-existing multibeam record.

5.3.2 The suprapodal T phase of the 2014 M_W 7.3 Papanoa earthquake, Mexico

At 14:27:24 UTC 18 April 2014, a M_W 7.3 earthquake occurred at 17.39°N, 100.97°W near the Pacific coast of Mexico. Located at a focal depth of 24 km and within 75 km of the Middle America Trench, the event is deemed to have been part of a slow slip sequence that had begun two months earlier within the Guerrero segment of the Cocos-North America subduction zone (Radiguet et al., 2016). Preliminary results suggest that hydroacoustic phases generated by the earthquake were recorded at the IMS hydrophone station located at Diego Garcia, Indian Ocean (Figure 5.2). At a range of ∼21,354 km, the suprapodal signal would thus exceed the source-receiver distance achieved by the 1960 Australia-Bermuda Sound Transmission Experiment (19,820 km, Munk et al., 1988) and the previously discussed observations of volcanic activity at Monowai (15,800 km, Metz et al., 2016), making it the furthest hydroacoustic transmission to have ever been observed on Earth.

We adapt the processing parameters of the plane-wave-fitting routine outlined in the previous chapters to study the 2014 Papanoa earthquake signal in the record of the H08S array. Acoustic data is band-pass filtered at 2-20 Hz and binned to 12-sec windows with 50% overlap. Detection thresholds are set to 1400-1600 m/s, 0.3, and 48 ms for apparent sound speed, cross-correlation coefficient, and closure function, respectively. Acoustic phases associated with the M_W 7.3 main shock are registered from a southeastern direction after approximately four hours (Figure 5.3), which is consistent with the nominal time of arrival for a signal traveling in the deep sound channel. The observed signal back azimuth (153.1°) appears to be slightly different from the geodesic value of 148.5°. This offset may be, in part, explained by the uncer-

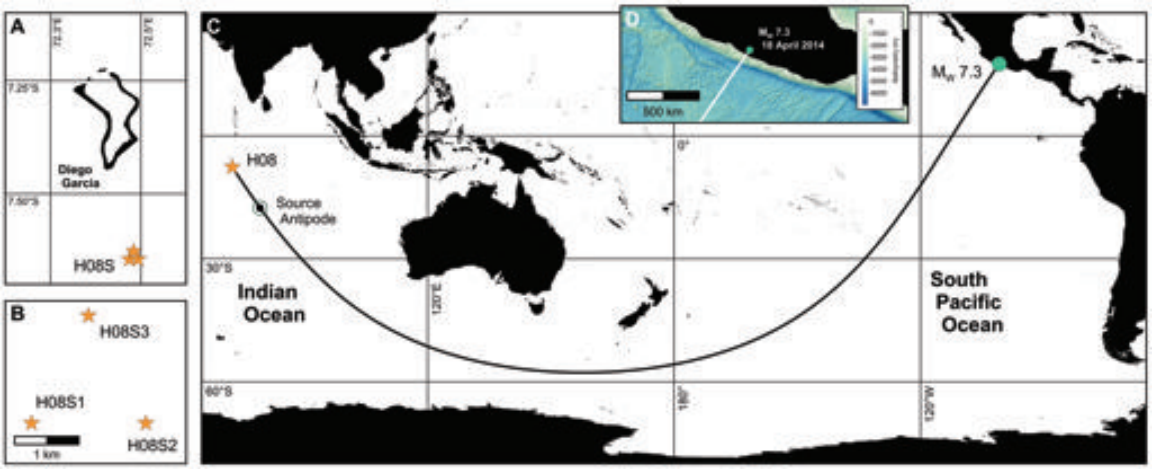

Figure 5.2: Overview map. (a) Position of IMS array H08S, located 25 km south of the Diego Garcia atoll in the Indian Ocean. (b) Tripartite configuration of the hydrophone elements. (c) Location of IMS station H08 (orange star) and the epicenter of the 2014 M_W 7.3 Papanoa earthquake (green filled circle). The geodesic source-receiver distance (solid black line) is 21,354 km, thus surpassing the source antipode (black and green circle) by ∼1316 km ('suprapodal' distance). (d) Detailed view of the earthquake source region and seafloor topography. The hypocenter of the main shock is located at 17.39°N, 100.97°W along the Cocos-North America subduction zone.

tainty that is inherent to the process of seismoacoustic coupling at the seafloor-ocean interface (Pulli and Upton, 2002). As the injection of energy into the deep sound channel can occur tens to hundreds of kilometers away from the earthquake epicenter (Graeber and Piserchia, 2004), corresponding signal back azimuths deviate accordingly, an effect most noticeable at source-receiver distances close to the antipodal range (cf. Munk et al., 1988). Consider, for instance, a coupling point at a position only 75 km west of the main rupture zone rather than at the initial focal point of the M_W 7.3 event (cf. Gualandi et al., 2017; Mendoza and Martinez Lopez, 2017). The offset from the geodesic value is now reduced to less than 1.0°, which is on the order of the angular deviation observed along the Monowai-Ascension Island trajectory (cf. Figure 2.3).

Interestingly, the H08S array also facilitates the detection of seismic events located further east along the Middle America Trench, for instance the 2017 M_W 8.2

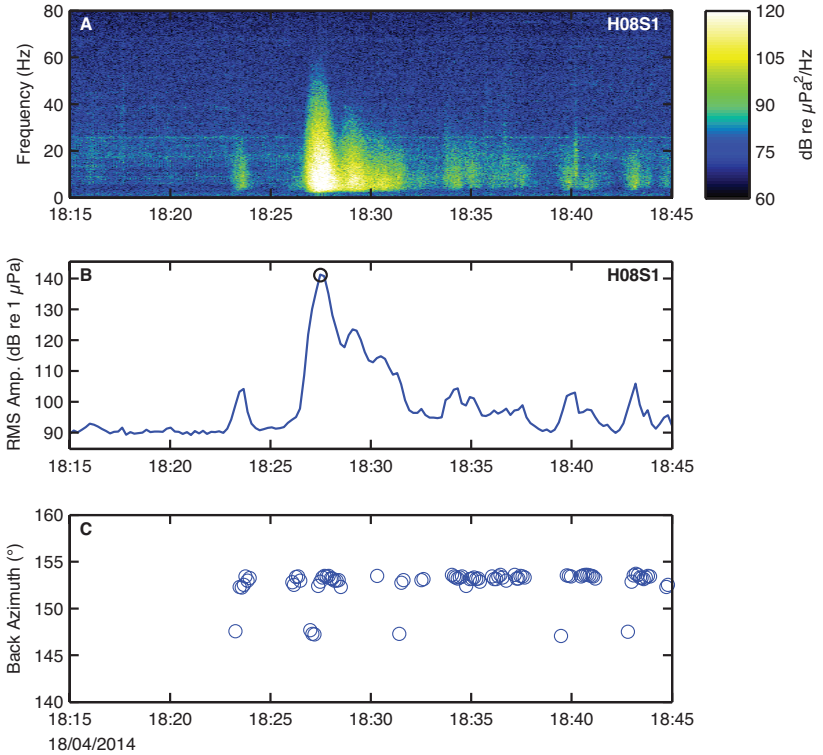

Figure 5.3: Hydroacoustic observations of the 2014 Papanoa earthquake. (a) Single receiver spectrogram of the H08S1 hydrophone data, beginning at 18:15 UTC 18 April 2014. A 1 Hz high-pass filter is applied to minimize background noise levels. (b) Root-mean-square (RMS) amplitudes calculated over 12-sec windows with 50% overlap in the 2-20 Hz frequency band. (c) Back azimuths of 12-sec detections during the 30 min period, averaging at 153.1 ± 0.7° (two standard deviations uncertainty). The timing of the maximum RMS amplitude (black circle) is consistent to within 4 sec of the designated arrival time of the M_W 7.3 main shock at 18:27:32 UTC, assuming a mean propagation speed of 1482 m/s along the source-receiver path.

Chiapas earthquake (Ye et al., 2017). Direct geodesic routes between these events and the H08S hydrophones are blocked by the New Zealand and Australian mainland, yet low-frequency arrivals similar to the one of the 2014 Papanoa earthquake can be recorded. Potential factors that may enable the transmission of low-frequency sound despite the obstructed source-receiver paths include, amongst others, the left-lateral, i.e. southbound, deflection of acoustic phases due to the horizontal sound speed gradients present at southern latitudes, in particular within the Antarctic Circumpolar Current, as well as the refraction, and partial or total reflection of acoustic energy at bathymetric obstacles (Munk and Zachariasen, 1991), for example at steeply sloped islands and seamounts in the South Pacific Ocean or the Antarctic continental margin. Neither of the aforementioned factors have been studied extensively in the past. Future investigations will, therefore, focus on a more detailed analysis of the ray path geometry between seismic sources along the Cocos-North America subduction zone and the IMS station at Diego Garcia and attempt to reconcile hydroacoustic observations with results from long-range propagation modeling (e.g., Dushaw and Menemenlis, 2014). Similar to the work presented in the previous chapters, it may further be possible to relate acoustic and body wave magnitude of seismic events to derive the detection threshold of the H08S array for such suprapodal arrivals.

Appendix A

Appendices of Chapter 3

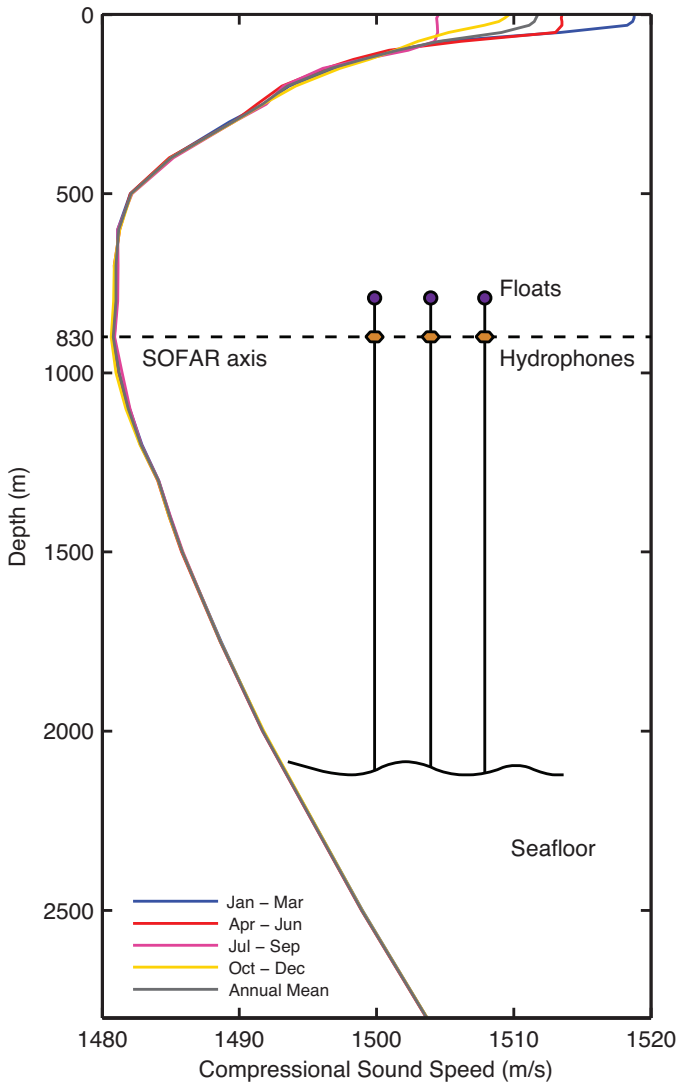

Figure A.1: Sound speed profile at H03S and schematic outline of the IMS hydrophone triplet array. Instruments are bottom-moored at a water depth of approximately 830 m, which corresponds to the depth of the SOFAR channel axis. Water column data taken from the 2005 World Ocean Atlas suggests a mean annual sound speed of 1481 m/s at the depth of the hydrophones, with less than 0.2 m/s seasonal variation throughout the year.

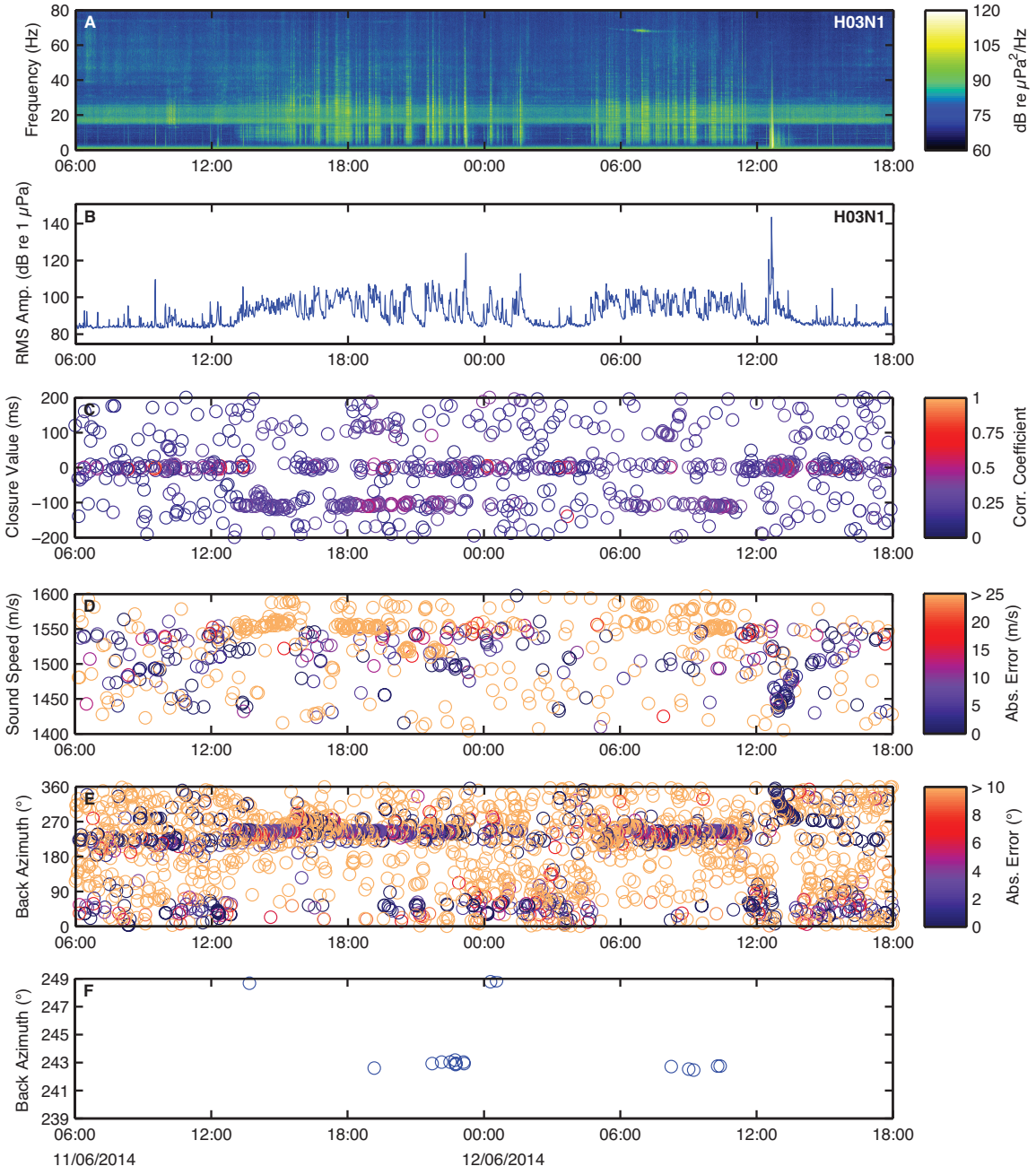

Figure A.2: 36 hours of hydroacoustic data recorded at the H03N array, beginning at 06:00 UTC 11 June 2014. The same processing parameters apply as in Figure 3.3. (a-b) Activity at Monowai is still recognizable in all subfigures, but appears attenuated across all frequencies and by 5-10 dB re 1 μPa in the 4-12 Hz processing band. (c-e) Arrivals are less numerous and show lower phase coherency than at the southern array. (f) Less than a dozen 1-min windows remain within the defined thresholds, i.e. $cc > 0.3$, $cl < |48|ms$, and a sound speed range of 1431-1531 m/s, thus rendering the data impractical for the detection and long-term tracking of activity at the volcano.

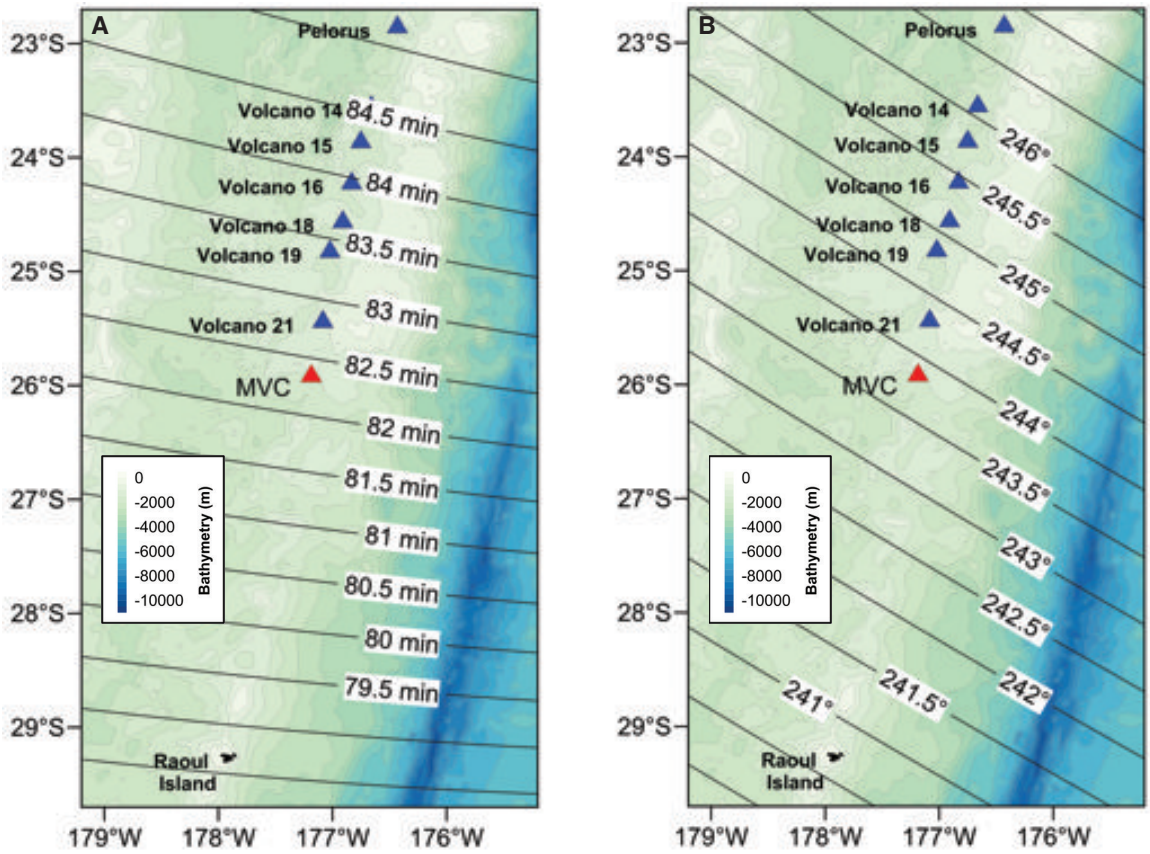

Figure A.3: Relative travel time differences (a) and back azimuths (b) for acoustic source locations in the central Tonga-Kermadec Arc and receiving sensors at Rarotonga and the southern IMS hydrophone array at Juan Fernández Islands. The propagation speed is fixed at 1480 m/s (cf. Munk and Forbes, 1989). Calculations are carried out at an equidistant grid spacing of 0.02°. Triangles mark the positions of the Monowai Volcanic Center (MVC, red) and known hydrothermally active sites (blue) along the central Tonga-Kermadec Arc (Massoth et al., 2007).

Out of all reported sites, the combination of a travel time difference of 82 min and a back azimuth of 243.8° at the H03S array is unique to an acoustic source located at Monowai. The next closest site, Volcano 21, is located within the 82-min band, but at a distinctly different back azimuth relative to the H03S array (244.3°). We note that the geodesic offset of 0.5° is greater than the two standard deviation uncertainty (± 0.3°) of all 1-min detections associated with activity at Monowai during the time of this study. Signals from Volcano 21 traveling in the SOFAR channel are likely to be blocked by the Kermadec Ridge, which shoals to depths of less than 500 m east of the edifice. Furthermore, ROV dives conducted as part of the 2007 expedition aboard R/V SONNE (SO192-2, Schwarz-Schampera et al., 2007) showed no signs of recent eruptive activity at Volcano 21. It is therefore reasonable to assume that volcanic episodes identified by the approach outlined in Chapter 3, and accordingly in Chapter 2, indeed occurred at Monowai.

No.	Start time (UTC)	End time (UTC)	Duration (days)	Number of Detections	RMS Level (re 1 μPa)
1	2003-07-13 14:41	2003-07-23 19:43	10.21	9289	100.36
2	2003-08-07 03:52	2003-08-09 16:09	2.51	3186	102.55
3	2003-09-09 23:32	2003-09-11 03:12	1.15	629	107.38
4	2003-09-18 19:34	2003-09-21 18:26	2.95	3691	108.38
5	2003-09-29 06:17	2003-10-02 13:24	3.30	3111	104.71
6	2003-10-05 16:21	2003-10-06 23:48	1.31	1483	106.85
7	2003-10-25 15:10	2003-10-30 12:06	4.87	4029	98.37
8	2003-11-07 18:23	2003-11-10 17:34	2.97	2965	97.62
9	2003-11-13 15:04	2003-11-15 19:41	2.19	624	98.96
10	2003-11-21 00:58	2003-11-24 14:44	3.57	1528	101.14
11	2003-11-25 05:12	2003-11-26 00:23	0.80	340	98.99
12	2003-12-05 17:19	2003-12-13 14:54	7.90	7861	96.70
13	2003-12-14 03:26	2003-12-15 02:26	0.96	92	92.71
14	2004-01-25 22:30	2004-01-27 13:55	1.64	1526	101.16
15	2004-02-17 23:56	2004-02-19 08:46	1.37	1368	105.49
16	2004-02-23 00:05*	2004-03-02 13:50	8.57	8116	99.31
17	2014-04-23 00:03*	2014-05-01 06:55	8.29	8709	100.46
18	2014-05-07 00:27	2014-05-08 09:08	1.36	1289	100.72
19	2014-05-13 03:06	2014-05-14 03:59	1.04	984	99.51
20	2014-05-20 10:39	2014-05-21 12:07	1.06	489	98.74
21	2014-05-26 04:02	2014-05-26 16:28	0.52	292	104.63
22	2014-05-31 22:56	2014-06-01 05:39	0.28	141	103.04
23	2014-06-05 03:47	2014-06-05 09:30	0.24	96	98.99
24	2014-06-07 05:49	2014-06-08 01:35	0.82	379	102.28

Table A.1 continued from previous page

No.	Start time (UTC)	End time (UTC)	Duration (days)	Number of Detections	RMS Level (re 1 μPa)
25	2014-06-11 13:01	2014-06-12 11:28	0.94	801	105.53
26	2014-07-04 10:50	2014-07-05 08:42	0.91	598	101.05
27	2014-07-13 07:49	2014-07-14 02:02	0.76	225	93.28
28	2014-07-20 04:47	2014-07-27 05:43	7.04	7924	94.88
29	2014-08-02 14:27	2014-08-04 19:57	2.23	1876	91.77
30	2014-08-12 09:59	2014-08-15 06:14	2.84	1786	91.84
31	2014-08-18 00:19	2014-08-19 20:36	1.85	211	87.98
32	2014-09-05 05:54	2014-09-05 23:19	0.73	316	101.8
33	2014-10-15 15:39	2014-10-22 02:30	6.45	8820	99.12
34	2014-10-22 14:45	2014-10-27 07:19	4.69	5997	98.52
35	2014-10-30 00:20**	2014-11-08 22:23	9.92	12144	94.56
36	2014-11-11 03:07	2014-11-11 19:04	0.66	901	94.99
37	2015-01-09 09:30	2015-01-11 01:03	1.65	1672	100.45
38	2015-01-12 02:12	2015-01-17 12:28	5.43	3652	98.43
39	2015-01-20 23:53	2015-01-22 11:27	1.48	128	96.16
40	2015-01-25 08:27	2015-01-27 06:27	1.92	1241	96.56
41	2015-01-31 15:25	2015-02-01 16:58	1.06	1053	98.06
42	2015-03-06 01:52	2015-03-09 15:20	3.56	1736	99.29
43	2015-03-15 22:40	2015-03-20 00:31	4.08	1124	103.36
44	2015-05-03 19:10	2015-05-17 05:40	13.44	8937	97.52
45	2015-06-06 15:00	2015-06-15 05:46	8.62	7733	97.48
46	2015-06-15 22:41	2015-06-17 00:16	1.07	1364	101.51
47	2015-06-18 11:45	2015-06-24 00:53	5.55	3814	93.78

Table A.1 continued from previous page

No.	Start time (UTC)	End time (UTC)	Duration (days)	Number of Detections	RMS Level (re 1 μPa)
48	2015-07-22 16:42	2015-07-25 22:10	3.23	3007	97.95
49	2015-08-14 15:07	2015-08-23 14:09	8.96	8365	97.01
50	2015-08-28 15:44	2015-08-30 18:44	2.13	1995	103.23
51	2015-09-17 18:05	2015-09-19 05:29	1.48	786	100.1
52	2015-10-12 09:33	2015-10-16 14:44	4.22	2572	99.91
53	2015-10-17 01:43	2015-10-18 06:15	1.19	482	91.85
54	2015-10-26 23:25	2015-10-31 10:57	4.48	1327	90.45
55	2015-11-10 20:12	2015-11-14 06:30	3.43	2270	92.89
56	2015-11-15 14:01	2015-11-21 14:30	6.02	4761	92.02
57	2015-11-28 09:54	2015-11-29 20:51	1.46	619	94.35
58	2015-12-30 10:36	2015-12-31 20:29	1.41	1103	98.48
59	2016-01-01 16:42	2016-01-02 22:12	1.23	959	102.35
60	2016-01-06 10:34	2016-01-07 12:09	1.07	579	102.49
61	2016-02-02 05:19	2016-02-03 17:04	1.49	87	102.04
62	2016-02-07 12:58	2016-02-08 18:44	1.24	579	102.79
63	2016-02-14 12:54	2016-02-18 15:16	4.10	3168	101.88
64	2016-02-22 11:11	2016-02-25 07:35	2.85	1911	97.53
65	2016-02-26 05:15	2016-02-27 19:08	1.58	1310	102.76
66	2016-03-04 17:05	2016-03-07 13:23	2.85	2455	100.40
67	2016-03-11 15:00	2016-03-13 23:42	2.36	928	99.65
68	2016-03-18 16:13	2016-03-19 07:19	0.63	476	104.61
69	2016-03-28 23:11	2016-03-29 09:46	0.44	503	104.53
70	2016-04-02 08:59	2016-04-03 23:29	1.60	1596	102.05

Table A.1 continued from previous page

No.	Start time (UTC)	End time (UTC)	Duration (days)	Number of Detections	RMS Level (re 1 μPa)
71	2016-04-09 16:32	2016-04-11 01:53	1.39	1146	105.35
72	2016-04-16 11:32	2016-04-19 17:37	3.25	662	93.79
73	2016-05-13 12:40**	2016-05-19 07:28	5.78	4282	94.76
74	2016-07-01 04:42	2016-07-03 20:13	2.65	1440	92.86
75	2016-07-10 00:12	2016-07-12 03:42	2.15	1730	97.38
76	2016-07-13 07:14	2016-07-13 20:14	0.54	394	97.44
77	2016-08-31 15:23	2016-09-05 16:08	5.03	3871	95.88
78	2016-09-28 13:44	2016-09-30 21:59	2.34	362	89.77
79	2016-10-11 19:13	2016-10-13 22:18	2.13	1381	95.03
80	2016-11-10 16:34	2016-11-11 18:16	1.07	1482	103.95
81	2016-12-05 07:35	2016-12-06 19:00	1.48	310	92.63
82	2017-01-10 13:45	2017-01-13 08:26	2.78	1781	95.16

Table A.1: Activity at Monowai, as identified by density-based clustering of 1-min detections in the record of the H03S hydrophone array. The data set comprises 82 volcanic episodes between 10 July 2003 and 25 March 2004, and from 23 April 2014 to 31 January 2017. The search radius of the DBSCAN algorithm is set to 12 hours and 0.5°. Start times could not be derived for two episodes in February 2004 and April 2014 due to missing data (marked by a single asterisk). In all other cases, the start and end times correspond to the first and last detection of the respective cluster. Observations of discolored water and pumice rafts near the location of Monowai (Global Volcanism Program, 2017a) coincide to the day with two episodes identified in October 2014 and May 2016 (marked by a double asterisk).

Latitude (°S)	Longitude (°W)	Depth (km)	Magnitude (m_b)	Acoustic Amplitude (re 1 μPa)	Duration (sec)
28.75	177.46	58.45	3.44	127.20	48.1
27.64	177.65	76.89	3.63	121.13	41.8
27.54	176.60	55.22	3.66	119.78	21.9
29.80	177.51	40.09	4.63	131.25	132.0
28.07	177.26	68.15	3.59	117.74	55.3
25.58	177.00	61.10	3.73	117.70	49.0
28.30	177.15	37.71	3.55	118.25	42.8
28.86	177.12	52.66	3.96	120.69	55.5
27.47	176.94	58.39	4.30	127.13	89.3
29.13	177.25	43.56	3.59	117.60	9.4
29.33	177.44	53.42	3.77	122.48	40.9
28.86	177.53	42.82	3.34	116.89	18.6
29.37	177.32	55.10	3.80	127.44	57.5
24.72	176.09	55.52	3.73	113.59	21.8
30.23	177.92	44.02	5.00	140.94	156.9
28.82	177.43	59.58	5.03	142.71	140.7
27.69	177.22	70.95	3.83	119.35	66.6
30.10	177.91	64.41	3.83	117.31	21.9
30.11	177.99	56.06	4.73	134.33	32.4
27.74	177.03	50.92	4.70	133.85	164.8
30.11	177.90	66.14	3.97	122.16	21.5
28.02	177.24	71.94	3.56	119.67	45.5
30.13	177.85	42.81	4.81	140.76	78.8
26.28	177.36	51.86	3.54	114.65	45.4
29.61	177.62	43.02	4.16	131.49	49.1
28.61	177.30	40.63	4.33	130.24	101.0
29.12	177.13	56.84	3.46	103.99	12.6
28.16	177.22	45.81	4.94	137.10	138.2

Table A.2: 28 earthquakes detected by IMS seismic stations and hydrophone H03S1 at Juan Fernández Islands during the time of the study presented in Chapter 3, i.e. from 10 July 2003 to 25 March 2004, and between 23 April 2014 and 31 January 2017. The data set is limited to events with focal depths of up to 80 km, located at distances similar to the source-receiver range between Monowai and the H03S array, i.e. 9050 ± 120 km. The mean length of arrivals received at H03S1 is 63 seconds. In the vDEC database, the following tables of the Reviewed Event Bulletin were used in the extraction process: *arrival*, *assoc*, and *origin*. Corresponding acoustic amplitudes are taken from the *hydrofeatures* table of the final Standard Event List (SEL3).

Appendix B

Appendices of Chapter 4

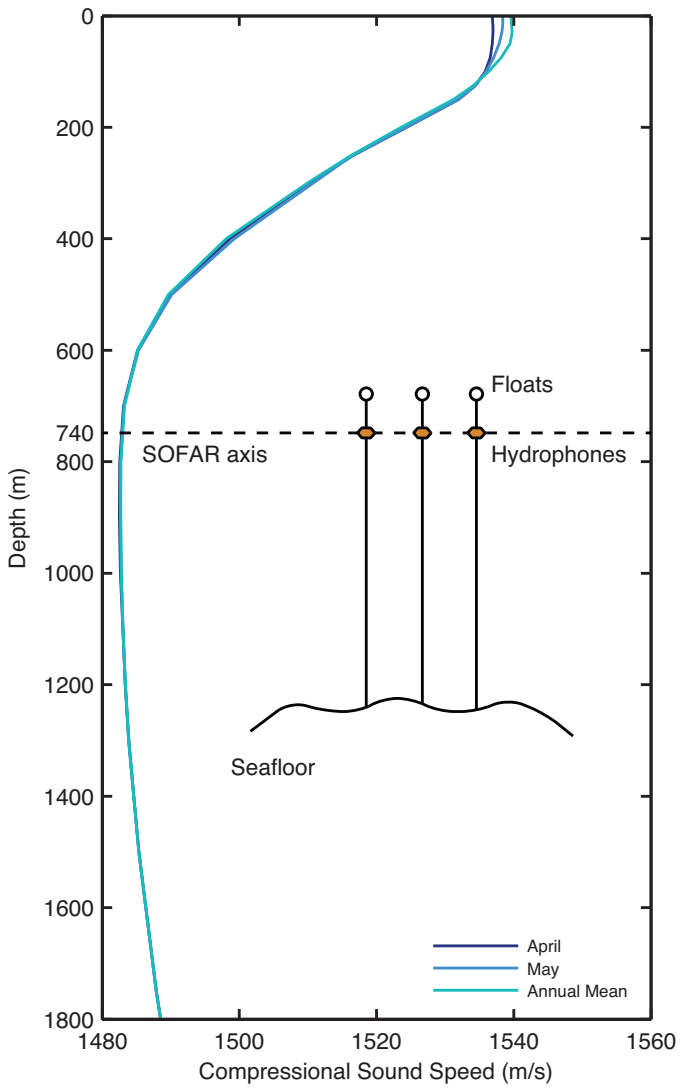

Figure B.1: Vertical sound speed profiles at H11S and schematic outline of the triplet array. The average mooring depth of the three hydrophones is 740 ± 12 m. The compressional sound speed is about 1482 m/s near the SOFAR channel axis, with little monthly variation below 100 m. Water column data is taken from the 2005 World Ocean Atlas.

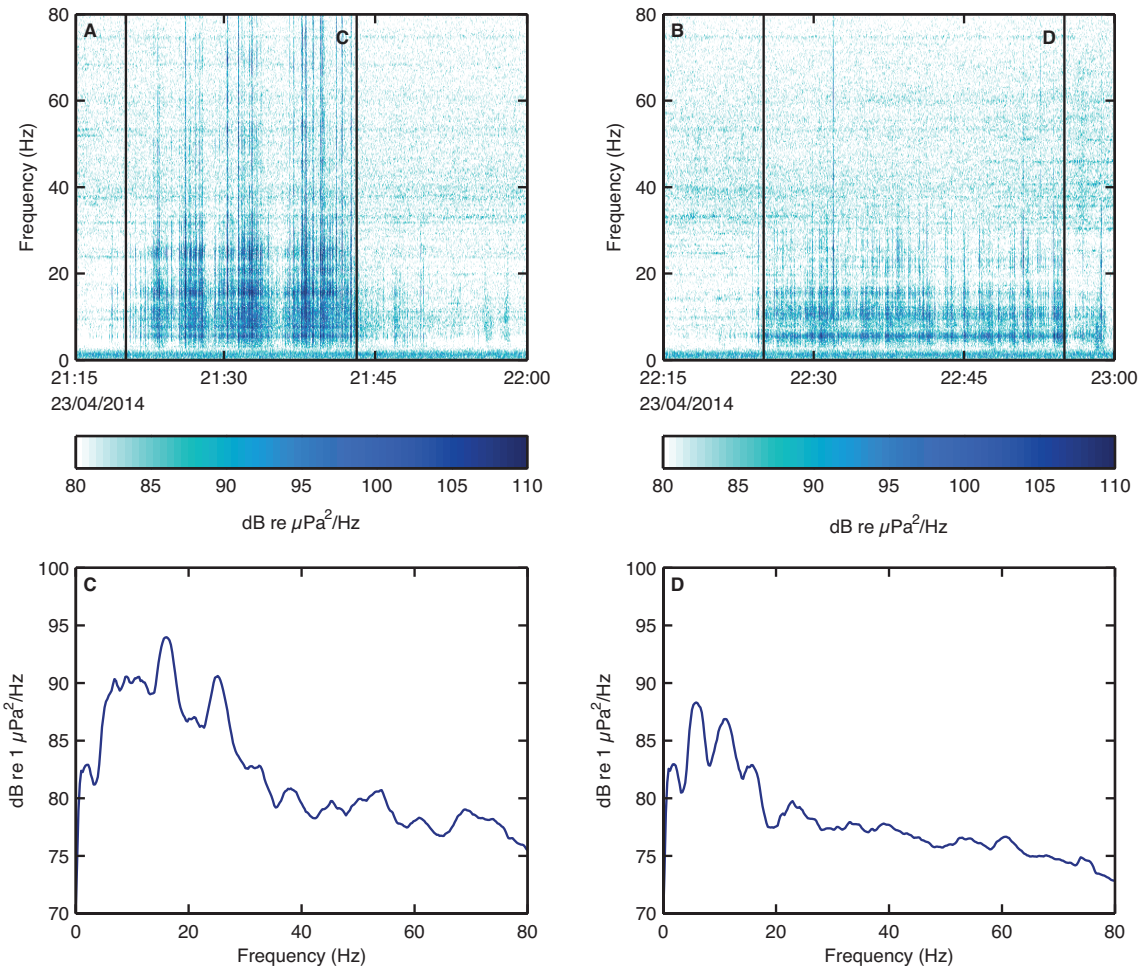

Figure B.2: Spectral investigation of presumed tremor events of the 2014 eruption at Ahyi. Single receiver spectrograms of data recorded at the H11S1 hydrophone, beginning at (a) 21:15 UTC and (b) at 22:15 UTC 23 April 2014. A 1 Hz high-pass filter is applied to minimize background noise levels. (c and d) Corresponding power spectral density (PSD) of segments highlighted in the spectrograms (black lines). Fourier transforms are averaged over 4-sec windows with 50% overlap. The earlier event exhibits a broadband distribution of energy between 5 and 30 Hz, with notable peaks at 16 and 25 Hz. A fundamental of 6 Hz, with overtones at 12, 18, and possibly 24 Hz, is clearly distinguishable during the second event, i.e. between 22:25 and 22:55 UTC.

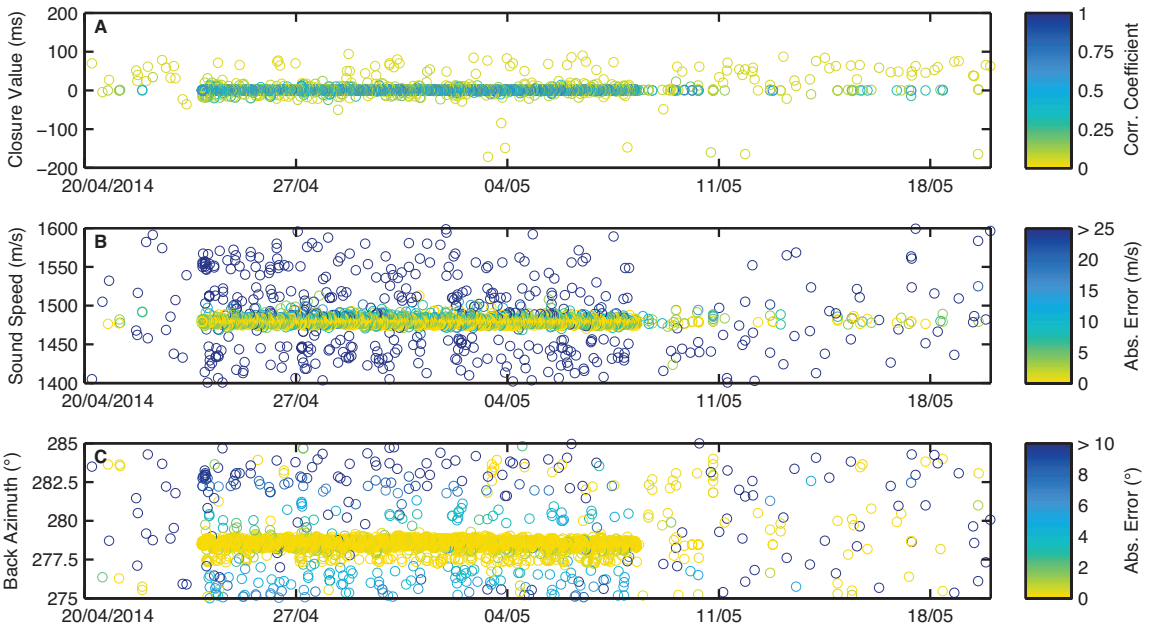

Figure B.3: Parameters of the plane wave fitting routine used to derive the signal back azimuth of 1-min windows recorded at IMS array H11S between 20 April and 20 May 2014. Processing results are shown in the form of (a) closure value and mean correlation coefficient between the three hydrophone pairs, (b) apparent sound speed across the array, and (c) back azimuth. Acoustic phases associated with the eruption at Ahyi arrive from 23 April onwards, accompanied by a distinct increase in signal coherence, i.e. a positive shift in correlation coefficients to above 0.3 and closure values typically below 15 ms. During the 15 days long main burst, detections stabilize at an average of 1479 m/s and a back azimuth of 278.5°, which indicates that the received signal travels in the deep sound channel and arrives from within half a degree of the geodesic angle of arrival between the hydrophone array and the volcano (278.9°). Error estimates of the inversion are given at two standard deviation uncertainties.

Latitude (°N)	Longitude (°E)	Depth (km)	Magnitude (m_b)	Acoustic Amplitude (re 1 μPa)	Duration (sec)
18.78	147.31	49.45	3.32	113.42	40.9
18.67	146.35	69.10	5.23	146.94	40.8
18.75	146.98	57.28	3.95	120.81	66.5
17.93	147.07	28.47	4.69	126.21	79.3
17.89	146.92	54.76	4.35	124.33	63.7
18.63	146.86	71.45	3.49	109.84	51.2
20.21	146.82	57.87	3.68	119.14	42.4
20.89	144.66	59.51	3.51	119.43	45.0
18.60	146.76	72.72	3.55	114.19	46.4
17.92	147.15	51.95	3.44	111.70	40.3
19.38	146.00	72.46	4.26	136.20	79.1
18.90	146.85	45.79	4.35	126.00	65.8
18.84	146.85	70.50	3.78	115.85	42.5

Table B.1: 13 earthquakes detected by IMS seismic stations and hydrophone H11S1 at Wake Island between 1 January 2012 and 31 December 2016. The data set is limited to events located at a source-receiver distance of 2283 ± 250 km from the H11S array, with a focal depth of less than 80 km, and between 40 and 80 seconds in arrival length. In the vDEC database, the following tables of the Reviewed Event Bulletin were used in the extraction process: *arrival*, *assoc*, and *origin*. Acoustic amplitudes are taken from the *hydrofeatures* table of the final Standard Event List (SEL3).

Appendix C

Appendices of Chapter 5

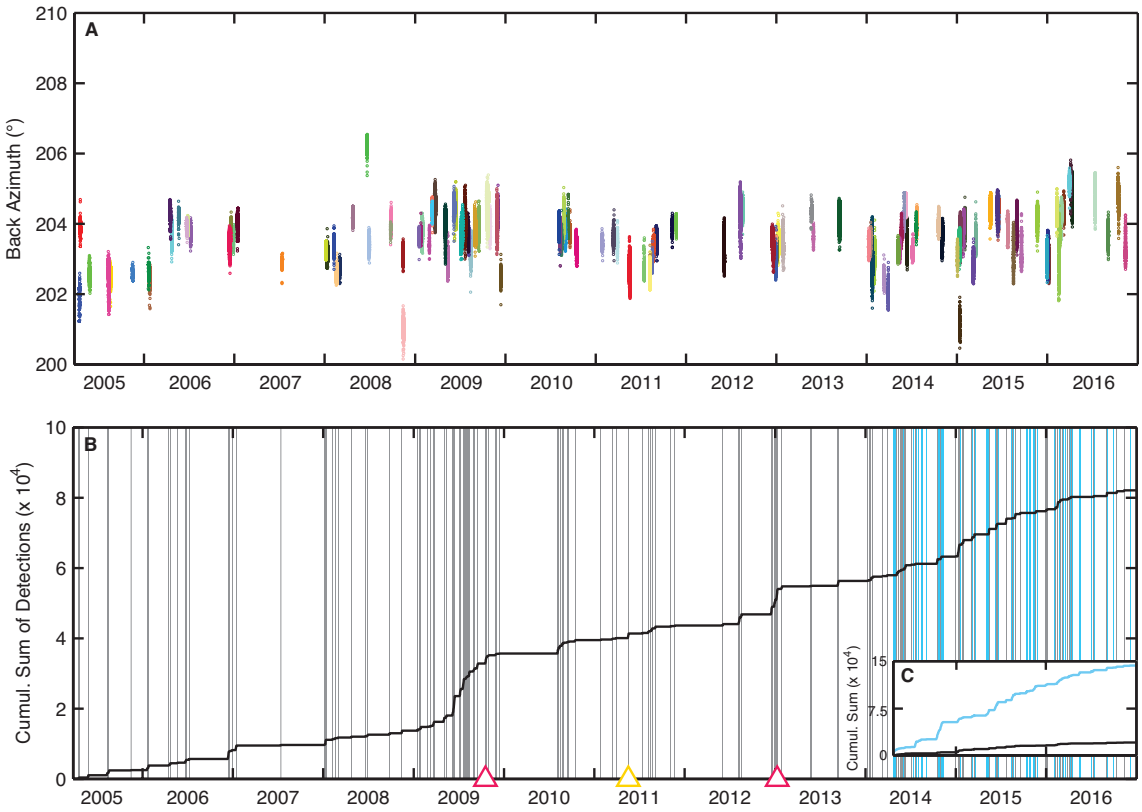

Figure C.1: Volcanic activity at Monowai between 23 March 2005 and 31 December 2016, recorded at IMS array H10N, Ascension Island. (a) Results of the DBSCAN algorithm, using the same parameter settings as for data recorded at H03S (see Chapter 3.2 to and 3.3). A total of 135 clusters are identified in the record. (b) Cumulative sum of 82,070 clustered 1-min detections (black line). Grey shaded areas correspond to episodes recorded at H10N, as shown in (a). Blue shaded areas indicate episodes recorded at H03S (cf. Figure 3.5f in Chapter 3). The blue triangle marks the positions of the May 2011 eruption discussed in Chapter 2. In two cases, onsite observations of discolored surface water (27 October 2009, Global Volcanism Program, 2017a) and acoustic shockwaves (1 January 2013, Werner et al., 2013) at Monowai coincide with volcanic episodes (red triangles). (c) Cumulative sum of clustered 1-min detections at H10N and H03S between 23 April 2014 and 31 December 2016, i.e. when data from both stations is available. A total of 144,717 detections are made at H03S (blue line), in contrast to 24,159 at H10N (black line).

Out of 64 episodes identified at H03S, 43 are retrieved in the record of the Ascension Island array. The number of detections per episode is between 1.1 and 81 times lower than at H03S, resulting in six times fewer arrivals registered over the course of the 2.5 years. Notably, we observe more than twice as many detections at H03S during its time of operation (∼3.5 years) than over the entire length of the 12-year record at H10N. We conclude that tracking volcanic activity at Monowai in the data set of IMS station H10 is possible, but does not provide the same resolution as recordings of the 'proximate' hydrophone array at Juan Fernández Islands.

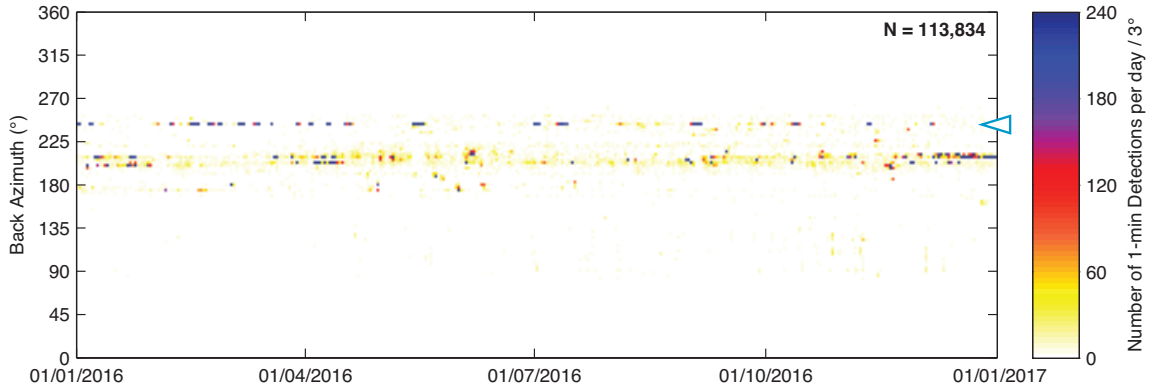

Figure C.2: Distribution of 1-min detections recorded at the southern hydrophone array of IMS station H03, Juan Fernández Islands, for the year 2016. Detection thresholds are set in accordance with previous studies, thus limiting the data set to arrivals with a sound speed of 1400-1600 m/s across the array, a cross-correlation coefficient of 0.3, and a closure value of |48| ms. Data is band-pass filtered at 4-12 Hz. A total of 113,834 arrivals are registered over the course of the year, 28% of which are associated with volcanic activity at Monowai as defined in Chapter 3 (cf. Figure 3.5). The blue and white filled triangle marks the geodesic back azimuth of 243.8° between the array and the volcano. The majority of the remaining detections arrive from a southwestern direction (190-220°), most likely corresponding to ice-generated noise at southern latitudes, for example in the western Amundsen Sea and a region north of the Ross Ice Shelf (cf. Talandier et al., 2006).

Appendix D

Station List

Network	Station	Location	Latitude (°S)	Longitude (°W)	Elevation (m)	Sampling Rate (Hz)
G	PPTF	00	17.58	149.56	705	20
G	TAOE	00	8.85	140.14	800	50
IU	RAR	00	21.21	159.77	28	20
IU	RAR	10	21.21	159.77	28	40
RSP	TVO	00	17.79	149.24	1080	20

Table D.1: List of seismic stations referred to throughout this thesis. Data gathered by seismometers affiliated with the Geophone (G) and Global Seismograph Network (IU) initiatives can be accessed via web services maintained by the Incorporated Research Institutions for Seismology (IRIS). Times of T phase arrivals, detected at station TVO of the Polynesian Seismic Network (RSP) and presented in Chadwick et al. (2008b), were made available by Bill Chadwick (Oregon State/NOAA), Olivier Hyvernaud, and Dominique Reymond (both Laboratoire de Géophysique Tahiti).

Array	Element	Latitude (°S)	Longitude (°W)	Mooring Depth (m bsl)	Sampling Rate (Hz)	Ondate	Offdate
H03N	H03N1	33.4412	78.9120	757	250	09/07/2003	13/07/2007
H03N	H03N2	33.4399	78.9324	757	250	09/07/2003	13/07/2007
H03N	H03N3	33.4556	78.9240	761	250	09/07/2003	13/07/2007
H03N	H03N1	33.4412	78.9120	757	250	14/07/2007	27/02/2010
H03N	H03N2	33.4399	78.9324	757	250	14/07/2007	27/02/2010
H03N	H03N3	33.4556	78.9240	761	250	14/07/2007	27/02/2010
H03N	H03N1	33.45802	78.93414	813	250	23/04/2014	online
H03N	H03N2	33.44672	78.94971	825	250	23/04/2014	online
H03N	H03N3	33.44161	78.92908	835	250	23/04/2014	online
H03S	H03S1	33.8437	78.9058	752	250	09/07/2003	25/03/2004
H03S	H03S2	33.8370	78.9262	750	250	09/07/2003	25/03/2004
H03S	H03S3	33.8258	78.9095	754	250	09/07/2003	25/03/2004
H03S	H03S1	33.81818	78.83534	832	250	23/04/2014	online
H03S	H03S2	33.83378	78.84616	816	250	23/04/2014	online
H03S	H03S3	33.81816	78.85694	835	250	23/04/2014	online

Table D.2: List of hydrophone array elements deployed at IMS station H03, Juan Fernández Islands. Mooring depth is given in meters below sea level (m bsl). Sensor positions of the northern array (H03N) were re-calibrated in 2007. Note that the column 'Ondate' refers to the day of station certification, i.e. when recordings become available in the vDEC database, rather than the time of installation.

Array	Element	Latitude (°S)	Longitude (°W)	Mooring Depth (m bsl)	Sampling Rate (Hz)	Ondate	Offdate
H10N	H10N1	7.8457	14.4802	847	250	25/03/2005	13/07/2007
H10N	H10N2	7.8277	14.4872	845	250	25/03/2005	05/03/2006
H10N	H10N3	7.8415	14.5015	850	250	25/03/2005	05/03/2006
H10N	H10N1	7.8457	14.4802	847	250	14/07/2007	online
H10N	H10N2	7.8278	14.4875	845	250	06/03/2006	online
H10N	H10N3	7.8409	14.5017	850	250	06/03/2006	online
H10S	H10S1	8.9412	14.6484	865	250	25/03/2005	13/07/2007
H10S	H10S2	8.9597	14.6447	852	250	25/03/2005	05/03/2006
H10S	H10S3	8.9530	14.6627	863	250	25/03/2005	05/03/2006
H10S	H10S1	8.9412	14.6484	865	250	14/07/2007	n/a
H10S	H10S2	8.9591	14.6453	852	250	06/03/2006	online
H10S	H10S3	8.9527	14.6629	863	250	06/03/2006	online

Table D.3: List of hydrophone array elements deployed at IMS station H10, Ascension Island. Mooring depth is given in meters below sea level (m bsl). Sensor positions of both arrays were re-calibrated in 2006 and 2007. Hydrophone element H10S1 was lost in 2013. Note that the column 'Ondate' refers to the day of station certification, i.e. when recordings become available in the vDEC database, rather than the time of installation.

Array	Element	Latitude (°N)	Longitude (°E)	Mooring Depth (m bsl)	Sampling Rate (Hz)	Ondate	Offdate
H11S	H11S1	18.5083	166.7003	750	250	07/05/2007	08/09/2009
H11S	H11S2	18.4908	166.7050	742	250	07/05/2007	08/09/2009
H11S	H11S3	18.4957	166.6865	726	250	07/05/2007	08/09/2009
H11S	H11S1	18.5083	166.7003	750	250	09/09/2009	online
H11S	H11S2	18.4905	166.7054	742	250	09/09/2009	online
H11S	H11S3	18.4949	166.6873	726	250	09/09/2009	online

Table D.4: List of hydrophone elements of the southern array of IMS station H11, Wake Island. Mooring depth is given in meters below sea level (m bsl). Sensor positions were re-calibrated in 2009. Note that the ondate refers to the day of station certification, i.e. when recordings become available in the vDEC database, rather than the time of installation.

Bibliography

Aki, K. and Koyanagi, R. Deep Volcanic Tremor and Magma Ascent Mechanism Under Kilauea, Hawaii. *J. Geophys. Res.*, 86(NB8):7095–7109, 1981.

Arora, N. S., Russell, S., and Sudderth, E. NET-VISA: Network Processing Vertically Integrated Seismic Analysis. *Bull. Seismol. Soc. Am.*, 103(2A):709–729, 2013.

Assink, J. D., Averbuch, G., Smets, P. S. M., and Evers, L. G. On the infrasound detected from the 2013 and 2016 DPRK's underground nuclear tests. *Geophys. Res. Lett.*, 43(7):3526–3533, 2016.

Baker, E. T., Embley, R. W., Walker, S. L., Resing, J. A., Lupton, J. E., Nakamura, K., de Ronde, C. E. J., and Massoth, G. J. Hydrothermal activity and volcano distribution along the Mariana arc. *J. Geophys. Res.*, 113(B8), 2008.

Bassett, D. and Watts, A. B. Gravity anomalies, crustal structure, and seismicity at subduction zones: 1. Seafloor roughness and subducting relief. *Geochem. Geophys. Geosyst.*, 16(5):1508–1540, 2015.

Battaglia, J. and Aki, K. Location of seismic events and eruptive fissures on the Piton de la Fournaise volcano using seismic amplitudes. *J. Geophys. Res*, 108(B8), 2003.

Becker, A., Wotawa, G., Ringbom, A., and Saey, P. R. J. Backtracking of Noble Gas Measurements Taken in the Aftermath of the Announced October 2006 Event in North Korea by Means of PTS Methods in Nuclear Source Estimation and Reconstruction. *Pure Appl. Geophys.*, 167(4-5):581–599, 2010.

Blackman, D. K., Groot-Hedlin, C. C., Harben, P., Sauter, A., and Orcutt, J. A. Testing low/very low frequency acoustic sources for basin-wide propagation in the Indian Ocean. *J. Acoust. Soc. Am.*, 116(4):2057–2066, 2004.

Bloomer, S. H., Stern, R. J., and Smoot, N. C. Physical Volcanology of the Submarine Mariana and Volcano Arcs. *B. Volcanol.*, 51(3):210–224, May 1989.

Blum, J. W. and Cohen, D. S. Acoustic wave propagation in an underwater sound channel. I. Qualitative theory. *J. Inst. Math. Appl.*, 8:186–198, 1971.

Bohnenstiehl, D. R., Scheip, C. M., Matsumoto, H., and Dziak, R. P. Acoustics variability of air gun signals recorded at intermediate ranges within the Lau Basin. *Geochem. Geophys. Geosyst.*, 13(11), 2012.

Bohnenstiehl, D. R., Dziak, R. P., Matsumoto, H., and Lau, T. K. A. Underwater acoustic records from the March 2009 eruption of Hunga Ha'apai-Hunga Tonga volcano in the Kingdom of Tonga. *J. Volc. Geotherm. Res.*, 249:12–24, 2013.

Bohnenstiehl, D. R., Dziak, R. P., Matsumoto, H., and Conder, J. A. Acoustic response of submarine volcanoes in the Tofua Arc and northern Lau Basin to two great earthquakes. *Geophys. J. Int.*, 196(3):1657–1675, 2014.

Bowers, D., Douglas, A., Selby, N. D., Marshall, P. D., Porter, D., and Wallis, N. J. Seismological identification of the 1998 May 28 Pakistan nuclear test. *Geophys. J. Int.*, 150(1):153–161, 2002.

Bredemeyer, S. and Hansteen, T. H. Synchronous degassing patterns of the neighbouring volcanoes Llaima and Villarrica in south-central Chile: the influence of tidal forces. *Int. J. Earth Sci.*, page 39, 2014.

Bromirski, P. D., Duennebier, F. K., and Stephen, R. A. Mid-ocean microseisms. *Geochem. Geophys. Geosyst.*, 6(4), 2005.

Brown, D., Ceranna, L., Prior, M., Mialle, P., and Le Bras, R. J. The IDC Seismic, Hydroacoustic and Infrasound Global Low and High Noise Models. *Pure Appl. Geophys.*, 171(3-5):361–375, 2012.

Brown, P. G., Assink, J. D., Astiz, L., Blaauw, R., Boslough, M. B., Borovicka, J., Brachet, N., Brown, D., Campbell-Brown, M., Ceranna, L., Cooke, W., de Groot-Hedlin, C., Drob, D. P., Edwards, W., Evers, L. G., Garces, M., Gill, J., Hedlin, M., Kingery, A., Laske, G., Le Pichon, A., Mialle, P., Moser, D. E., Saffer, A., Silber, E., Smets, P., Spalding, R. E., Spurny, P., Tagliaferri, E., Uren, D., Weryk, R. J., Whitaker, R., and Krzeminski, Z. A 500-kiloton airburst over Chelyabinsk and an enhanced hazard from small impactors. *Nature*, 503(7475):238–241, 2013.

Buehler, J. S. and Shearer, P. M. T phase observations in global seismogram stacks. *Geophys. Res. Lett.*, 42(16):6607–6613, 2015.

Burley, J. M. A. and Katz, R. F. Variations in mid-ocean ridge CO2 emissions driven by glacial cycles. *Earth Planet. Sci. Lett.*, 426:246–258, 2015.

Butler, R. Observations of polarized seismoacoustic T waves at and beneath the seafloor in the abyssal Pacific Ocean. *J. Acoust. Soc. Am.*, 120(6):3599–3606, 2006.

Butler, R. and Lomnitz, C. Coupled seismoacoustic modes on the seafloor. *Geophys. Res. Lett.*, 29(10), 2002.

Calkins, J., Oppenheimer, C., and Kyle, P. R. Ground-based thermal imaging of lava lakes at Erebus volcano, Antarctica. *J. Volc. Geotherm. Res.*, 177(3):695–704, 2008.

Cansi, Y. An Automatic Seismic Event Processing for Detection and Location - the Pmcc Method. *Geophys. Res. Lett.*, 22(9):1021–1024, 1995.

Caplan-Auerbach, J., Dziak, R. P., Haxel, J., Bohnenstiehl, D. R., and Garcia, C. Explosive processes during the 2015 eruption of Axial Seamount, as recorded by seafloor hydrophones. *Geochem. Geophys. Geosyst.*, 18(4):1761–1774, 2017.

Chadwick, W. W., Dziak, R. P., Haxel, J. H., Embley, R. W., and Matsumoto, H. Submarine landslide triggered by volcanic eruption recorded by in situ hydrophone. *Geology*, 40(1):51–54, 2012.

Chadwick, W. W. J., Cashman, K. V., Embley, R. W., Matsumoto, H., Dziak, R. P., de Ronde, C. E. J., Lau, T. K. A., Deardorff, N. D., and Merle, S. G. Direct video and hydrophone observations of submarine explosive eruptions at NW Rota-1 volcano, Mariana arc. *J. Geophys. Res.*, 113(B8), 2008a.

Chadwick, W. W. J., Wright, I. C., Schwarz-Schampera, U., Hyvernaud, O., Reymond, D., and de Ronde, C. E. J. Cyclic eruptions and sector collapses at Monowai submarine volcano, Kermadec arc: 1998-2007. *Geochem. Geophys. Geosyst.*, 9(10), 2008b.

Chapman, N. R. and Price, A. Low frequency deep ocean ambient noise trend in the Northeast Pacific Ocean. *J. Acoust. Soc. Am.*, 129(5):E161–E165, 2011.

Chapp, E., Bohnenstiehl, D. R., and Tolstoy, M. Sound-channel observations of ice-generated tremor in the Indian Ocean. *Geochem. Geophys. Geosyst.*, 6(6), 2005.

Chouet, B. A. Long-period volcano seismicity: Its source and use in eruption forecasting. *Nature*, 380(6572):309–316, 1996.

Collins, M. D. A Split-Step Pade Solution for the Parabolic Equation Method. *J. Acoust. Soc. Am.*, 93(4):1736–1742, 1993.

Dars, J. D., Jaupart, C., and Sparks, R. S. J. Distribution of Volcanos in Active Margins. *J. Geophys. Res*, 100(B10):20421–20432, 1995.

Davey, F. J. The Monowai Seamount - an Active Submarine Volcanic Center on the Tonga-Kermadec Ridge. *New Zeal. J. Geol. Geop.*, 23(4):533–536, 1980.

de Groot-Hedlin, C., Blackman, D. K., and Jenkins, C. S. Effects of variability associated with the Antarctic circumpolar current on sound propagation in the ocean. *Geophys. J. Int.*, 176(2):478–490, 2009.

de Ronde, C. E. J., Baker, E. T., Massoth, G. J., Lupton, J. E., Wright, I. C., Feely, R. A., and Greene, R. R. Intra-oceanic subduction-related hydrothermal venting, Kermadec volcanic arc, New Zealand. *Earth Planet. Sci. Lett.*, 193(3-4):359–369, 2001.

Del Pezzo, E. and Giudicepietro, F. Plane wave fitting method for a plane, small aperture, short period seismic array: a MATHCAD program. *Comput. Geosci.*, 28 (1):59–64, 2002.

Denham, R. N. and Kibblewhite, A. C. Sound-Velocity Structure of South Pacific Ocean. *New Zeal. J. Geol. Geop.*, 13(1):39–&, 1970.

Dushaw, B. D. and Menemenlis, D. Antipodal acoustic thermometry: 1960, 2004. *Deep-Sea Research I: Oceanography*, 86:1–20, 2014.

Dziak, R. P. and Fox, C. G. Evidence of harmonic tremor from a submarine volcano detected across the Pacific Ocean basin. *J. Geophys. Res*, 107(B5), 2002.

Dziak, R. P., Fox, C. G., Embley, R. W., Lupton, J. E., Johnson, G. C., Chadwick, W. W., and Koski, R. A. Detection of and response to a probable volcanogenic T-wave event swarm on the western Blanco Transform Fault Zone. *Geophys. Res. Lett.*, 23(8):873–876, 1996.

Dziak, R. P., Park, M., Matsumoto, H., and Byun, S. K. Hydroacoustic records and a numerical model of the source mechanism from the first historical eruption of Anatahan Volcano, Mariana Islands. *J. Volc. Geotherm. Res.*, 146(1-3):86–101, 2005.

Dziak, R. P., Haxel, J. H., Matsumoto, H., Lau, T. K. A., Merle, S. G., de Ronde, C. E. J., Embley, R. W., and Mellinger, D. K. Observations of regional seismicity and local harmonic tremor at Brothers volcano, south Kermadec arc, using an ocean bottom hydrophone array. *J. Geophys. Res.*, 113(B8):B08S04, 2008.

Dziak, R. P., Hammond, S. R., and Fox, C. G. A 20-Year Hydroacoustic Time Series of Seismic and Volcanic Events in the Northeast Pacific Ocean. *Oceanography*, 24 (3):280–293, 2011.

Dziak, R. P., Bohnenstiehl, D. R., Baker, E. T., Matsumoto, H., Caplan-Auerbach, J., Embley, R. W., Merle, S. G., Walker, S. L., Lau, T. K. A., and Chadwick, W. W. J. Long-term explosive degassing and debris flow activity at West Mata submarine volcano. *Geophys. Res. Lett.*, 42(5):1480–1487, 2015.

Embley, R. W., Chadwick, W. W., Baker, E. T., Butterfield, D. A., Resing, J. A., de Ronde, C. E. J., Tunnicliffe, V., Lupton, J. E., Juniper, S. K., Rubin, K. H., Stern, R. J., Lebon, G. T., Nakamura, K., Merle, S. G., Hein, J. R., Wiens, D. A., and Tamura, Y. Long-term eruptive activity at a submarine arc volcano. *Nature*, 441(7092):494–497, 2006.

Ester, M., Kriegel, H. P., Sander, J., and Xu, X. A Density-Based Algorithm for Discovering Clusters in Large Spatial Databases with Noise. *Proceedings of the Second International Conference on Knowledge Discovery and Data Mining*, pages 226–231, 1996.

Evers, L. G. and Snellen, M. Passive probing of the sound fixing and ranging channel with hydro-acoustic observations from ridge earthquakes. *J. Acoust. Soc. Am.*, 137 (4):2124–2136, 2015.

Evers, L. G., Green, D. N., Young, N. W., and Snellen, M. Remote hydroacoustic sensing of large icebergs in the southern Indian Ocean: Implications for iceberg monitoring. *Geophys. Res. Lett.*, 40(17):4694–4699, 2013.

Evers, L. G., Brown, D., Heaney, K. D., Assink, J. D., Smets, P. S. M., and Snellen, M. Evanescent wave coupling in a geophysical system: Airborne acoustic signals from the Mw 8.1 Macquarie Ridge earthquake. *Geophys. Res. Lett.*, 41(5):1644–1650, 2014.

Evers, L. G., Wapenaar, K., Heaney, K. D., and Snellen, M. Deep ocean sound speed characteristics passively derived from the ambient acoustic noise field. *Geophys. J. Int.*, 210(1):27–33, 2017.

Ewing, M., Press, F., and Worzel, J. L. Further Observations of the T-Phase. *Geol. Soc. Am. Bull.*, 62(12):1527–1527, 1951.

Fee, D., Steffke, A., and Garces, M. Characterization of the 2008 Kasatochi and Okmok eruptions using remote infrasound arrays. *J. Geophys. Res*, 115(9), 2010.

Fornari, D. J., Ryan, W. B. F., and Fox, P. J. The evolution of craters and calderas on young seamounts: Insights from SEA MARC I and Sea beam sonar surveys of a small seamount group near the axis of the East Pacific Rise at 10°N. *J. Geophys. Res*, 89(B13):11069–11083, 1984.

Fox, C. G., Matsumoto, H., and Lau, T. K. A. Monitoring Pacific Ocean seismicity from an autonomous hydrophone array. *J. Geophys. Res*, 106(B3):4183–4206, 2001.

Fritz, H. M., Petroff, C. M., Catalan, P. A., Cienfuegos, R., Winckler, P., Kalligeris, N., Weiss, R., Barrientos, S. E., Meneses, G., Valderas-Bermejo, C., Ebeling, C., Papadopoulos, A., Contreras, M., Almar, R., Carlos Dominguez, J., and Synolakis, C. E. Field Survey of the 27 February 2010 Chile Tsunami. *Pure Appl. Geophys.*, 168(11):1989–2010, 2011.

Gernon, T. M., Hincks, T. K., Tyrrell, T., Rohling, E. J., and Palmer, M. R. Snowball Earth ocean chemistry driven by extensive ridge volcanism during Rodinia breakup. *Nature Geosci.*, 9(3):242–U83, 2016.

Global Volcanism Program. Report on Ahyi (United States). *Scientific Event Alert Network Bulletin*, 4(11), 1979.

Global Volcanism Program. Report on Ahyi (United States). 26(5), 2001.

Global Volcanism Program. Volcanoes of the World. Technical report, Smithsonian Institution, 2013.

Global Volcanism Program. Report on Ahyi (United States). 39(2), 2014.

Global Volcanism Program. Report on Monowai (New Zealand). 42(2), 2017a.

Global Volcanism Program. Report on Ahyi (United States). 42(4), 2017b.

Godin, O. A. Transmission of low-frequency sound through the water-to-air interface. *Acoustical Physics*, 53(3):305–312, 2007.

Graeber, F. M. and Piserchia, P. F. Zones of T-wave excitation in the NE Indian ocean mapped using variations in backazimuth over time obtained from multi-channel correlation of IMS hydrophone triplet data. *Geophys. J. Int.*, 158(1):239–256, 2004.

Graham, I. J., Reyes, A. G., Wright, I. C., Peckett, K. M., Smith, I. E. M., and Arculus, R. J. Structure and petrology of newly discovered volcanic centers in the northern Kermadec-southern Tofua arc, South Pacific Ocean. *J. Geophys. Res.*, 113(B8), 2008.

Green, D. N., Evers, L. G., Fee, D., Matoza, R. S., Snellen, M., Smets, P., and Simons, D. Hydroacoustic, infrasonic and seismic monitoring of the submarine eruptive activity and sub-aerial plume generation at South Sarigan, May 2010. *J. Volc. Geotherm. Res.*, 257:31–43, 2013.

Gualandi, A., Perfettini, H., Radiguet, M., Cotte, N., and Kostoglodov, V. GPS deformation related to the Mw 7.3, 2014, Papanoa earthquake (Mexico) reveals the aseismic behavior of the Guerrero seismic gap. *Geophys. Res. Lett.*, 44(12): 6039–6047, 2017.

Guilbert, J., Vergoz, J., Schisselé, E., Roueff, A., and Cansi, Y. Use of hydroacoustic and seismic arrays to observe rupture propagation and source extent of the Mw = 9.0 Sumatra earthquake. *Geophys. Res. Lett.*, 32(1):15310, 2005.

Haney, M. M., Chadwick, W. W., Merle, S. G., Buck, N. J., Butterfield, D. A., Coombs, M. L., Evers, L. G., Heaney, K. D., Lyons, J. J., Searcy, C. K., Walker, S. L., Young, C., and Embley, R. W. The 2014 Submarine Eruption of Ahyi Volcano, Northern Mariana Arc. In *AGU Fall Meeting Abstracts*, 2014.

Hanson, J., Le Bras, R., Dysart, P., Brumbaugh, D., Gault, A., and Guern, J. Operational processing of hydroacoustics at the Prototype International Data Center. *Pure Appl. Geophys.*, 158(3):425–456, 2001.

Hanson, J. A. and Bowman, J. R. Dispersive and reflected tsunami signals from the 2004 Indian Ocean tsunami observed on hydrophones and seismic stations. *Geophys. Res. Lett.*, 32(17):7–5, 2005a.

Hanson, J. A. and Bowman, J. R. Indian Ocean ridge seismicity observed with a permanent hydroacoustic network. *Geophys. Res. Lett.*, 32(6), 2005b.

Hanson, J. A. and Bowman, J. R. Methods for monitoring hydroacoustic events using direct and reflected T waves in the Indian Ocean. *J. Geophys. Res.*, 111(B2), 2006.

Heaney, K. D., Campbell, R. L., and Snellen, M. Long range acoustic measurements of an undersea volcano. *J. Acoust. Soc. Am.*, 134(4):3299, 2013.

Helffrich, G., Heleno, S. I. N., Faria, B., and Fonseca, J. F. B. D. Hydroacoustic detection of volcanic ocean-island earthquakes. *Geophys. J. Int.*, 167(3):1529–1536, 2006.

Hildebrand, J. A. Impacts of Anthropogenic Sound. In Reynolds III, J. E., Perrin, W. F., Reeves, R. R., Montgomery, S., and Ragen, T. J., editors, *Marine Mammal Research Conservation beyond Crisis*, pages 101–124. Baltimore, 2005.

Hildebrand, J. A. Anthropogenic and natural sources of ambient noise in the ocean. *Mar. Ecol. Prog. Series*, 395:5–20, 2009.

Hillier, J. K. and Watts, A. B. Global distribution of seamounts from ship-track bathymetry data. *Geophys. Res. Lett.*, 34(13), 2007.

Holt, M. M., Noren, D. P., Veirs, V., Emmons, C. K., and Veirs, S. Speaking up: Killer whales (Orcinus orca) increase their call amplitude in response to vessel noise. *J. Acoust. Soc. Am.*, 125(1):EL27–EL32, 2009.

Ito, A., Sugioka, H., Suetsugu, D., Shiobara, H., Kanazawa, T., and Fukao, Y. Detection of small earthquakes along the Pacific-Antarctic Ridge from T-waves recorded by abyssal ocean-bottom observatories. *Mar. Geophys. Res.*, 33(3):229–238, 2012.

Jutzeler, M., Marsh, R., Carey, R. J., White, J. D. L., Talling, P. J., and Karlstrom, L. On the fate of pumice rafts formed during the 2012 Havre submarine eruption. *Nature Commun.*, 5, 2014.

Ketner, D. and Power, J. Characterization of seismic events during the 2009 eruption of Redoubt Volcano, Alaska. *J. Volc. Geotherm. Res.*, 259:45–62, 2013.

Kibblewhite, A. C. Attenuation of Sound in Marine-Sediments - a Review with Emphasis on New Low-Frequency Data. *J. Acoust. Soc. Am.*, 86(2):716–738, 1989.

Koch, K. Eight Years of Continuous Quality Assessment of the International Data Centre (IDC) Reviewed Event Bulletin. *B. Seismol. Soc. Am.*, 103(1):296–305, 2013.

Konter, J. G., Staudigel, H., Hart, S. R., and Shearer, P. M. Seafloor seismic monitoring of an active submarine volcano: Local seismicity at Vailulu'u Seamount, Samoa. *Geochem. Geophys. Geosyst.*, 5(6):1991–15, 2004.

Kosuga, M. Localization of T-wave energy on land revealed by a dense seismic network in Japan. *Geophys. J. Int.*, 187(1):338–354, 2011.

Koyanagi, S., Aki, K., Biswas, N., and Mayeda, K. Inferred attenuation from site effect-corrected T phases recorded on the island of Hawaii. *Pure Appl. Geophys.*, 144(1):1–17, 1995.

Le Bras, R. J., Kuzma, H., Sucic, V., and Bokelmann, G. Observations and Bayesian location methodology of transient acoustic signals (likely blue whales) in the Indian Ocean, using a hydrophone triplet. *J. Acoust. Soc. Am.*, 139(5):2656–2667, 2016.

Le Pichon, A., Maurer, V., Raymond, D., and Hyvernaud, O. Infrasound from ocean waves observed in Tahiti. *Geophys. Res. Lett.*, 31(19), 2004.

Leybourne, M. I., Schwarz-Schampera, U., de Ronde, C. E. J., Baker, E. T., Faure, K., Walker, S. L., Butterfield, D. A., Resing, J. A., Lupton, J. E., Hannington, M. D., Gibson, H. L., Massoth, G. J., Embley, R. W., Chadwick, W. W., Clark, M. R., Timm, C., Graham, I. J., and Wright, I. C. Submarine Magmatic-Hydrothermal Systems at the Monowai Volcanic Center, Kermadec Arc. *Economic Geology*, 107 (8):1669–1694, 2012.

Li, B. *Acoustic observation of ice rifting and breaking events on the Antarctic ice shelf using remote hydroacoustic listening stations.* PhD thesis, 2010.

Lindsay, J. M., Shepherd, J. B., and Wilson, D. Volcanic and scientific activity at Kick 'em Jenny submarine volcano 2001-2002: Implications for volcanic hazard in the Southern Grenadines, Lesser Antilles. *Natural Hazards*, 34(1):1–24, 2005.

Linehan, D. Earthquakes in the West Indian region. *Trans. Am. geophys. Union*, 22: 229–232, 1940.

Mackenzie, K. V. 9-Term Equation for Sound Speed in the Oceans. *J. Acoust. Soc. Am.*, 70(3):807–812, 1981.

Massey, F. J. The Kolmogorov-Smirnov Test for Goodness of Fit. *J. Am. Stat. Assoc.*, 46(253):68–78, 1951.

Massoth, G., Baker, E., Worthington, T., Lupton, J., de Ronde, C., Arculus, R., Walker, S., Nakamura, K., Ishibashi, J., Stoffers, P., Resing, J., Greene, R., and Lebon, G. Multiple hydrothermal sources along the south Tonga arc and Valu Fa Ridge. *Geochem. Geophys. Geosyst.*, 8(11), 2007.

Mastin, L. G. and Witter, J. B. The hazards of eruptions through lakes and seawater. *J. Volc. Geotherm. Res.*, 97(1-4):195–214, 2000.

Mather, T. A., Witt, M. L. I., Pyle, D. M., Quayle, B. M., Aiuppa, A., Bagnato, E., Martin, R. S., Sims, K. W. W., Edmonds, M., Sutton, A. J., and Ilyinskaya, E. Halogens and trace metal emissions from the ongoing 2008 summit eruption of Kilauea volcano, Hawaii. *Geochimica Et Cosmochimica Acta*, 83:292–323, 2012.

Matoza, R. S. and Chouet, B. A. Subevents of long-period seismicity: Implications for hydrothermal dynamics during the 2004–2008 eruption of Mount St. Helens. *J. Geophys. Res.*, 115(B12):489–26, 2010.

Matoza, R. S., Le Pichon, A., Vergoz, J., Herry, P., Lalande, J. M., Lee, H., Che, I., and Rybin, A. Infrasonic observations of the June 2009 Sarychev Peak eruption, Kuril Islands: Implications for infrasonic monitoring of remote explosive volcanism. *J. Volc. Geotherm. Res.*, 200(1-2):35–48, 2011a.

Matoza, R. S., Vergoz, J., Le Pichon, A., Ceranna, L., Green, D. N., Evers, L. G., Ripepe, M., Campus, P., Liszka, L., Kværna, T., Kjartansson, E., and Höskuldsson, Á. Long-range acoustic observations of the Eyjafjallajökull eruption, Iceland, April-May 2010. *Geophys. Res. Lett.*, 38(6), 2011b.

Matoza, R. S., Green, D. N., Le Pichon, A., Shearer, P. M., Fee, D., Mialle, P., and Ceranna, L. Automated detection and cataloging of global explosive volcanism using the International Monitoring System infrasound network. *J. Geophys. Res*, 122(4):2946–2971, 2017.

Matsumoto, H., Haxel, J. H., Dziak, R. P., Bohnenstiehl, D. R., and Embley, R. W. Mapping the sound field of an erupting submarine volcano using an acoustic glider. *J. Acoust. Soc. Am.*, 129(3):EL94, 2011.

Matsumoto, H., Haralabus, G., Zampolli, M., and Oezel, N. M. T-phase and tsunami pressure waveforms recorded by near-source IMS water-column hydrophone triplets during the 2015 Chile earthquake. *Geophys. Res. Lett.*, 43(24):12511–12519, 2016.

McKenna, M. F., Katz, S. L., Wiggins, S. M., Ross, D., and Hildebrand, J. A. A quieting ocean: Unintended consequence of a fluctuating economy. *J. Acoust. Soc. Am.*, 132(3):EL169–EL175, 2012.

McNutt, S. R. and Beavan, R. J. Volcanic earthquakes at Pavlof Volcano correlated with the solid earth tide. *Nature*, 294(5842):615–618, 1981.

McNutt, S. R. and Nishimura, T. Volcanic tremor during eruptions: Temporal characteristics, scaling and constraints on conduit size and processes. *J. Volc. Geotherm. Res.*, 178(1):10–18, 2008.

Mendoza, C. and Martinez Lopez, M. R. The Mw 7.3 Papanoa, Mexico earthquake of April 18, 2014: Implications for recurrent M $>$ 7 thrust earthquakes in western Guerrero. *Geofis. Int.*, 56(1):13–26, 2017.

Metz, D., Watts, A. B., Grevemeyer, I., Rodgers, M., and Paulatto, M. Ultra-long-range hydroacoustic observations of submarine volcanic activity at Monowai, Kermadec Arc. *Geophys. Res. Lett.*, 43(4):1529–1536, 2016.

Munk, W. Global Ocean Warming: Detection by Long-Path Acoustic Travel Times. *Oceanography*, 2(2):40–41, 1989.

Munk, W. H. and Forbes, A. M. G. Global Ocean Warming: An Acoustic Measure? *J. Phys. Oceanography*, 19(11):1765–1780, 1989.

Munk, W. H. and Zachariasen, F. Refraction of Sound by Islands and Seamounts. 1991.

Munk, W. H., O'Reilly, W. C., and Reid, J. L. Australia-Bermuda Sound-Transmission Experiment (1960) Revisited. *J. Phys. Oceanography*, 18(12):1876–1898, 1988.

Munk, W. H., Spindel, R. C., and Baggeroer, A. The Heard Island feasibility test. *J. Acoust. Soc. Am.*, 96(4):2330, 1994.

Nakano, M., Nakamura, T., Kamiya, S., Ohori, M., and Kaneda, Y. Intensive seismic activity around the Nankai trough revealed by DONET ocean-floor seismic observations. *Earth, Planets and Space*, 65(1):5–15, 2013.

Neuberg, J. W., Tuffen, H., Collier, L., Green, D., Powell, T., and Dingwell, D. The trigger mechanism of low-frequency earthquakes on Montserrat. *J. Volc. Geotherm. Res.*, 153(1-2):37–50, 2006.

Nichols, S. M. and Bradley, D. L. In Situ Shape Estimation of Triangular Moored Hydrophone Arrays Using Ambient Signals. *IEEE J. Oceanic Eng.*, pages 1–13, 2016.

Nieukirk, S. L., Stafford, K. M., Mellinger, D. K., Dziak, R. P., and Fox, C. G. Low-frequency whale and seismic airgun sounds recorded in the mid-Atlantic Ocean. *J. Acoust. Soc. Am.*, 115(4):1832–1843, 2004.

Nishida, K. and Ichihara, M. Real-time infrasonic monitoring of the eruption at a remote island volcano using seismoacoustic cross correlation. *Geophys. J. Int.*, 204 (2):748–752, 2016.

Norris, R. A. and Johnson, R. H. Submarine volcanic eruptions recently located in the Pacific by Sofar Hydrophones. *J. Geophys. Res.*, 74(2):2156–2202, 1969.

Northrop, J. Detection of low-frequency underwater sounds from a submarine volcano in the Western Pacific. *J. Acoust. Soc. Am.*, 56(3):837–841, 1974.

Northrop, J. and Colborn, J. G. Sofar channel axial sound speed and depth in the Atlantic Ocean. *J. Geophys. Res.*, 79(3):5633–5641, 1974.

Okal, E. A. T-phase Stations for the International Monitoring System of the Comprehensive Nuclear-Test-Ban Treaty: A Global Perspective. *Seismol. Res. Lett.*, 72 (2):186–196, 2001.

O'Malley, R. T., Behrenfeld, M. J., Westberry, T. K., Milligan, A. J., Reese, D. C., and Halsey, K. H. Improbability mapping: A metric for satellite-detection of submarine volcanic eruptions. *Remote Sens. Environ.*, 140:596–603, 2014.

Papanicolopulu, I. The European Union and the Regulation of Underwater Noise Pollution. In *The World Ocean in Globalisation*, pages 457–471. Brill, 2011.

Parks, M. M., Biggs, J., Mather, T. A., Pyle, D. M., Amelung, F., Monsalve, M. L., and Narvaez Medina, L. Co-eruptive subsidence at Galeras identified during an InSAR survey of Colombian volcanoes (2006-2009). *J. Volc. Geotherm. Res.*, 202 (3-4):228–240, 2011.

Paulatto, M., Watts, A. B., and Peirce, C. Potential field and high-resolution bathymetry investigation of the Monowai volcanic centre, Kermadec Arc: implications for caldera formation and volcanic evolution. *Geophys. J. Int.*, 197(3): 1484–1499, 2014.

Power, J. A., Stihler, S. D., Chouet, B. A., Haney, M. M., and Ketner, D. M. Seismic observations of Redoubt Volcano, Alaska — 1989–2010 and a conceptual model of the Redoubt magmatic system. *J. Volc. Geotherm. Res.*, 259:31–44, 2013.

Pulli, J. J. and Upton, Z. M. Hydroacoustic observations of Indian earthquake provide new data on T-waves. *Eos*, 83(13):145–151, 2002.

Radiguet, M., Perfettini, H., Cotte, N., Gualandi, A., Valette, B., Kostoglodov, V., Lhomme, T., Walpersdorf, A., Cabral Cano, E., and Campillo, M. Triggering of the 2014M(w)7.3 Papanoa earthquake by a slow slip event in Guerrero, Mexico. *Nature Geosci.*, 9(11):829–834, 2016.

Resing, J. A., Baker, E. T., Lupton, J. E., Walker, S. L., Butterfield, D. A., Massoth, G. J., and Nakamura, K. Chemistry of hydrothermal plumes above submarine volcanoes of the Mariana Arc. *Geochem. Geophys. Geosyst.*, 10(2), 2009.

Rodgers, M., Roman, D. C., Geirsson, H., LaFemina, P., Munoz, A., Guzman, C., and Tenorio, V. Seismicity accompanying the 1999 eruptive episode at Telica Volcano, Nicaragua. *J. Volc. Geotherm. Res.*, 265:39–51, 2013.

Rolling Deck to Repository Program. Cruise MGL1701 on R/V Marcus G. Langseth. Technical report, 2017.

Ryan, J. G. Criterion for the minimum source distance at which plane-wave beamforming can be applied. *J. Acoust. Soc. Am.*, 104(1):595–598, 1998.

Schnur, S. R., Chadwick, W. W., Embley, R. W., Ferrini, V. L., de Ronde, C. E. J., Cashman, K. V., Deardorff, N. D., Merle, S. G., Dziak, R. P., Haxel, J. H., and Matsumoto, H. A decade of volcanic construction and destruction at the summit of NW Rota-1 seamount: 2004-2014. *J. Geophys. Res*, 122(3):1558–1584, 2017.

Schoeppner, M., Plastino, W., Povinec, P. P., Wotawa, G., Bella, F., Budano, A., De Vincenzi, M., and Ruggieri, F. Estimation of the time-dependent radioactive source-term from the Fukushima nuclear power plant accident using atmospheric transport modelling. *J. Environ. Rad.*, 114:10–14, 2012.

Schwarz-Schampera, U., Botz, R., and Hannington, M. RV SONNE - Cruise Report SO192-2. Technical report, GEOMAR Helmholtz Centre for Ocean Research Kiel, Kiel, 2007.

Selby, N. D., Bowers, D., Marshall, P. D., and Douglas, A. Empirical path and station corrections for surface-wave magnitude, M-s, using a global network. *Geophys. J. Int.*, 155(2):379–390, 2003.

Sherburn, S. and White, R. S. Tectonics of the Taranaki region, New Zealand: earthquake focal mechanisms and stress axes. *New Zeal. J. Geol. Geop.*, 49(2):269–279, 2006.

Sirovic, A., Wiggins, S. M., and Oleson, E. M. Ocean noise in the tropical and subtropical Pacific Ocean. *J. Acoust. Soc. Am.*, 134(4):2681–2689, 2013.

Smith, D. K., Tolstoy, M., Fox, C. G., Bohnenstiehl, D. R., Matsumoto, H., and Fowler, M. J. Hydroacoustic monitoring of seismicity at the slow-spreading Mid-Atlantic Ridge. *Geophys. Res. Lett.*, 29(1):1518, 2002.

Smith, D. K., Escartin, J., Cannat, M., Tolstoy, M., Fox, C. G., Bohnenstiehl, D., and Bazin, S. Spatial and temporal distribution of seismicity along the northern Mid-Atlantic Ridge (15°-35°N). *J. Geophys. Res*, 108(B):2167, 2003.

Smith, M. S. and Shepherd, J. B. Tsunami waves generated by volcanic landslides: an assessment of the hazard associated with Kick 'em Jenny. *Geological Society*, 110(1):115–123, 1996.

Snelling, B. T-waves and Tectonics: A survey of acoustic signals generated by tectonic processes on spreading ridges in the Indian Ocean. pages 1–61, 2015.

Sottili, G. and Palladino, D. M. Tidal modulation of eruptive activity at open-vent volcanoes: evidence from Stromboli, Italy. *Terra Nova*, 24(3):233–237, 2012.

Sousa, A. G. and Harris, D. Description and seasonal detection of two potential whale calls recorded in the Indian Ocean. *J. Acoust. Soc. Am.*, 138(3):1379–1388, 2015.

Stevens, J. L., Baker, G. E., Cook, R. W., D'Spain, G. L., Berger, L. P., and Day, S. M. Empirical and Numerical Modeling of T-phase Propagation from Ocean to Land. *Pure Appl. Geophys.*, 158(3):531–565, 2001.

Stoffers, P., Botz, R., Cheminee, J. L., Devey, C. W., Froger, V., Glasby, G. P., Hartmann, M., Hekinian, R., Kogler, F., Laschek, D., Larque, P., Michaelis, W., Muhe, R. K., Puteanus, D., and Richnow, H. H. Geology of Macdonald Seamount Region, Austral-Islands - Recent Hotspot Volcanism in the South-Pacific. *Mar. Geophys. Res.*, 11(2):101–112, 1989.

Stoffers, P., Worthington, T. J., Schwarz-Schampera, U., Hannington, M. D., Massoth, G. J., Hekinian, R., Schmidt, M., Lundsten, L. J., Evans, L. J., Vaiomo'unga, R., and Kerby, T. Submarine volcanoes and high-temperature hydrothermal venting on the Tonga arc, southwest Pacific. *Geology*, 34(6):453–456, 2006.

Talandier, J. and Kuster, G. T. Seismicity and Submarine Volcanic Activity in French Polynesia. *J. Geophys. Res.*, 81(5):936–948, 1976.

Talandier, J. and Okal, E. A. New Surveys of Macdonald Seamount, Southcentral Pacific, Following Volcanoseismic Activity, 1977-1983. *Geophys. Res. Lett.*, 11(9): 813–816, 1984.

Talandier, J. and Okal, E. A. Seismic Detection of Underwater Volcanism - the Example of French Polynesia. *Pure Appl. Geophys.*, 125(6):919–950, 1987.

Talandier, J., Hyvernaud, O., Reymond, D., and Okal, E. A. Hydroacoustic signals generated by parked and drifting icebergs in the Southern Indian and Pacific Oceans. *Geophys. J. Int.*, 165(3):817–834, 2006.

Tolstoy, I., Ewing, M., and Press, F. T Phase of Shallow-Focus Submarine Earthquakes. *Geol. Soc. Am. Bull.*, 60(12):1957–1957, 1949.

Tolstoy, M. Mid-ocean ridge eruptions as a climate valve. *Geophys. Res. Lett.*, 42(5): 1346–1351, 2015.

Tolstoy, M. and Bohnenstiehl, D. R. Hydroacoustic constraints on the rupture duration, length, and speed of the Great Sumatra-Andaman Earthquake. *Seismol. Res. Lett.*, 76(4):419–425, 2005.

Tolstoy, M., Constable, S., Orcutt, J., Staudigel, H., Wyatt, F. K., and Anderson, G. Short and long baseline tiltmeter measurements on axial seamount, Juan de Fuca Ridge. *Phys. Earth Planet. Inter.*, 108(2):129–141, 1998.

Tolstoy, M., Vernon, F. L., Orcutt, J. A., and Wyatt, F. K. Breathing of the seafloor: Tidal correlations of seismicity at Axial volcano. *Geology*, 30(6):503–506, 2002.

Tolstoy, M., Cowen, J. P., Baker, E. T., Fornari, D. J., Rubin, K. H., Shank, T. M., Waldhauser, F., Bohnenstiehl, D. R., Forsyth, D. W., Holmes, R. C., Love, B., Perfit, M. R., Weekly, R. T., Soule, S. A., and Glazer, B. A sea-floor spreading event captured by seismometers. *Science*, 314(5807):1920–1922, 2006.

Tuma, M., Rorbech, V., Prior, M. K., and Igel, C. Integrated Optimization of Long-Range Underwater Signal Detection, Feature Extraction, and Classification for Nuclear Treaty Monitoring. *Ieee Trans. Geosci. Remote Sens. Lett.*, 54(6):3649–3659, 2016.

Walter, T. R., Wang, R., Zimmer, M., Grosser, H., Luehr, B., and Ratdomopurbo, A. Volcanic activity influenced by tectonic earthquakes: Static and dynamic stress triggering at Mt. Merapi. *Geophys. Res. Lett.*, 34(5), 2007.

Ward, R., Gavrilov, A. N., and McCauley, R. D. Spot call: A common sound from an unidentified great whale in Australian temperate waters. *J. Acoust. Soc. Am.*, 142(2):EL231–EL236, 2017.

Watts, A. B., Sandwell, D. T., Smith, W. H. F., and Wessel, P. Global gravity, bathymetry, and the distribution of submarine volcanism through space and time. *J. Geophys. Res*, 111(B8), 2006.

Watts, A. B., Peirce, C., Grevemeyer, I., Paulatto, M., Stratford, W., Bassett, D., Hunter, J. A., Kalnins, L. M., and de Ronde, C. E. J. Rapid rates of growth and collapse of Monowai submarine volcano in the Kermadec Arc. *Nature Geosci.*, 5 (7):510–515, 2012.

Werner, R., Nuernberg, D., and Hauff, F. RV SONNE - Cruise Report SO225. Technical report, GEOMAR Helmholtz Centre for Ocean Research Kiel, Kiel, 2013.

Wiemer, S. and Wyss, M. Minimum magnitude of completeness in earthquake catalogs: Examples from Alaska, the western United States, and Japan. *B. Seismol. Soc. Am.*, 90(4):859–869, 2000.

Williams, C. M., Stephen, R. A., and Smith, D. K. Hydroacoustic events located at the intersection of the Atlantis (30°N) and Kane (23°40'N) Transform Faults with the Mid-Atlantic Ridge. *Geochemistry*, 7(6), 2006.

Williams, R., Wright, A. J., Ashe, E., Blight, L. K., Bruintjes, R., Canessa, R., Clark, C. W., Cullis-Suzuki, S., Dakin, D. T., Erbe, C., Hammond, P. S., Merchant, N. D., O'Hara, P. D., Purser, J., Radford, A. N., Simpson, S. D., Thomas, L., and Wale, M. A. Impacts of anthropogenic noise on marine life: Publication patterns, new discoveries, and future directions in research and management. *Ocean and Coastal Management*, 115(C):17–24, 2015.

Woessner, J. and Wiemer, S. Assessing the Quality of Earthquake Catalogues: Estimating the Magnitude of Completeness and Its Uncertainty. *B. Seismol. Soc. Am.*, 95(2):684–698, 2005.

Woolfe, K. F. and Sabra, K. G. Variability of the coherent arrivals extracted from low-frequency deep-ocean ambient noise correlations. *J. Acoust. Soc. Am.*, 138(2): 521–532, 2015.

Wormald, S. C., Wright, I. C., Bull, J. M., Lamarche, G., and Sanderson, D. J. Morphometric analysis of the submarine arc volcano Monowai (Tofua-Kermadec Arc) to decipher tectono-magmatic interactions. *J. Volc. Geotherm. Res.*, 239: 69–82, 2012.

Wright, I. C., Chadwick, W., de Ronde, C. E. J., Reymond, D., Hyvernaud, O., Gennerich, H. H., Stoffers, P., Mackay, K., Dunkin, M. A., and Bannister, S. C. Collapse and reconstruction of Monowai submarine volcano, Kermadec arc, 1998-2004. *J. Geophys. Res.*, 113(B8), 2008.

Wyss, M., Habermann, R. E., and Griesser, J. C. Seismic Quiescence and Asperities in the Tonga-Kermadec Arc. *J. Geophys. Res.*, 89(NB11):9293–9304, 1984.

Yang, Y. J. and Forsyth, D. W. Improving epicentral and magnitude estimation of earthquakes from T phases by considering the excitation function. *B. Seismol. Soc. Am.*, 93(5):2106–2122, 2003.

Ye, L., Lay, T., Bai, Y., Cheung, K. F., and Kanamori, H. The 2017 Mw 8.2 Chiapas, Mexico, Earthquake: Energetic Slab Detachment. *Geophys. Res. Lett.*, 44(23): 11824–11832, 2017.